Ultrafast optical studies of electronic dynamics in semiconductors

By

Brian A. Ruzicka

Submitted to the Department of Physics and Astronomy and the
Faculty of the Graduate School of the University of Kansas
in partial fulfillment of the requirements for the degree of
Doctor of Philosophy

Dr. Hui Zhao, Chairperson

Dr. Judy Wu

Committee members

Dr. Siyuan Han

Dr. Hsin-Ying Chiu

Dr. Shenqiang Ren

Date defended: 04/03/2012

The Dissertation Committee for Brian A. Ruzicka certifies
that this is the approved version of the following dissertation :

Ultrafast optical studies of electronic dynamics in semiconductors

_____

Dr. Hui Zhao, Chairperson

Date approved: 04/03/2012

Dedicated to my wonderful parents Jim and Leslie,

my sister Sarah,

and my amazing wife Gabby

List of publications

1. B.A. Ruzicka, L.K. Werake, G. Xu, J.B. Khurgin, E.Y. Sherman, J.Z. Wu, and H. Zhao, "Second-harmonic generation induced by electric currents in GaAs," *Phys. Rev. Lett.* 108, 077403 (2012).

2. B.A. Ruzicka and H. Zhao, "Optical studies of ballistic currents in semiconductors," *Journ. Opt. Soc. Am. B* 29, A43 (2012).

3. B.A. Ruzicka, N. Kumar, S. Wang, K.P. Loh, and H. Zhao, "Two-probe study of hot carriers in reduced graphene oxide," *Journ. Appl. Phys.* 109, 084322 (2011).

4. B.A. Ruzicka, L.K. Werake, H. Samassekou, and H. Zhao, "Ambipolar diffusion of photo-excited carriers in bulk GaAs," *Appl. Phys. Lett.* 97, 262119 (2010).

5. B.A. Ruzicka, S. Wang, L.K. Werake, B. Weintrub, K.P. Loh, and H. Zhao, "Hot carrier diffusion in graphene," *Phys. Rev. B* 82, 195414 (2010).

6. B.A. Ruzicka, L.K. Werake, H. Zhao, S. Wang, and K.P. Loh, "Femtosecond pump-probe studies of reduced graphene oxide thin films," *Appl. Phys. Lett.* 96, 173106 (2010).

7. B.A. Ruzicka and H. Zhao, "Power dependence of pure spin current injection by quantum interference," *Phys. Rev. B* 79, 155204 (2009).

8. B.A. Ruzicka, K. Higley, L.K. Werake, and H. Zhao, "All-optical generation and detection of subpicosecond ac spin-current pulses in GaAs," *Phys. Rev. B* 78, 045314 (2008).

9. N. Kumar, B.A. Ruzicka, N.P. Butch, P. Syers, K. Kirshenbaum, J. Paglione, and H. Zhao, "Spatially resolved femtosecond pump-probe study of topological insulator Bi_2Se_3," *Phys. Rev. B* 83, 235306 (2011).

10. L.K. Werake, B.A. Ruzicka, and H. Zhao, "Observation of intrinsic inverse spin Hall effect," *Phys. Rev. Lett.* 106, 107205 (2011).

11. E.J. Loren, B.A. Ruzicka, L.K. Werake, H. Zhao, H.M. van Driel, and A.L. Smirl, "Optical injection and detection of ballistic pure spin currents in Ge," *Appl. Phys. Lett.* 95, 092107 (2009).

Abstract

The dynamics of charge carriers in semiconductors are of fundamental importance for semiconductor applications. This includes studies of energy relaxation, carrier recombination, and carrier transport (both diffusive and ballistic). Due to their limited temporal resolution, electron measurement techniques cannot be used to study these processes on time scales in which the carrier-lattice system is not in equilibrium. However, in contemporary semiconductor devices with nanometer dimensions, this is the regime that is of interest. In this dissertation, ultrafast optical experimental techniques and results from various semiconductors are presented, which provide information about nonequilibrium electronic dynamics. First, a time resolved pump-probe technique is discussed, which can be used to measure carrier energy relaxation and carrier lifetime, and results are presented on reduced graphene oxide, Si/SiGe quantum wells, and single walled carbon nanotubes. Then, a spatially and temporally resolved pump-probe technique is discussed, which can be used to study carrier diffusion, and results are presented on GaAs, graphene, Si/SiGe quantum wells and single walled carbon nanotubes. Next, a quantum interference and control technique and a differential pump-probe technique that can be used to inject and detect ballistic currents are discussed along with results for the efficiency of such an injection technique and a demonstration of an AC spin polarized charge current in GaAs that was injected and detected using these techniques. Finally, a current induced second harmonic generation technique that can be used to directly study currents is discussed, with results presented on both steady state and transient currents in GaAs.

Acknowledgements

I am grateful to have had the opportunity to spend my time as a graduate student working with such brilliant and kind people. Without these people's help, I would not have been able to complete my Ph.D. and I would like to sincerely thank everyone for this. First, I would like to thank my advisor, Dr. Hui Zhao. Although I was one of his first graduate students, you would think he has been advising students for several years, because he is already very good at it. Besides teaching me practically every experimental skill that I now possess, he has always given me the guidance that I needed and was willing to take time to answer my questions, even managing to not make fun of me too much when the questions are bad, which I know can be difficult. Also, I am very thankful that I have had the privilege to play a role in bringing the ideas that he came up with to fruition. He has provided me with an enormous amount of opportunities and any success I had as a graduate student and will (hopefully) have in my future career I owe to him.

I would also like to thank my lab mates Lalani Werake, Eric Loren, Nardeep Kumar, and Rui Wang. I have learned a great deal from all of you and enjoyed working with you all. Also they each assisted with some of the measurements that were discussed in the dissertation. Specifically, Lalani Werake took most of the data for the second harmonic generation study of ballistic currents that were injected optically in gallium arsenide, Nardeep Kumar assisted with the two-probe study of hot carriers of graphene, and Rui Wang assisted with the carbon nanotube measurements. Also, I would like to acknowledge the undergraduate students who worked with me in various experiments. Specifically, Karl Higley who assisted in collecting the spin-polarized charge current data, Ben Weintrub who assisted with the graphene diffusion experiment, and Hassana Samassekou who assisted with the GaAs diffusion experiment.

I owe thanks to several other people here at KU outside of our group as well. First, I would like to thank my committee members. Besides providing me with the all-important signatures, I have gained a vast amount of knowledge and assistance from each of you in the lab. I would like to specifically thank Dr. Judy Wu for providing us with the CVD graphene sample and her student Guowei Xu who fabricated the electrodes on the gallium arsenide sample for the second harmonic

generation from charge current experiment. Also, I would like to acknowledge Dr. Siyuan Han who assisted in our understanding of the electronic measurements during the second harmonic generation from charge current experiment. Finally, Dr. Shenqiang Ren fabricated the carbon nanotube samples. My fellow condensed matter graduate students and the postdoctoral researchers from Dr. Wu's group also provided me with much help. I especially thank Caitlin Rochford, Guowei Xu, Alan Elliot, Rongtao Lu, and Jianwei Liu for always being willing to take time help me whenever I popped into your lab or offices unannounced.

Additionally, many people outside of KU deserve recognition for their roles in our several collaborations. John Prineas from the University of Iowa provided us with high quality gallium arsenide samples, which were used in the diffusion, quantum interference and control, and optically pumped second harmonic generation experiments. Kian Ping Loh and his student Shuai Wang from the National University of Singapore provided the reduced graphene oxide and epitaxial graphene samples. Finally, Jacob Khurgin from Johns Hopkins University and Eugene Ya. Sherman from Spain performed theoretical calculations for the current induced second harmonic experiment. I would like to thank all of our collaborators for their excellent work.

Finally, I would like to thank my friends and family for their support during my time as a graduate student. I thank my parents Jim and Leslie for encouraging me to do my best in everything that I do and showing their pride and interest in my work. Thank you both for always being there for me and helping me with the things in life that aren't related to physics. I would never have made it this far without everything that I learned from both of you. I also thank my sister Sarah for always being there to talk to me, and for always making sure I remembered to enjoy myself outside of school. And last, but definitely not least, I would like to thank my wife Gabby for staying by my side and always supporting my studies even when I was gone spending those long hours in the lab. Thank you, Gabby, for always being there for me whenever I needed you and for the happiness and joy that you bring to my life every day.

Contents

List of Figures

List of Tables

List of Symbols and Abbreviations

$1/\tau_e$ Energy relaxation rate

$1/\tau_r$ Carrier recombination rate

α Absorption coefficient

$\Delta R/R_0$ Differential reflection

ΔR Change in reflection of the probe caused by the pump

$\Delta T/T_0$ Differential transmission

ΔT Change in transmission of the probe caused by the pump

ε_0 Permittivity of free space (8.854×10^{-12} F/m)

$\hbar$ Reduced Planck's constant (6.582×10^{-16} eV·s)

P   Material polarization

ω_p Plasma frequency

c Speed of light (3×10^8 m/s)

D Diffusion coefficient

e Magnitude of electron charge (1.602×10^{-19} C)

E_g Band gap energy

f_{rep} Laser repetition rate

$g(E)$ Density of states

J_d Drift current density

J_f Diffusion current density

k_B Boltzmann constant (8.617×10^{-5} eV/K)

m_e^* Electron effective mass

m_h^* Hole effective mass

N Carrier density

n Index of refraction

R Reflectance

R_0 Reflection of the probe with no pump

S Spin density

T Transmittance

T_0 Transmission of the probe with no pump

v_d Drift velocity

Chapter 1

Introduction

1.1   Motivation for ultrafast optical studies of carrier dynamics

In a semiconductor, electrons in the conduction band and holes in the valence band are called charge carriers, since they are mobile and are responsible for charge transport. Carriers can be generated by different mechanisms. For example in doped semiconductors, carriers are provided by the dopant atoms. Intrinsic, or pure, semiconductors at a nonzero temperature have carriers due to thermal excitation. In both intrinsic and doped semiconductors, light absorption can excite carriers, which are known as photocarriers, since an electron in the valence band can absorb a photon with enough energy and reach the conduction band.

The dynamics of these carriers is important for many applications. In this context, the phrase "carrier dynamics" is generally applied to processes that involve motion in real space, some exchange of energy, or the disappearance of the carriers altogether. Since charge carriers are typically used in applications to carry information or energy, these processes directly determine the performance. For example, in a solar cell, how far the carriers can move before losing their energy or disappearing determines how much of the solar energy can be converted into electrical energy. Therefore, the dynamics of charge carriers in semiconductors are of fundamental importance and such studies serve as the foundation of the modern semiconductor industry. Given this fundamental

importance, each of these processes have been extensively investigated for several decades.

Most of these previous studies have been performed on carrier systems that are in thermal equilibrium with the lattice. For example, the motion in real space (i.e. carrier transport) has in the past generally always been studied on carrier systems in thermal equilibrium with the lattice. In this regime, the transport is described by the macroscopic quantities of mobility and diffusion coefficient, which are straightforwardly related to microscopic quantities of mean free path and mean free time. However, in a practical device carriers are usually injected with a nonthermal distribution. It takes multiple carrier-carrier scattering events for the carriers to exchange energy in order to establish a thermal distribution, and multiple carrier-phonon scattering events for the carrier system to reach a thermal equilibrium with the lattice. Under typical conditions, the mean free length of carriers is on the order of 10 to 100 nm.[9] Therefore, equilibrium carrier transport can only be established on larger length scales. Since feature sizes of electronic devices in integrated circuits have already been reduced to 60 nm and will approach 20 nm soon,[10] which are comparable to or even smaller than the mean free path, carriers can move through the device with few or even no collisions. This means that there is no room for the carriers to reach thermal equilibrium with the lattice and the nonthermal, nonequilibrium carrier transport plays a dominant role in nanoscale devices.

Studies of nonequilibrium carrier nanoscale transport require experimental techniques with a high temporal resolution since the transport occurs on ultrafast time scales of at most a few picoseconds. Electrical detection techniques (i.e. measurements involving electrodes and I-V characteristics) that are generally used in transport studies have limited temporal resolution. Optical techniques that involve ultrafast lasers on the other hand, are standard tools that can be used to study nonequilibrium carrier dynamics in semiconductors, due to their relatively high temporal resolution.[11] Several optical techniques to study carrier transport have been developed, including transient grating[12–17] and spatially resolved photoluminescence.[18–23] However, in contrast to these techniques, ultrafast pump-probe techniques (those discussed in this dissertation) possess several qualities that make them ideal for studies of carrier dynamics.

In order to realize these, the most basic type of ultrafast optical technique must first be described: time resolved pump-probe. Time resolved pump-probe techniques involve two short (on the order of 100 fs pulse duration) laser pulses of the same or different wavelength. One laser pulse is sent to the sample and is used to "pump" it, i.e. excite carriers by the absorption of photons. After the carriers are excited, they will lose their energy and most likely undergo some transport process – either diffusive or ballistic, i.e. involving or not involving collisions. If the second laser pulse is sent to the sample and the pump has already excited carriers, the absorption of this laser pulse can be different since the pump-excited carriers can modify the optical properties of the sample. By comparing the transmission or reflection of this laser pulse with the transmission or reflection of this laser pulse without the pump pulse present, this laser essentially serves as a "probe" of the density of carriers at the probing energy. This laser pulse can probe the carriers at different energies by changing the probe wavelength, at different times by having the probe arrive at the sample at a different time, and at different positions by sending the probe to different spots on the sample. By changing these three parameters together in different combinations, the temporal behavior of the carriers in energy and real space can be directly monitored.

With this simple description it is easy to immediately see several good qualities of such an experiment and advantages over electrical measurements of similar quantities. First, the temporal resolution is determined by the duration of the laser pulses. For typical pulsed lasers that are readily commercially available today, this can be smaller than 100 fs. Therefore, processes that occur on very short time scales can be observed using ultrafast laser techniques and the transient behavior can be observed in addition to the steady state behavior. Electrical techniques on the other hand do not have access to the transient behavior of the carriers – electrical measurements involve measuring the steady-state quantities of resistivity or conductivity.

Second, the spatial resolution is generally determined by the size of the laser spot, which can be as small as 1 μm if the beam is focused with a microscope objective lens. Furthermore, in studies of ballistic transport, the Gaussian shape of the laser spot allows for the use of a special technique to measure the carrier transport distance, with a spatial resolution as small as a few nanometers.

Therefore, very small transport distances can be observed. Apart from the spatial resolution, this demonstrates another good quality of pump-probe experiments: The measurements are local and occur only over the area of interest. In electrical measurements, however, the behavior is that of the entire material in contact with the electrodes.

Finally, since the laser pulses do not modify the material properties themselves in any way apart from the generation of carriers, the pump-probe experiment is nondestructive and noninvasive. Therefore, it can be used to study the true intrinsic properties of materials. Electrical techniques on the other hand, require the fabrication of electrodes for current measurement and therefore may lead to an alteration of the intrinsic properties of the material.

In summary, for many applications it is not sufficient to use electrical techniques to study the necessary carrier dynamics. For example, electrical techniques only have access to equilibrium carrier transport, while transport in real devices that are being developed today is nonequilibrium. Ultrafast optical techniques on the other hand, offer access to the nonequilibrium regime of carrier dynamics and therefore are essential tools for such studies. Ultrafast pump probe techniques in particular have several qualities that make them ideal for these types of studies.

1.2   Introduction to materials studied

These ultrafast optical techniques for the study of carrier dynamics have the additional advantage that they can be applied to a vast range of materials. Throughout this dissertation, the results of measurements of various aspects the dynamics of carriers in some different materials will be presented. This includes a study of carrier energy relaxation in graphene, single walled carbon nanotubes, and Si/SiGe quantum wells; a study of diffusive transport in graphene, bulk GaAs, single walled carbon nanotubes, and Si/SiGe quantum wells; a study of ballistic spin polarized charge currents in bulk GaAs; and a study of an optical effect of charge currents in bulk GaAs. Therefore, a brief introduction to some basic properties, applications, and general motivation for studying each material will be presented here, with more detailed information presented before

each experiment and even more in the appropriate appendix.

The first material for which results will be discussed in detail is graphene. Graphene consists of a two dimensional honeycomb lattice of carbon atoms. Since it was demonstrated in 2004 to have a very high carrier mobility of about $10,000$ cm^2/Vs,[24] experimental investigations into the properties of graphene quickly escalated. Since then, even higher carrier mobilities have been reported, with values reaching over $200,000$ cm^2/Vs.[25] The high carrier mobility has made it a material of great interest for use in high speed transistors, but it also gained popularity due to its large breaking strength[26] and excellent thermal conductivity.[27] There are several different types of graphene based on the method of production. The first that was made popular is known as intrinsic graphene and is produced by the mechanical exfoliation of bulk graphite by the "scotch tape" method.[24] Another type is known as epitaxial graphene, and is produced by thermal desorption of silicon in a SiC crystal.[28] Graphene can also be produced by chemical vapor deposition onto nickel or copper substrates.[29] Finally, graphene can be produced by the reduction of graphite oxide, producing a type of graphene known as reduced graphene oxide, which despite the oxide in its name is actually graphene.[30]

Graphene is a material in which ultrafast optical studies can be very useful. The initial ultrafast pump-probe studies on graphene demonstrated that the carrier dynamics are very short-lived, lasting for only a few hundred femtoseconds.[31] Additionally, due to the unique band structure of graphene, electrons move through it very fast, at $1/300^{th}$ of the speed of light.[32] The unique ability of ultrafast laser techniques to measure the ultrafast intrinsic properties of materials in a non-contact, noninvasive way makes these techniques ideal tools for the study of carrier dynamics in graphene. For a more detailed review of graphene, see Appendix B.

Strained Si/Si$_{1-x}$Ge$_x$ structures have attracted attention for several years due to their potential use in electronic and photonic applications. By controlling the relative concentrations, i.e. x, the strain can be actively controlled, which changes the band gap and therefore the optical properties.[33] Also, due to the presence of the Si, devices made with this material can be easily integrated. Therefore, this material has the potential to be used as an electro-optic modulator, or receiver for

optical communications. Hence studies of carrier lifetime and carrier transport in this material, which can be readily obtained by ultrafast optical techniques, can be very important. In order to develop applications around this material, it is essential that these properties be studied, since they can determine the speed and efficiency of such a device.

Single walled carbon nanotubes are essentially a rolled up form of graphene. The electrons are then essentially confined to move in one dimension. The result of this is a set of discrete transition energy levels.[34] Due to the structure and reasonably high carrier mobility in carbon nanotubes, they have been cited for potential use in many possible applications such as solar cells,[35] supercapacitors, and composite materials.[36] Therefore, in order to develop such applications, which rely again on the carrier lifetime and carrier transport properties, these must be studied, and an excellent way to do this is with ultrafast laser techniques. See Appendix C for more information on single walled carbon nanotubes.

The final material that will be mentioned is gallium arsenide. Gallium arsenide is a direct band gap semiconductor with band gap energy around 1.42 eV. Gallium arsenide is studied for many different reasons. In terms of applications, it is often used in high speed optoelectronic devices. However, it is studied here mainly because it serves as an ideal platform for the study of several different fundamental physical effects and demonstration of measurement techniques. As will be discussed in the following chapters, gallium arsenide has an ideal band gap for access by typical ultrafast laser configurations. This means it is easy to measure behavior on the band edge, which makes the measurements much more convenient. This in combination with its relatively large absorption coefficient and the ability to produce high quality and purity samples makes it an ideal material for these investigations.

1.3   Organization of the dissertation

All of the ultrafast optical techniques that will be discussed in this dissertation of course involve the interaction of light with semiconductors. Therefore, in Chapter 2 this interaction will be described

in detail. This includes the definition of some basic quantities that are discussed frequently in the experiments and a discussion of the physical model that is used to describe the interaction of light with semiconductors.

In Chapter 3, ultrafast optical studies of energy relaxation and carrier lifetime will be discussed. These experiments demonstrate the simplest implementation and use of ultrafast pump-probe experiments. This chapter first includes a discussion of what physically happens to the carriers in the semiconductor after excitation. Then, some fundamental experimental techniques and concepts concerning time resolved pump-probe measurements will be introduced. This will then be followed by experimental results for this type of measurement, with results from reduced graphene oxide being discussed in detail followed by a shorter discussion of results from Si/SiGe quantum wells and single walled carbon nanotubes.

Chapter 4 builds further upon the content presented in Chapter 3, with a discussion of ultrafast optical studies of carrier diffusion in semiconductors. This chapter begins with a theoretical discussion of diffusive transport and is similarly followed by a presentation of the experimental techniques used to measure the carrier diffusion coefficient and some experimental results. Results from measurements of the diffusion of carriers in bulk GaAs will be presented in detail, and the results of similar measurements that were performed on epitaxial graphene on SiC, reduced graphene oxide, graphene produced by chemical vapor deposition, Si/SiGe quantum wells, and single walled carbon nanotubes will be summarized.

After the discussion of ultrafast optical studies of diffusive transport in semiconductors, Chapter 5 will contain a discussion about ultrafast optical studies of ballistic transport. This chapter will include a theoretical discussion of the quantum interference and control technique that is used to inject ballistic currents, as well as a discussion of the differential pump-probe experimental technique that is used to indirectly detect the ballistic currents. Results on subpicosecond AC spin-polarized charge currents will be presented, as well as measurements that demonstrate the efficiency of a current injected by this quantum interference method.

Chapter 6 will be focused on an optical effect of charge currents, which can be used to directly

detect a charge current. This again includes a theoretical discussion of the effect as well as the experimental techniques that are required to observe it. Experimental results from an n-doped bulk GaAs electrode device will be presented to demonstrate this effect and then this effect will be used to directly study a ballistic charge current produced by the quantum interference and control technique.

Finally, Chapter 7 will contain a summary of the dissertation as well as information about the types of experiments that can be performed in the future using the techniques discussed in the dissertation. Also, so as to not interrupt the flow of the dissertation, additional and more detailed information about some topics is presented in various appendices. Appendix A describes the lock-in detection technique, Appendix B presents a review of the properties and previous ultrafast studies of graphene, Appendix C presents a review the properties and previous ultrafast studies of single walled carbon nanotubes, and Appendix D describes the calculations used in the determination of the laser fluence and carrier density as excited by the ultrafast laser pulses.

Chapter 2

Interaction of light with semiconductors

2.1 Introduction

Many properties of semiconductors are determined by transient electronic dynamics that occur on very short time scales. Ultrafast lasers have widely been used as a tool for accessing this information, which plays an important role in high-speed and nanoscale electronic devices. Throughout this dissertation, ultrafast laser techniques and the significance of the properties of carrier dynamics that they can be used to study will be discussed in detail. However, all ultrafast optical studies of carrier dynamics in semiconductors share the characteristic that they involve the interaction of the semiconductor with light. Therefore a general description of this interaction is required. This chapter will begin by defining some basic quantities that are used throughout the dissertation, and then go on to discuss the physical model used to describe the interaction of light with materials. From this, the interaction of light with semiconductors will be reviewed, specifically some of the different absorption processes that can occur.

2.2 Optical coefficients

Before discussing the theoretical aspects of the interactions of light with semiconductors, it is best to start with a few intuitive definitions. Consider an electric field with angular frequency ω in the

optical range, wave vector $\mathbf{k}$ and phase ϕ:

$$\mathbf{E} = \mathbf{E}_0 e^{i(\mathbf{k} \cdot \mathbf{r} - \omega t + \phi)} \tag{2.1}$$

The optical intensity, I_i, of this field will be

$$I_i = (c\varepsilon_0/2)E_0^2, \tag{2.2}$$

which has units of W/m^2. Here, c is the speed of light and ε_0 is the permittivity of free space. If such a beam is incident on a material, there are three possible things that can happen: the beam can be reflected, transmitted, or absorbed. If the reflected intensity is I_r and the transmitted intensity is I_t, then the reflectance and transmittance are defined as

$$R = \frac{I_r}{I_i} \tag{2.3}$$

and

$$T = \frac{I_t}{I_i}, \tag{2.4}$$

respectively. By conservation of energy, if there is no absorption or scattering, then $R + T = 1$.

The absorption of light by a material is described by the absorption coefficient, α. If $R = 0$, then by Beer's law the intensity of light at a depth z into the material will be

$$I(z) = I_0 e^{-\alpha z}. \tag{2.5}$$

Therefore, for a material with zero reflectivity, absorption coefficient α, and thickness L, the transmittance will be

$$T = \frac{I(L)}{I_0} = e^{-\alpha L}. \tag{2.6}$$

Equation (2.6) demonstrates that there is a direct relationship between the transmittance and the absorption coefficient of a material, which is also true for the reflectance.

2.3 Physical model

As discussed in the previous section, the transmittance and reflectance can both be expressed in terms of the absorption coefficient, α. By energy conservation, essentially what is not absorbed by the material is re-emitted, resulting in a transmitted or reflected beam of the same wavelength. Therefore, it is necessary only to discuss the physical model behind the absorption of light, since this is the most fundamental mechanism involved in ultrafast optical studies of carrier dynamics. This section will describe one-photon absorption processes, which make up the majority of the ultrafast pump-probe experiment absorption processes, as well as two-photon absorption, which is essential for the quantum interference and control experiments that are discussed in Chapter 5. All of these processes will be discussed in terms of direct semiconductors, since most of the experiments discussed in this dissertation were performed on direct semiconductors.

2.3.1 Interband absorption

2.3.1.1 One-photon absorption

If a photon of angular frequency ω is absorbed by a semiconductor, and the energy of the photon is larger than the band gap energy $(\hbar\omega > E_g)$, an electron will be excited from the valence band to the conduction band, leading to the formation of an electron-hole pair, as illustrated in Fig. 2.1(a). Since the photon has zero momentum, the electron and hole will have opposite momenta.

In order to determine the probability that a photon is absorbed by the semiconductor, and therefore the absorption coefficient, we must know the quantum mechanical transition rate, $W_{i \to f}$,
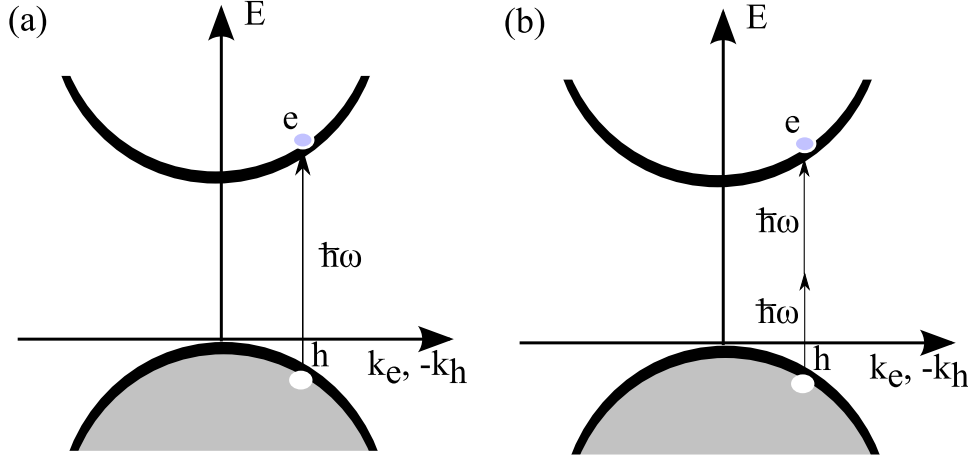
Figure 2.1: Interband one-photon absorption (a) and two-photon absorption (b) in a semiconductor.

which is defined as the rate at which an electron is excited from the initial state ϕ_i to the final state ϕ_f. Using time-dependent perturbation theory, it is easy to show that this transition rate is given by Fermi's golden rule:

$$W_{i \to f} = \frac{2\pi}{\hbar}|M|^2 g(\hbar\omega),$$ (2.7)

where M is the matrix element for the transition between states and $g(\hbar\omega)$ is the joint density of states.[37] The matrix element is

$$M = \langle \phi_f | H' | \phi_i \rangle,$$ (2.8)

where H' is the perturbation Hamiltonian. In the semi-classical approach, which is commonly used for such calculations, this perturbation is the electric-dipole interaction between the light and the electron:

$$H' = -\mathbf{p}_e \cdot \mathbf{E},$$ (2.9)

where $\mathbf{p}_e = -e\mathbf{r}$ is the electron dipole moment and $\mathbf{E}$ is the electric field. The resulting dipole matrix element, $\mathbf{P}_{\mathbf{k}'}$, depends on the semiconductor (i.e. the crystal structure and thus the band structure or electron effective mass) and the electron wave vector, $\mathbf{k}'$. The joint density of states

12

also depends on the material, and is simply the density of states, $g(E)$, evaluated at the photon energy. The transition rate for interband absorption is symmetric with respect to k', i.e. it is symmetric along any particular direction, but not necessarily symmetric with respect to $\mathbf{k}'$. This means that the light will excite carriers equally with velocities along opposite directions, but not necessarily the same in all directions.

2.3.1.2 Two-photon absorption

As illustrated in Fig. 2.1(b), if a photon of frequency ω is incident on a semiconductor with band gap energy E_g, and $\omega < E_g < 2\omega$, the single photon will not have enough energy to excite an electron from the valence band to the conduction band. If a second photon of frequency ω arrives simultaneously, however, the two photons together will have enough energy to excite an electron. The result is then the same as an electron being excited by a photon of frequency 2ω. This process is known as two-photon absorption. This can be described in a similar way to to one-photon direct interband absorption. In this case however, an intermediate transition state, ϕ_j, and the transition matrix element is calculated by summing the transition matrix element for transitions from initial to intermediate to final state over all possible intermediate states:

$$M = \sum_j \langle \phi_f | H' | \phi_j \rangle \langle \phi_j | H' | \phi_i \rangle. \tag{2.10}$$

Transitions of this type will be discussed in more detail in Chapter 5.

2.3.2 Free carrier absorption

Also of importance to ultrafast laser studies are absorption mechanisms involving free carriers. In this case, the energy of the photon is such that $\hbar\omega < E_g$, so interband absorption cannot occur. Instead, if there are free carriers present, the photon may be absorbed, being excited up to a higher energy level. This process can be modeled classically, with the Drude-Lorentz model. In this model, the interaction is treated by considering the oscillations of a free electron driven by the

electric field. The polarization induced by the oscillating electron leads to a relative permittivity of:

$$\varepsilon_r(\omega) = n^2 \left(1 - \frac{\omega_p^2}{(\omega^2 + i\gamma\omega)} \right), \tag{2.11}$$

where n is the index of refraction of the semiconductor and γ is a coefficient that determines the damping of the electron oscillation (related to the carrier momentum scattering time). The value ω_p is the plasma frequency, which is related to the carrier density, N, and electron effective mass, m_e^*, through:

$$\omega_p = \left(\frac{Ne^2}{\varepsilon_o m_e^*} \right)^{1/2}. \tag{2.12}$$

Since the relative permittivity and absorption coefficient are related by considering the attenuation of a wave in a medium, we find that

$$\alpha_{\text{free carrier}} = \frac{Ne^2\gamma}{m_e^*\varepsilon_0 nc} \frac{1}{\omega^2}, \tag{2.13}$$

i.e., the absorption coefficient is proportional to the free carrier density.[37]

2.4 Summary

In summary, the interaction of light with semiconductors can be described macroscopically by the quantities of reflectance, transmittance, and absorption coefficient. Reflectance and transmittance are directly related to the absorption coefficient, which is the most fundamental quantity of interest in ultrafast experiments. There are two main types of absorption mechanisms that will be used in this dissertation: interband absorption and free carrier absorption. Interband absorption involves the absorption of one photon or two photons in order to excite an electron from the valence band to the conduction band, whereas free carrier absorption involves the excitation of a free carrier already in the conduction or a carrier in the valence band to a higher energy still in the same band.

Chapter 3

Energy relaxation and carrier lifetime

3.1   Introduction

The energy relaxation and recombination of carriers that takes place after excitation is of great interest for a wide variety of applications and reasons. For example, it is necessary to know how long carriers will stay around so they can be used to carry information or deliver energy in a device. On the other hand, carrier lifetime limits the operation speed of optoelectronic devices since carriers involved in one operation need to disappear before the next opertation. Therefore, studies of carrier lifetime are essential to the development of new, more efficient devices. This chapter will begin with a discussion of what happens to carriers after excitation with specific emphasis on what happens after excitation by an ultrafast laser pulse. Then, the processes involved in the energy relaxation and recombination of carriers will be discussed. This will then be followed by a description of the ultrafast optical techniques that are used to observe such processes. Finally, there will be a discussion of results from a wide variety of materials, including Si/SiGe quantum wells, graphene, and carbon nanotubes.

3.2 Energy distributions of electrons excited by laser pulses

3.2.1 Energy distribution after excitation

Since ultrafast laser pulses will always have a finite energy spectrum, the resulting photoexcited electrons will have a similarly shaped energy distribution. In most cases, the spectrum of the ultrafast laser pulse is Gaussian:

$$I(\lambda) = I_0 e^{-4\ln(2)\frac{(\lambda-\lambda_0)^2}{b^2}}, \tag{3.1}$$

where b is the bandwidth (full width at half maximum), λ_0 is the center wavelength, and I_0 is the peak intensity. Therefore, as shown in Fig. 3.1(a), after excitation by such a laser pulse the energy distribution of the carriers can be approximately described by:

$$f(E) = \frac{N}{b}\sqrt{\frac{4\ln(2)}{\pi}}e^{-4\ln(2)\frac{(\lambda-\lambda_0)^2}{b^2}}, \tag{3.2}$$

where N is the total density of carriers excited (determined by the absorption coefficient, etc.) and $f(E)$ is the density of carriers per unit energy. This $f(E)$ should not to be confused with the distribution function, $f_0(E)$. In general $f(E)$ is defined here as $f(E) \equiv f_0(E)g(E)$, but in this case, where the carriers have not yet formed a Fermi-Dirac distribution, we know that $f(E)$ is given by Eq. (3.2). Strictly speaking, this initial distribution will also depend upon the density of states, which is different for each semiconductor. However, in all cases, including in the experiments discussed here, N is chosen so that the density of carriers at each energy is much less than the number of available states and therefore this energy distribution is accurate.

3.2.2 Thermalization

The initial energy distribution of the photoexcited carriers is considered to be nonthermal, since it cannot be described using a single temperature. However, as shown in Fig. 3.1(b), after some time, due to carrier-carrier scattering the carriers' energy will be redistributed, leading to the formation
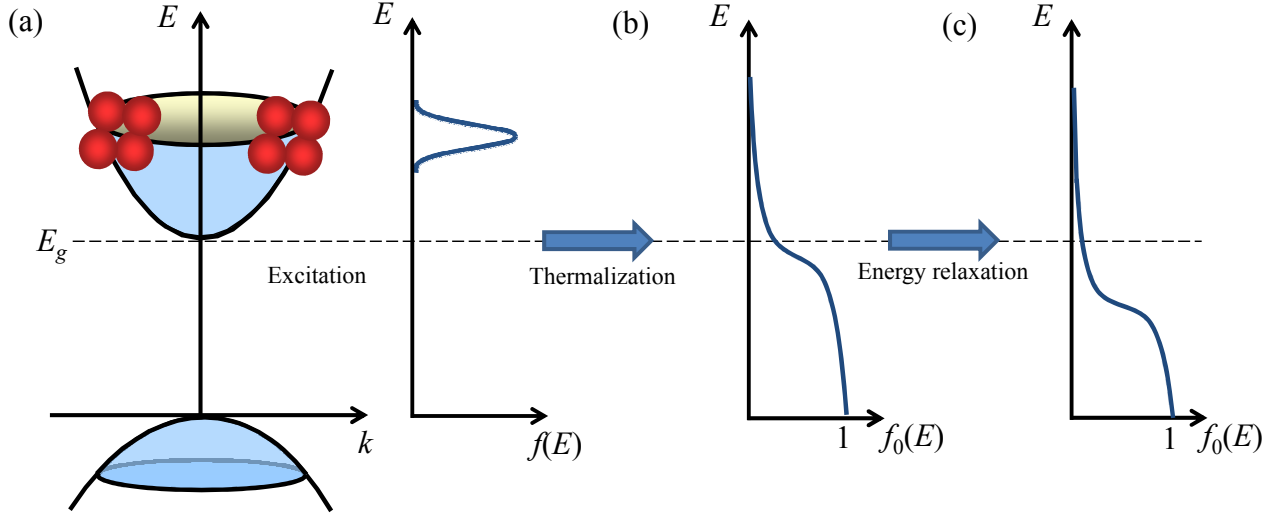
Figure 3.1: Schematic of the carrier energy distribution at various times after excitation. (a) Initial carrier energy distribution after excitation. (b) The carrier distribution function after thermalization (Fermi-Dirac with high temperature and Fermi level) (c) The carrier distribution function after energy relaxation (Fermi-Dirac with lower temperature and Fermi level). Panels (b) and (c) are greatly exaggerated for clarity.

of a Fermi-Dirac distribution:

$$f_0(E) = \frac{1}{1 + e^{(E-E_f)/k_B T}}, \tag{3.3}$$

where k_B is Boltzmann's constant, T is the carrier temperature, and E_f is the Fermi energy. The initial carrier temperature for this distribution, T_0, can be deduced by noting that the thermalization will not cause the total energy of the system of carriers to decrease. Therefore, the average energy of this distribution will be equal to the energy imparted by the laser pulse. If a laser pulse of angular frequency ω is incident on a semiconductor with a parabolic band structure, then the average energy of the electrons will be

$$E_0 = \frac{(\hbar\omega - E_g)m_h^*}{m_e^* + m_h^*}, \tag{3.4}$$

where m_h^* is the hole effective mass.[37] Since the average energy of a distribution of particles is given by:

$$\langle E \rangle = \frac{\int_{-\infty}^{\infty} E f_0(E) g(E) dE}{\int_{-\infty}^{\infty} f_0(E) g(E) dE}, \tag{3.5}$$

it is straightforward to calculate the initial carrier temperature if the density of states is known.

3.2.3 Energy relaxation and carrier recombination

After carriers are excited, besides thermalization there are many other processes that will occur. The two of interest for a wide variety of experiments are carrier energy relaxation and recombination. Due to the relatively high excess energies, i.e. the kinetic energy of the electrons in the conduction band, the primary method for energy relaxation is the emission of optical phonons. There are two main results to this. First, the temperature of the carrier distribution will decrease, as energy is removed from the system and given to the lattice, as shown in Fig. 3.1(c). The second result of this can be the formation of a local hot spot in the sample, where the lattice temperature is elevated. This may then affect the energy relaxation further, if the carriers gain some energy back from the optical phonon population. While optical phonon emission is a critical part of the energy relaxation of photoexcited carriers, the optical phonon energy cannot be derived in general, since it depends on the material being studied. The other process, carrier recombination, occurs when an electron in the conduction band drops back down to the valence band as it recombines with a hole. Both processes are typically modeled as causing an exponential decay in the carrier density at a specific energy. Therefore, the inverse of time constants from the exponential fits, i.e. $1/\tau_e$ and $1/\tau_r$ are essentially the energy relaxation and carrier recombination rates, respectively.

3.3 Experimental techniques: Time-resolved pump-probe

3.3.1 Introduction

Time resolved pump-probe techniques are some of the most fundamental techniques used in ultra-fast optical studies and as a result, all others discussed in this dissertation will expand upon these

basic principles. As the name suggests, pump-probe techniques involve at least two laser pulses: one that serves as a pump, exciting carriers in the material, and a second that serves as a probe, probing the excited carriers. By changing the relative times at which the pump and probe arrive at the sample, we can observe the density of carriers at the probing energy that were excited by the pump as a function of time. This is achieved by changing the travel distance of either the pump or probe using a mechanical stage, referred to as the delay stage, since it changes the time delay between the two pulses. Before going into the experimental details, a detailed discussion of the probing mechanisms are necessary.

After the carriers are excited by the pump pulse, they will form some energy distribution. As discussed in Sec. 3.2, this is initially a nonthermal distribution, but after some time it will become thermalized. In either case, the probing of carriers involves essentially the same processes as the pumping of carriers, but to measure the density of carriers at the probing energy, the absorption of the probe is constantly monitored, by measuring either its reflectance or transmittance (or both). Depending on the energy of the probe and the energy of the carriers being probed, in the simplest cases the absorption can either increase or decrease, and this change in absorption, $\Delta\alpha$ will provide information about the density of carriers at the probing energies.

3.3.2 Optical probing of carriers

3.3.2.1 Photobleaching

In this simplified, yet very common case, the absorption of the material depends only on the density of carriers present. At each energy there are only a limited number of available states for carriers to occupy. Once these states are significantly filled, absorption at this energy is reduced, and the semiconductor is considered to be "saturated" at this energy. Therefore, if we call N_{sat} the carrier density that causes the absorption coefficient to drop to 50%, then the the absorption coefficient can be modeled as

$$\alpha(n) = \frac{\alpha_0}{1 + \frac{N}{N_{sat}}}, \tag{3.6}$$

where α_0 is the absorption coefficient of the material when no carriers are present. So, the change in absorption caused by a nonzero carrier density will be equal to

$$\Delta\alpha = \alpha_0[(1 + N/N_{sat})^{-1} - 1]. \tag{3.7}$$

If $N \ll N_{sat}$, as is intentionally the case in pump-probe experiments, this can be approximated as

$$\Delta\alpha \approx -\frac{\alpha_0}{N_{sat}}N. \tag{3.8}$$

So, by measuring the change in absorption of the probe that is caused by the pump, we are essentially measuring the density of carriers excited by the pump.[38]

3.3.2.2 Photoinduced absorption

It is also possible, however, that the carriers excited by the pump will provide additional excitation pathways to the probe. This may be caused by several different mechanisms, but the term describing any increase in absorption caused by photoexcited carriers will be referred to as photoinduced absorption here. The most common mechanism is free carrier absorption, which was discussed previously, in Chapter 2. From that discussion, it is clear that

$$\alpha_{\text{free carrier}} \propto N. \tag{3.9}$$

Therefore, assuming there are no free carriers present before the pump has caused excitation, for free carrier absorption

$$\Delta\alpha = \alpha_{\text{free carrer}} \propto N. \tag{3.10}$$

3.3.3 Differential transmission and differential reflection

3.3.3.1 Differential transmission

In practice it is not possible to directly measure change in absorption of the probe that is caused by the pump. Therefore, either the change in transmission or the change in reflection of the probe is measured. As discussed in Chapter 2, the transmittance through a sample of thickness L with absorption coefficient α is $T = e^{-\alpha L}$. (This is assuming no reflection loss, which is irrelevant for this discussion.) So, the change in transmission caused by the pump-excited carriers, i.e. the difference between transmission with and without carriers, is

$$\Delta T(N) = T(N) - T_0 = e^{-\alpha(N)L} - e^{-\alpha_0 L}. \tag{3.11}$$

In the case that $\Delta \alpha L \ll 1$, again as is usually true experimentally, we then have

$$\frac{\Delta T(N)}{T_0} \approx -\Delta \alpha L \tag{3.12}$$

Therefore, by measuring the change in transmission of the probe caused by the pump, and normalizing this by the transmission of the probe with no pump present, we are essentially measuring the change in absorption of the probe caused by the pump. This normalized change in transmission of the probe caused by the pump is known as differential transmission. In experiment, the linear relationship between the differential transmission and the carrier density is always confirmed by measuring the differential transmission as a function of pump power, which is certainly proportional to the carrier density.

3.3.3.2 Differential reflection

Using a reflection to deduce the change in absorption on the other hand, can be much more complicated, depending on the substrate used, since multiple reflections should be taken into account. While this may make it difficult to determine the relationship between the sign of the change in reflection and change in absorption, since it may change depending on the layout of the sample,

its magnitude is still very useful. As mentioned for the differential transmission measurements, whenever using differential reflection, we verify that the magnitude of the differential reflection is indeed proportional to the density of carriers excited by the pump. Therefore, while it is sometimes difficult to determine the mechanism of absorption from the sign of the differential reflection, differential reflection still conveys the information of greatest interest in most experiments – the density of carriers at the probing energy.

3.3.4   Experimental configurations: Time-resolved pump-probe

A typical experimental setup for a pump-probe measurement is shown in Fig. 3.2. The relative distance that the probe and pump pulses travel is modified using the delay stage with a retrore-flecting mirror attached. This allows the time delay to be changed over a long range (as long as 1 ns, the maximum range of the stage) while still maintaining the same beam path. This stage, which is computer controlled, has a minimum step size of 300 nm, which corresponds to a delay time step size of 2 fs. Both the pump and the probe laser pulses are sent to the sample and focused tightly (typically around 2 to 5 μm) using a microscope objective lens. The pump and probe can be incident on the sample from either the same side (co-propagating, shown in the figure) or from opposite sides (counter-propagating, not shown in the figure), depending on the experimental concerns. Then, either the transmitted or reflected probe beam is collected by a detector for differential transmission or differential reflection measurements, respectively. Also, in some measurements both are detected simultaneously.

The laser system is summarized in Fig. 3.3. The Millenia Pro, a diode-pump continuous wave (cw) laser produces output with wavelength 532 nm. This then pumps the Tsunami, a Ti:Sapphire laser. For the experiments discussed here, the Tsunami is tuned in the range of 775 to 810 nm. With an 8.5 W Millenia Pro output, the typical output power of the Tsunami is about 2.3 W. The Tsunami produces 100 fs laser pulses with a repetition rate of 80 MHz via regenerative mode locking. The bandwidth is tunable and is typically maintained around 10.5 nm. The Tsunami then pumps OPAL, an optical parametric oscillator (OPO). The OPAL consists of a signal and an idler
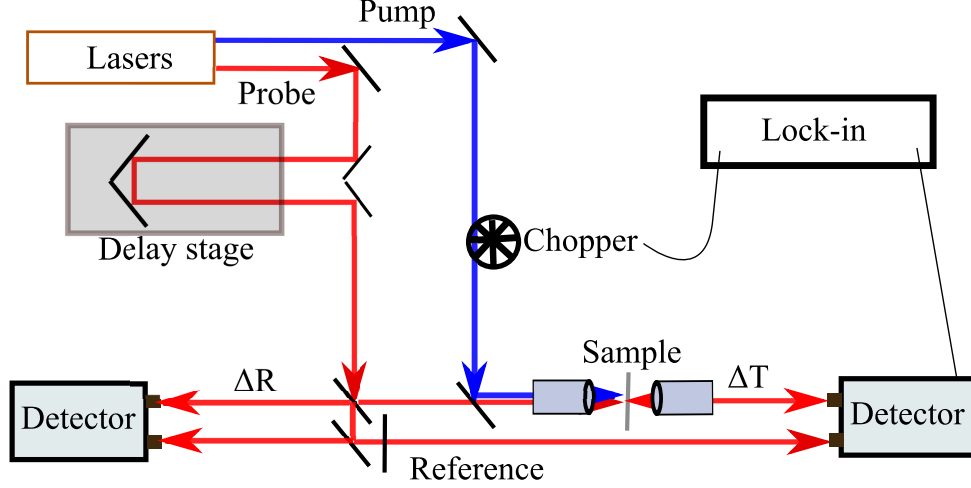
Figure 3.2: Experimental setup for differential reflection and differential transmission measurements with reference. This is the co-propagating configuration.

output, and with these two in combination with the tuning capabilities of the Tsunami, is capable of producing 130 fs pulses with wavelength tunable between 1.1 and 2.6 μ m and typical output power around 200 mW. Other wavelengths can also be obtained by second harmonic generation or sum frequency generation from various combinations of the outputs of the Tsunami and the OPAL.

In order to measure the differential signals, it is necessary to achieve a large signal to noise ratio, since the change in transmission or reflection can be smaller than 10^{-5} (0.001%) of the initial transmission or reflection. Fluctuations of the probe laser intensity however, can be as large as 0.1%. Therefore, since it is impossible to distinguish $T(N)$ from T_0 (i.e. to measure ΔT by measuring each individually) in a reasonable amount of time, lock-in detection techniques must be used. In order to measure ΔT or ΔR, we modulate the intensity of the pump beam with an optical chopper and send the transmitted or reflected probe beam to a photodiode, respectively. The output of the photodiode is sent to a lock-in amplifier that is referenced to the modulation frequency. The resulting output of the lock-in amplifier is a voltage that is proportional to the differential signal. To measure T_0 and R_0, we simply chop the probe and block the pump, and the resulting output of the lock-in amplifier is a voltage that is proportional to T_0. Finally, we divide these two voltages to obtain the differential signal ($\Delta T/T_0$ or $\Delta R/R_0$). (See Appendix A for a more detailed description of the lock-in detection techniques.)

23
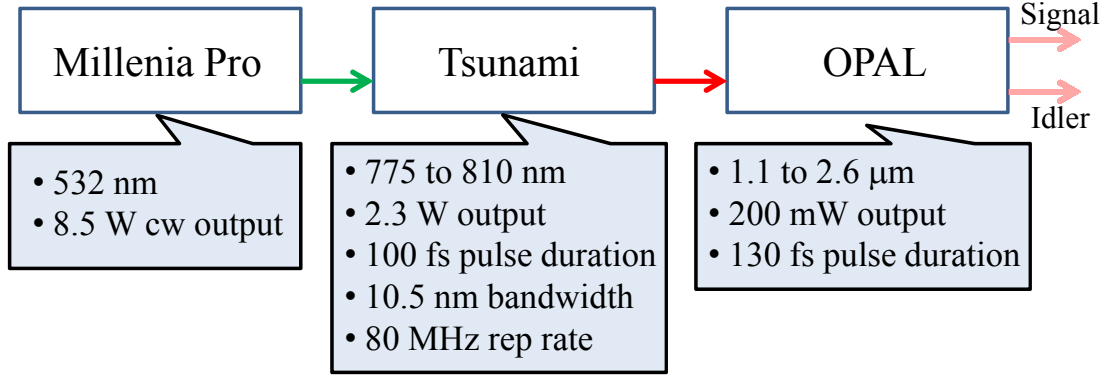
Figure 3.3: Summary of laser system and typical operating parameters for experiments in the dissertation.

In most measurements discussed in this dissertation, the modulation frequency is close to 2.1 kHz, and the lock-in time constant is between 300 ms and 1 s, depending on the signal level, with a filter slope of 12 dB/octave. With these conditions the laser noise can be decreased significantly. However, although the photodiode has adjustable gain, it is not possible to simply turn up the gain to increase the signal to noise ratio further – if the noise is predominantly from laser intensity fluctuations, it will also increase. On the other hand, if the noise is predominantly electronic, we will quickly reach a limit to our signal to noise ratio. Since the lock-in has a full scale sensitivity of 1 Volt, we cannot increase T_0 or R_0 by a very large amount in order to increase the signal to noise ratio before reaching saturation of the lock-in (electronic noise does not increase significantly with increasing gain for these photodiodes). If it is necessary to increase the signal to noise ratio further, we can use balanced photoreceivers – these output a voltage that is proportional to the difference in the optical powers to each photodiode. In this case, as shown in Fig. 3.2, we send part of the probe beam that does not make contact with the sample to the other arm of the photoreceiver, which we call the reference arm. We then chop the probe before the beams are split and send equal amounts of light to each arm of the photoreceiver using a polarizer, by making the voltage reported by the lock-in amplifier equal to zero. When chopping the pump, the lock-in will still report a voltage that is proportional to ΔT or ΔR, but now we are able to increase the gain of the photoreceiver to increase the differential signals and in turn increase the signal to noise ratio. With this technique, a noise level of 10^{-7} or less is achieved.

3.3.5 Summary

Time resolved pump-probe techniques allow carrier dynamics to be studied with a temporal resolution as small as 100 fs, which is limited only by the laser pulse durations. This is achieved by using two time-delayed short laser pulses: one to excite or pump carriers, and one to probe them. By measuring the differential transmission or differential reflection of the probe pulse, and verifying that it is proportional to the pump fluence, we are able to directly measure the density of the carriers at the probing energy as a function of time. This gives access to energy relaxation and carrier recombination processes that occur on ultrashort time scales. Using balanced detection techniques with a lock-in amplifier, we are able to measure differential transmission or reflection signals as small as 10^{-7}.

3.4 Results and discussion: Energy relaxation of carriers

3.4.1 Introduction

Time resolved ultrafast pump probe techniques are very common for studying the energy relaxation or recombination of carriers in semiconductors. As such, a wide variety of materials have been studied extensively such as bulk GaAs,[39–41] GaAs/AlGaAs quantum wells,[42] and epitaxial graphene,[43–45] just to name a few. Therefore, in this section I will mainly discuss results for a material that has been studied relatively less: reduced graphene oxide. These results are not only interesting for the sake of promoting this method of production of graphene as producing a material that retains the properties of intrinsic graphene, but also because they demonstrate the type of information that can be obtained from time resolved pump-probe measurements. After the discussion of the reduced graphene oxide results, similar results in Si/SiGe quantum wells and single-walled carbon nanotubes will be briefly discussed.

3.4.2 Reduced graphene oxide

3.4.2.1 Introduction

Graphene consists of a two-dimensional honeycomb lattice of carbon atoms. Heavily promoted for use in a wide variety of applications, including high speed transistors,[46] ultracapacitors,[47] and solar cells,[48] graphene has been studied extensively within the past five years since it was initially popularized by Nobel winners Andre Geim and Konstantin Novoselov.[24] For an in-depth review of the properties and previous ultrafast studies of graphene, see Appendix B. One important challenge in the progress of graphene lies in finding an efficient method of production that produces a material that keeps the properties of ideal graphene. Therefore, several different methods of production of graphene have been developed as discussed in Appendix B, and it is necessary that each type of graphene be characterized.

Ultrafast studies of graphene can be invaluable due to the relatively short carrier lifetime. One such type of graphene is graphene produced by the chemical reduction of graphene oxide, or reduced graphene oxide. This method can produce large quantities of graphene efficiently by spin-coating or solution printing techniques, but generally shows a lower mobility than what is present in pure graphene. Nevertheless, ultrafast studies of this type of graphene can be useful for possible future applications and studies. Here, two different types of experiments will be presented: one using the standard two-color pump probe configuration, and the second using a single color pump and two probes of different colors. The first essentially serves as a method for identifying that this type of graphene shows "graphene-like" properties. The second can be used to deduce import quantities, such as the optical phonon emission time and energy relaxation rate.

3.4.2.2 Ultrafast time-resolved pump-probe studies of reduced graphene oxide

In both experiments, graphene oxide flakes, synthesized using a modified Hummers' method,[49] were spin coated on a quartz substrate to form a film, which was then transformed to a multi-layer graphene film by thermal reduction at 1000 °C.[30] In order to obtain a thick sample, a high
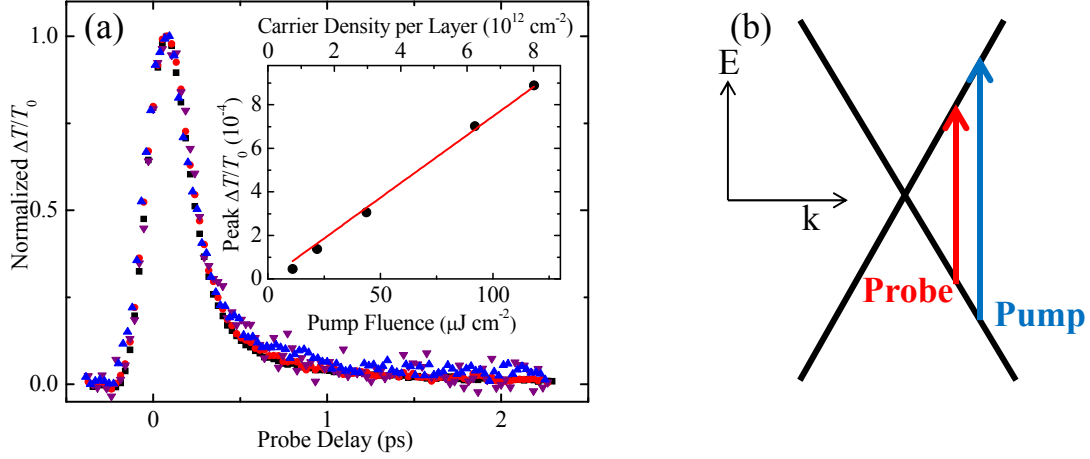
Figure 3.4: (a) Normalized $\Delta T/T_0$ for pump fluences of 22 (squares), 44 (circles), 92 (up-triangles), and 118 μJ/cm^2 (down-triangles) for a fixed sample temperature of 293 K. The inset shows the peak $\Delta T/T_0$ for various pump fluences. (b) Pump-probe scheme. Data from Ruzicka et al.[1]

concentration solution 4 mg/ml was used and the spin-coating was repeated four times. Since the thickness was controllable in this experiment, the differential transmission configuration was used – the thicker sample will lead to a larger signal for differential transmission, and the sign of the signal is more easily related to the sign of the absorption change. The number of graphene layers is determined to be about 50 by using an atomic force microscope. Additionally, the absorbance of the sample at 750 nm, is measured to be about 50%.

Carriers are excited with a pump pulse with a central wavelength of 750 nm, a pulse width of 0.1 ps, and a spot size of approximately 2.3 μm full width at half maximum (FWHM). The probe pulse for this experiment has a central wavelength of 810 nm, a pulse width of 0.19 ps, and was focused to a spot size of 1.2 μm FWHM. For this experiment, the probe is obtained from the output of the Tsunami and the pump from second harmonic generation of the signal output of the OPO, which is tuned to 1500 nm. The pumping and probing scheme is shown in Fig. 3.4(b). Since graphene has no band gap, excitation by either laser pulse gives carriers energy $\hbar\omega/2$. Hence, when carriers occupy the probing energy states, which are centered at 0.765 eV, half of the probe photon energy, the transmission of the probe through the sample will increase due to state filling effects. This is determined based on the wavelengths of the pump and probe, the band structure of graphene, and the positive sign of the differential transmission signal.

27
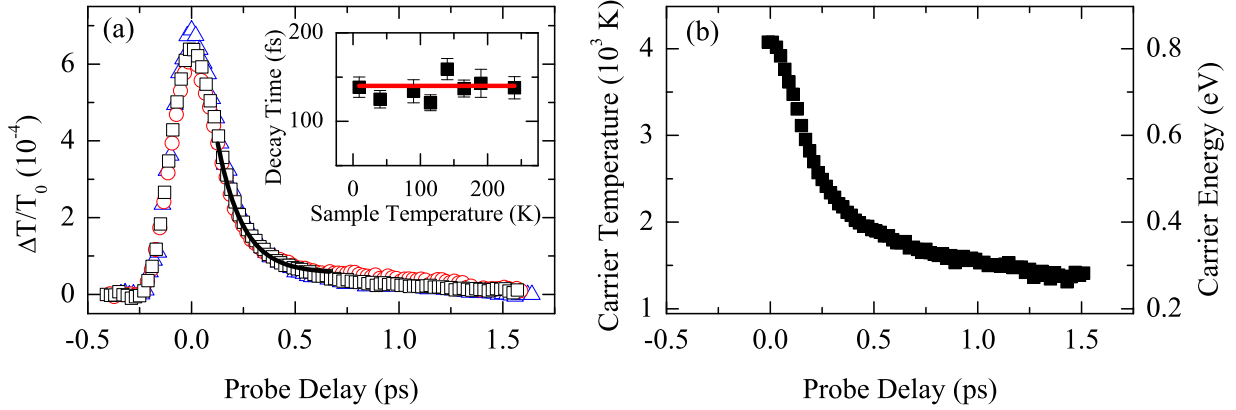
Figure 3.5: (a) $\Delta T/T_0$ measured for sample temperatures of 9 (squares), 115 (circles), and 240 K (up-triangles). The inset shows the decay time of the differential transmission signal for various lattice temperatures with an average (solid red line). (b) Carrier temperature (left axis) and average carrier energy (right axis) deduced from the $\Delta T/T_0$ curve at 9 K. Data from Ruzicka *et al.*[1]

First, in order to verify that $\Delta T/T_0 \propto N$, the peak $\Delta T/T_0$ was measured for various pump fluences, as shown in the inset of Fig. 3.4(a). (Data from Ruzicka *et al.*[1]) We observe that the peak $\Delta T/T_0$ is proportional to the pump fluence via a fit with the solid red line. This confirms that the change in absorption of the probe is due to state filling effects and that the differential transmission is in fact proportional to the carrier density. We then study the carrier dynamics for various pump fluences, and hence various carrier densities. Figure 3.4(a) shows the normalized $\Delta T/T_0$ for pump fluences of 22 (squares), 44 (circles), 92 (up-triangles), and 118 μJ/cm^2 (down-triangles) at room temperature. From these measurements it appears that the energy relaxation is not affected by the carrier density.

This result is in opposition to existence of a "phonon bottleneck" effect, which has been observed in epitaxial graphene on SiC.[50,51] Essentially, as the carriers relax via the emission of optical phonons, these phonons can feed energy back into the carrier population, leading to a slowing down of the energy relaxation. This may be hard to observe in these measurements however, since a wide range of carrier densities is not available, and the change in decay time due to this effect may be smaller than the uncertainty in such a measurement.

In order to investigate any possible effects of the lattice temperature on the carrier relaxation, it is varied from 9 to 300 K. The time dependent differential transmission is measured over this

28

lattice temperature range with a few examples shown as the symbols in Fig. 3.5(a). In these measurements, the peak energy fluence of the pump pulse is 118 μJ/cm^2. Using the absorption of 50%, the excited areal carrier densities in the first and the last graphene layers are estimated to be about 8.0×10^{12} cm^{-2} and 3.3×10^{12} cm^{-2}, respectively. (See Appendix D for information on how the carrier density is defined for graphene.) It is important to note that although the density in the front layer is about 20% of the density of states in graphene within the pump bandwidth (0.02 eV),[52] no significant absorption saturation is expected due to ultrafast thermalization of carriers: the carriers excited by the earlier part of the pump pulse are rapidly scattering to other energy states, making room for the excitation of carriers by the latter part of the pulse.

The temporal dynamics of the measurements in Fig. 3.4 and Fig. 3.5 are consistent with the following picture that has been established in previous studies of graphene, which was discussed in detail in Appendix B: After the carriers are excited with the pump pulse, they quickly reach a hot distribution via carrier-carrier scattering within a time scale on the order of 0.1 ps. Then, the carriers cool through carrier-phonon scattering (mainly optical phonon emission) on a slower time scale on the order of 1 ps. This energy relaxation causes the decrease in the carrier density in the probe states, and therefore the decrease in $\Delta T/T_0$. Carrier recombination occurs on a much longer time scale. Therefore, since the probe energy is rather high, it is not seen in this experiment. The effects of the lattice temperature on the relaxation of the carriers is quantified by fitting a portion of the differential transmission curve from 0.2 to 0.6 ps with a single exponential decay function. The solid line in Fig. 3.5(a) shows an example. The obtained decay time constants are plotted in the inset of Fig. 3.5(a). No systematic variation is observed, and an average value of 0.14 ps is obtained.

The fact that there is no dependence of the carrier energy relaxation on the lattice temperature is, however, not surprising. As stated previously, immediately after excitation, the carriers form a hot (i.e. thermalized) distribution. The energy relaxation that follows is then dominated by optical phonon emission. Due to the high excitation excess energy (0.83 eV), a large number of optical phonons is emitted, which causes a significant deviation of the phonon distribution in the excitation

spot away from the equilibrium distribution dictated by the sample temperature. Therefore, since the carriers experience a much higher lattice temperature than the temperature of other parts of the sample, the overall sample temperature has no influence on the carrier dynamics.

Assuming a Fermi–Dirac distribution is rapidly established right after the excitation, i.e. the carrier-carrier scattering time is much less than the optical phonon emission time, we can estimate the initial temperature of the distribution as discussed in Sec. 3.2.2. Using Eq. 3.5, and since the density of states of graphene is proportional to E (see Appendix B), the initial carrier temperature is approximately 4300 K. Since $\Delta T/T_0$ is proportional to the density of carriers at the probing energy, we can calculate how the temperature and the average energy of the carriers change over time using the measured $\Delta T/T_0$, and assuming the peak value of $\Delta T/T_0$ corresponds to a carrier temperature of 4300 K. These calculations are shown in Fig. 3.5(b) using data from the 9 K measurement—the calculations for measurements taken with different lattice temperatures give roughly the same values and show the same behavior. The temperature of the carriers decreases to approximately 1500 K within 1.5 ps, and then decreases much more slowly after this.

In summary, the ultrafast carrier dynamics in reduced graphene oxide are similar to those in other types of graphene samples indicating that graphene produced by this method is similar to intrinsic graphene. This is demonstrated by the fact that the carriers rapidly lose their energy and leave the probing window within 2 ps. Also, no dependence of the decay on carrier density was observed, which is in opposition to a phonon bottleneck effect. Additionally, no temperature dependence on this relaxation is observed, most likely due to the high local temperature experienced by the carriers. Finally, based on these measurements, it appears that the average energy of the carriers decreases by about 0.5 eV in 1.5 ps.

3.4.2.3 Two-probe study of hot carriers in reduced graphene oxide

In this experiment, hot carriers were studied in the same reduced graphene oxide thin films, but two probes of different colors were used instead of just a single one. By precisely overlapping the two probes in time, and measuring the time between which the differential transmission signals

peak with each probe, we are able to monitor the density of carriers at two different energies for various times after excitation. From this, it is then possible to find the exact time it takes for carriers to relax from the first probe energy to the second. This has several advantages over the previous technique. First, the optical phonon population should not be as high at the early time delays, so any effects of those on the energy relaxation will not be observed. Second, for this same reason we are able use the time difference to more accurately determine an energy relaxation rate, assuming the carrier distribution is immediately thermalized.

Figure 3.6 summarizes the experimental setup and pump/probe scheme. Carriers are excited with an 800-nm, 100-fs pump pulse, which is focused to a size of approximately 2.3 μm FWHM. This is obtained from residue Ti:Sapphire laser, which passes through the idler output of the OPO. To detect the carriers, we use one of the two different probe pulses of central wavelengths 1714 and 857 nm, respectively. The 1714-nm probe is produced from the idler output of the OPO, and the 857-nm probe is obtained from second-harmonic generation of the 1714-nm probe using a beta barium borate (BBO) crystal. The pulse width of each is 80 and 150 fs, respectively, and both are focused to a spot size of approximately 1.5 μm (FWHM). The two probe pulses are precisely overlapped using sum-frequency generation in a GaAs sample grown along the [110] direction that is mounted directly next to the graphene sample. By repeatedly obtaining the maximum sum-frequency generation (and therefore best temporal overlap), we find that we can consistently overlap the two probe pulses in time with an error smaller than 5 fs.

The differential transmission of each probe is measured with time, while pumping an average areal carrier density of 2.3×10^{13} cm^{-2}, as shown in Fig. 3.7(a). (Data from Ruzicka et al.[2]) The 0-ps probe delay is defined arbitrarily here, since only the difference in time between the peaks of the two curves is relevant. However, the 0-ps probe delay is expected to be very close to the peak of the 857-nm probe since the photon energies of the 800-nm pump and the 857-nm probe are close. The inset of Fig. 3.7(a) shows another scan that was taken closer to the peaks. The peak of the differential transmission with the 1714-nm probe occurs approximately 47 fs after the peak of the 857-nm probe.
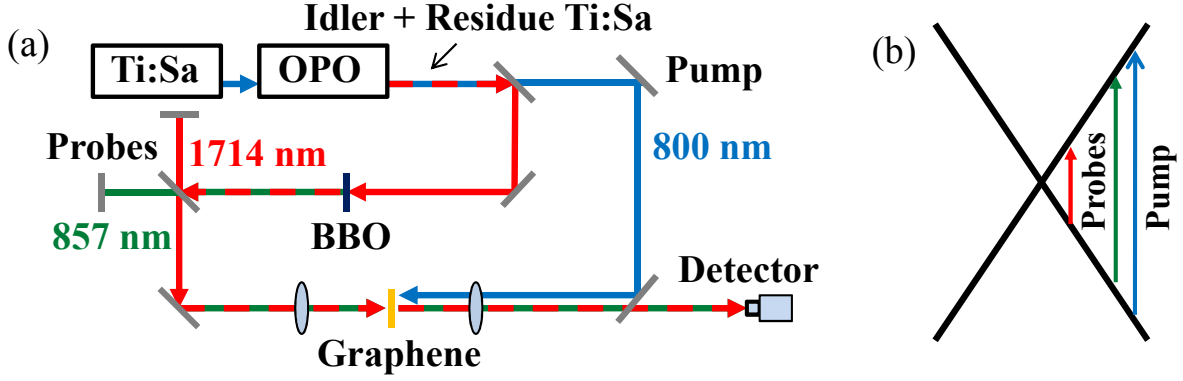
Figure 3.6: (a) Experimental setup for two-color probe experiment. (b) The excitation and probing scheme.

In order to investigate the dependence of the relative peak times on the carrier density, this measurement is repeated with various carrier densities by changing the pump fluence. The results are summarized in Fig. 3.7(b). The peak time of the 1714-nm probe changes systematically with the carrier density, while the peak time of the 857-nm probe remains unchanged. At a density of 1.5×10^{12} /cm^2, the 1714-nm probe peak occurs about 92 fs later than the 857-nm probe peak. When the density is increased to 3×10^{13} /cm^2, the 1714-nm peak shifts earlier, occurring about 37 fs after the 857-nm peak. As discussed in Appendix B, it is reasonable to assume that the thermalization occurs rapidly and therefore when the differential transmission of either probe reaches a peak, the distribution can already be described using Fermi-Dirac statistics. Hence, the data can be interpreted as follows: When the differential transmission (and therefore the density of carriers seen by the probe) peaks for the 857-nm (1714-nm) probe, the average energy of the carriers is approximately equal to the central probing energy of 0.72 eV (0.36 eV), half of the probe photon energy. The difference in the peak times gives the time it takes for the average carrier energy to decrease by 0.36 eV (from 0.72 to 0.36 eV). For example, in Fig. 3.7(a) the energy relaxation of 0.36 eV takes 47 fs. This corresponds to an energy relaxation rate of about 8 meV/fs. We can extend this analysis even further, since it is known that the dominant energy relaxation channel is the emission of G-mode optical phonons with an energy 0.195 eV.[53] Therefore, under the previous assumptions, at this carrier density, the optical phonon emission time is $47 \times (0.195/0.36) = 25$ fs.
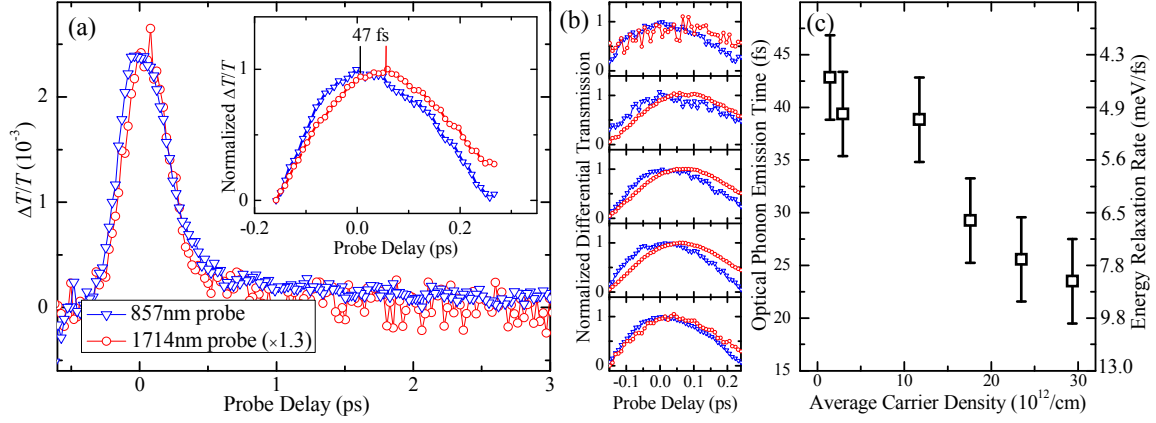
Figure 3.7: Differential transmission in reduced graphene oxide for the 857-nm (triangles) and 1714-nm (circles) probes with an average areal carrier density of 2.3×10^{13} /cm². The inset shows another scan performed closer to the peak. (b) Normalized differential transmission in reduced graphene oxide with the 857-nm (triangles) and 1714-nm (circles) probes with average areal carrier densities of 1.5, 2.9, 11.7, 17.6, and 30×10^{12} /cm² from top to bottom. (c) Energy relaxation rate and optical phonon emission time deduced from these measurements. Data from Ruzicka et al.[2]

Using the same analysis for different pump powers leads to the results in Fig. 3.7(c). At a density of 1.5×10^{12} cm^{-2}, the optical phonon emission time is about 50 fs, corresponding to an energy relaxation rate of about 4 meV/fs. When the density is increased to 3×10^{13} cm^{-2}, the optical phonon emission time decreases to about 20 fs, corresponding to an energy relaxation rate of about 10 meV/fs. The values of the optical phonon emission time as well as the density dependence determined in this way are reasonably consistent with recently theoretical calculations.[54,55]

3.4.2.4 Summary

Clearly, these results show a difference in the energy relaxation rate. For a carrier density on the order of 10^{12} per layer, in the first experiment, it appears that the average energy of the carriers decreased by about 0.5 eV in 1.5 ps, while the second experiment shows that the average carrier energy decreased by about 0.36 eV in 47 fs. The reason for the discrepancy most likely lies in the difference in measurement method. Wang et al. found that, by modeling differential transmission measurements in epitaxial graphene with coupled electron and optical phonon rate equations, after the first 200 to 300 fs, the optical phonon population reaches a maximum, which presents a bot-

tleneck to subsequent cooling.[51] Since, as demonstrated in the first experiment, reduced graphene oxide appears to behave the same as epitaxial graphene, it is most likely the case that the same is occurring here. Therefore, the slower decrease in average carrier energy observed in the first experiment is most likely caused by this same bottleneck effect: Since the two-probe study relies on determining the position of the peaks of the differential transmission curves, which occur within 50 fs or so of carrier excitation, it has the advantage of not being influenced by a large optical phonon population. Hence, the second method measures relaxation of carriers from optical phonon emission alone, while the first method is actually measuring the relaxation of carriers from optical phonon emission as well as energy gained back from the optical phonons.

In summary, reduced graphene oxide was studied using ultrafast pump-probe techniques. First, a single probe was used to measure the differential transmission decay time as a function of carrier density and lattice temperature. The relaxation of the carriers from the probing energy was found to be independent of both. Also, the decay time was found to be similar to that observed in other types of graphene, and therefore this type of graphene is expected to have similar properties to those of pure graphene and may be useful due to its favorable production process. Additionally, reduced graphene oxide was studied using a two-color probe scheme, which allowed us to deduce the optical phonon emission time. The optical phonon emission time was found to decrease with increasing carrier density, which is consistent with recent theoretical calculations.

3.4.3 Other semiconductors

These techniques can be applied to a wide variety of semiconductors, provided the band gaps are reachable by the laser system. Two such examples are Si/SiGe quantum wells and single walled carbon nanotubes. Strained $Si/Si_{1-x}Ge_x$ structures have attracted attention for several years due to their possible electronic and photonic applications. Specifically, they can be ideal for use in integrated optoelectronic devices: the Si is present for easy integration, and by controlling the relative concentrations, i.e. x, the strain can be actively controlled, which changes the band gap and therefore the optical properties.[33] Carbon nanotubes have many possible applications as well

such as solar cells,[35] supercapacitors, and composite materials.[36] Therefore, it is important for both materials to obtain information about the carrier lifetime and/or energy relaxation rate, which can be inferred from time resolved pump-probe experiments.

The Si/SiGe quantum well sample is grown by solid source molecular beam epitaxy on Si (001) wafers, as discussed by Wang et. al.[56] It consists of a thin layer of Si grown at low temperature (650 °C) on a thick buffer layer of $Si_{1-x}Ge_x$ (4000 Å) as a virtual substrate, and ten periods of $Si/Si_{1-x}Ge_x$ quantum wells. Hence, the sample is on a thick wafer and is therefore not transparent. To study the carrier dynamics we use a 170 fs, 737 nm pump pulse and a 170 fs, 810 nm probe pulse, both focused to a spot size of about 3 μm FWHM. The 737 nm pump pulse is obtained from second-harmonic generation using a BBO crystal of the signal output of the OPO, which is tuned to 1474 nm. The carbon nanotube sample is over 90% semiconducting and has a diameter distribution as described by Ren et al.[35] In order to study the carrier dynamics of this sample, we use the same 810 nm probe pulse and a 750 nm pump pulse, obtained as previously discussed. Both are focused to the sample to a spot size of approximately 2 μm full width at half maximum (FWHM).

Results of the basic time resolved pump-probe measurements for both materials are shown in Fig. 3.8. Figure 3.8(a) shows the differential reflection for the Si/SiGe quantum well sample as a function of probe delay for a peak pump fluence of 110 μJ/cm^2 and the inset shows the peak differential reflection as a function of pump fluence. The decay of the differential reflection is best fit as a bi-exponential (red line), which results in a fast decay time of 13 ± 2 ps and a much slower decay time of 495 ± 3 ps. The first decay time is most likely caused by the energy relaxation of carriers and the second is caused by carrier recombination and therefore reflects the carrier recombination rate. Additionally, the rising time is approximately 1 ps – i.e. it is longer than the pulse width of 170 fs. Therefore, this time indicates the time it takes for the carrier distribution to reach a peak in density at 1.53 eV, after starting out with average energy 1.68 eV.

Figure 3.8(b) shows the results for the single walled carbon nanotubes. The inset shows the peak differential reflection measured as a function of peak incident pump fluence. The main part
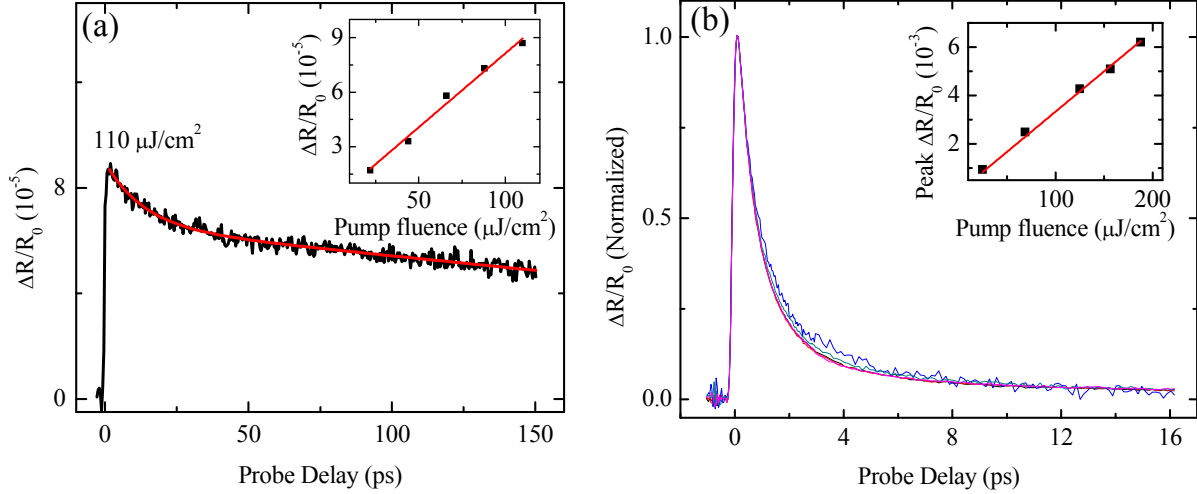
Figure 3.8: (a) Time resolved differential reflection measurement of Si/SiGe quantum wells with a 110 μJ/cm^2 peak pump fluence (737 nm pump and 810 nm probe). (b) Differential reflection for single walled carbon nanotubes as a function of probe delay normalized for various pump fluences. Both insets show the peak differential reflection as a function of pump fluence with a linear fit.

shows the normalized differential reflection for fluences of 25, 68, 125, 155 and 188 μJ/cm^2, which we investigate to see if there is any dependence of the relaxation on carrier density (i.e. any strong hot phonon effects). It appears that the signal decays as a bi-exponential with time constants of 0.66 ± 0.02 ps and 2.8 ± 0.2 ps, which are independent of pump fluence. Since both decay times are relatively short, the first may be caused by thermalization and the second by carrier relaxation. These two measurements demonstrate how simple it is to use time resolved pump-probe measurements on a wide variety of semiconductors to extract information about the carrier lifetime and carrier energy relaxation.

3.5   Summary

Ultrafast time-resolved pump-probe techniques can be used to obtain information about the lifetime and energy relaxation rate of carriers in semiconductors. These techniques involve measuring either the differential reflection or differential transmission of a probe pulse as a function of time delay between the probe and pump pulses. The differential transmission and differential reflection is proportional to the density of carriers excited by the pump, which can be easily verified exper-

imentally. Results were presented on reduced graphene oxide. In these experiments it was found that the differential transmission displays a behavior that is similar to other types of graphene, and therefore graphene produced in this way is similar to intrinsic graphene. Also, using a two-color probing scheme, the optical phonon emission time can be deduced, and for a carrier density of 1.5×10^{12} cm^{-2}, the optical phonon emission time is about 50 fs. When the density is increased to 3×10^{13} cm^{-2}, the optical phonon emission time decreases monotonically to about 20 fs. This decrease is consistent with recent theoretical calculations of the carrier density dependent optical phonon emission time. Additionally, results on Si/SiGe quantum wells and carbon nanotubes were presented, in order to show the applicability of these techniques to a wide variety of materials.

Chapter 4

Diffusive carrier transport

4.1 Introduction

Transport of charge carriers in semiconductors plays an essential role in several electronic applications. There are two main mechanisms for carrier transport: drift and diffusion. The key parameters describing the two processes are mobility and diffusion coefficient, respectively, and the two are related by the Einstein relation. Since the transport described by these two quantities is determined to a great extent by scattering, both of these are related to the microscopic quantities of mean-free time and mean-free path. For photoexcited carriers, both electrons and holes are present. Therefore, due to the Coulomb attraction between the two, they move as a pair through the semiconductor. Hence, the transport of such electron-hole pairs is known as ambipolar transport and the diffusion is known as ambipolar diffusion. Ambipolar diffusion plays a very important role in a wide variety of optoelectronic devices. For example, in a photovoltaic device, the absorbed photon energy is transferred by diffusion of the electron-hole pairs before the charge separation.

Ultrafast lasers have the unique ability to measure certain properties of a material without making a physical contact. Of particular interest for a wider variety of semiconductor applications is the mobility, which essential determines the speed and efficiency of any possible device that may be created from the material. The mobility is typically measured by the application of electri-

cal contacts for Hall effect measurements, which directly relates the mobility to the more easily measurable quantities of resistivity and current. While ultrafast laser techniques cannot directly measure the mobility of a semiconductor, they do have access to real-time and real-space carrier dynamics, which allows for the direct observation of the diffusion of carriers. This in conjunction with the ability to accurately control the energy and density of carriers excited by laser pulses makes it possible for ultrafast laser techniques to provide a non-contact and noninvasive method to measure the mobility of carriers in semiconductors.

4.2 Diffusion of carriers in semiconductors: Theoretical discussion

4.2.1 Diffusive transport and carrier mobility

A current in a semiconductor can be caused by two different mechanisms: drift and diffusion. The first mechanism, drift, involves the movement of charge due to an electric field. The force on a particle of charge q due to electric field E will be $F = qE$. However, since scattering occurs as the particle will collide with other particles or impurities in the crystal, the particle cannot accelerate indefinitely. This results in repeating periods of acceleration followed by a reduction of velocity as the particle undergoes a collision. The average drift velocity of the particle, i.e. the average velocity attained between collisions is defined as

$$v_d = \mu E, \tag{4.1}$$

where μ is known as the mobility of the particle. The drift current density will then be

$$J_d = qnv_d = qn\mu E, \tag{4.2}$$

where n is the density of particles. The particle charge q can be either $-e$ for electrons or e for holes, where e is the magnitude of the electron charge. The total drift current density will be equal to the sum of the electron and hole drift current densities.

Of particular interest here is the second mechanism, diffusion, since this is directly observable using temporally and spatially resolved ultrafast pump-probe techniques. The classical definition of diffusion is "the process whereby particles flow from a region of high concentration toward a region of low concentration."[9] Therefore, it is straightforward to define the diffusion current density as being proportional to the gradient of the carrier density distribution, i.e.

$$J_f = qD\nabla n. \tag{4.3}$$

Here D is the diffusion coefficient (a positive constant with units cm^2/s) and n is the carrier density as a function of (x, y, z).

Finally, the total current density is equal to the sum of the drift and diffusion current densities:

$$J_{tot} = qn\mu E + qD\nabla n. \tag{4.4}$$

Interestingly, although the processes seem quite different, the mobility and diffusion coefficient are related through the Einstein relation:

$$\frac{D}{\mu} = \frac{k_B T}{e}. \tag{4.5}$$

This relation arises through the fact that even if the total current density is zero in a semiconductor, a nonzero spatial carrier density distribution with a nonzero gradient may still exist. Then, by Eq. (4.4), the two components must be balanced. This is achieved by an electric field caused by the nonuniformity of the spatial distribution of carriers: The electric field will be $\mathbf{E} = -\nabla\phi$ where ϕ is the electric potential, and at each position ϕ depends on the energy of the carriers, which itself has an energy distribution (Fermi-Dirac or Boltzmann), hence the proportionality to $k_B T$.

Therefore, by measuring the diffusion coefficient and with knowledge of the carrier temperature, we are able to deduce the carrier mobility. As discussed in Chapter 3, the temperature can be calculated as from the pump wavelength as long as the band structure and density of states are known. Additionally, the diffusion coefficient can be directly measured using spatially and temporally resolved ultrafast pump-probe techniques, which will be discussed in the following sections.

4.2.2   Diffusion of a Gaussian spatial distribution of photoexcited carriers

In the experiments discussed here, the spatial distribution of carriers is always Gaussian in shape, since that is the shape of the laser spot used for excitation. Therefore, it is important to discuss the particular case of the diffusion of a Gaussian spatial distribution of carriers. For simplicity, we define the carrier density spatial profile in spherical coordinates at time t as $N(r,t)$. If at time $t = 0$ this is Gaussian, then the profile will have the form

$$N(r,0) = N_0 e^{-4\ln(2)r^2/w_0^2}, \tag{4.6}$$

where w_0 is the FWHM at time $t = 0$.

Since the photoexcitation will lead to the generation of free electrons and holes, which are oppositely electrically charged, the two will attract each other and move as a pair. Therefore, the observation of any transport of N will not be unipolar, i.e. the transport of either electrons or holes, but will instead be ambipolar. This means that the diffusion coefficient or mobility that is observed will be the effective value of the electron-hole pair. For this reason, it is important to add the subscript a, to denote that the transport processes are ambipolar and not unipolar.

In order to see how the spatial carrier density distribution will change during the transport process we use the charge continuity equation, which gives the relationship between the change in time of the distribution of carriers and the change in space:

$$\frac{\partial N}{\partial t} = \frac{1}{q}\nabla \cdot J_{fa} = D_a \nabla^2 N. \tag{4.7}$$

This assumes that the total density of carriers is constant, i.e. no carrier recombination or generation is occurring. It is easy to check that a solution to this equation is another Gaussian, but with a linearly increasing $w^2(t)$:[57]

$$N(r,t) = N_0 \left(\frac{w_0^2}{w^2(t)} \right) e^{-4\ln(2)r^2/w^2(t)}, \tag{4.8}$$

where

$$w^2(t) = w_0^2 + 16\ln(2)D_a t. \tag{4.9}$$

In the experiment, it is possible and likely that carrier recombination is occurring during the diffusion process. However, the only effect that this will have on $N(r,t)$ is to decrease its height over time. This amounts to adding a factor of $-t/\tau$ in the exponential, where $1/\tau$ is the carrier relaxation rate. The overall result, however is still the same: by measuring the width of the Gaussian profile over time, and fitting this squared with time, we can deduce the ambipolar diffusion coefficient, D_a, from the slope.

Finally, using the ambipolar transport equations derived by Neamen, we can relate the ambipolar diffusion coefficient to the unipolar diffusion coefficients.[9] Since we inject an equal density of electrons and holes, the ambipolar diffusion coefficient will be

$$D_a = \frac{D_e D_h}{D_e + D_h}, \tag{4.10}$$

where D_e and D_h are the diffusion coefficients for electrons and holes, respectively.

4.2.3 Summary

Carrier transport is caused by two main mechanisms: drift and diffusion of charge carriers. The key parameters for the two are the mobility and the diffusion coefficient, respectively. Although they are different processes, the two are in general related via Einstein's relation, which states that the diffusion coefficient to mobility ratio is equal to $k_B T/e$. Diffusion of a Gaussian spatial

distribution of carriers will cause the distribution to remain Gaussian, but have a decreased height and a linearly increasing squared FWHM with time. Therefore, by measuring the FWHM of the spatial profile as a function of time, we are able to deduce the diffusion coefficient. Additionally, if the pumping energy and band structure are known, we can use the diffusion coefficient to deduce the mobility.

4.3 Experimental techniques: Spatially and temporally resolved pump-probe

4.3.1 Introduction

Previously, ambipolar diffusion has been studied by several optical techniques including transient grating and photoluminescence. In transient-grating experiments, a periodic spatial distribution of carriers is generated by the interference of two laser pulses, which are incident on the sample from different angles. The decay of this periodic distribution is then detected by the diffraction of a third pulse, and the diffusion coefficient can be deduced from this decay.[12–17] Photoluminescence spectroscopies, both in the time-of-flight configuration[22,23] and the spatially resolved geometry,[18–21,57–60] have also been applied to study ambipolar diffusion. The use of spatially and temporally resolved pump-probe techniques to measure ambipolar diffusion, however, is very rare. Yet, this technique has several advantages over the others. First, relatively small diffusion coefficients can be measured by focusing the laser spots tightly and observing the diffusion over a relatively long probe delay (about 1 ns maximum for the configuration used in these experiments). Second, these techniques allow the direct observation of the expansion of the carrier density profile, and therefore provide information about any changes in the diffusion coefficient that may be caused by carrier or lattice temperature.

The rarity of such spatially and temporally resolved pump-probe techniques is due in part to the difficulty of achieving a high spatial resolution. However, this is achievable by tightly focusing the

laser spots down to roughly 2 μm with objective lenses with a high numerical aperture (NA~ 0.4). In most pump-probe experiments common lenses are usually used, which typically results in laser spots on the order of 100 μm. This ability to focus the beam to a small spot size in addition to the ability to temporally and spatially control the overlap of the pulses allows the direct observation of carrier diffusion and in most cases, the deduction of mobility from this.

4.3.2 Experimental configurations: Spatially and temporally resolved pump-probe

These experiments are nearly exactly the same as the time-resolved pump-probe experiments discussed in Chapter 3. The only difference is that now we include the ability to control the spatial overlap of the pulses in addition to the temporal overlap. This allows us to go to a certain time delay and measure the differential reflection or differential transmission as a function of the position of the probe spot relative to the pump spot, which essentially amounts to measuring the spatial distribution of the carrier density as a function of time.

The control of the spatial overlap of the pump and probe pulses can be achieved in two different ways, depending on if the co- or counter-propagation configuration is used. In the co-propagating configuration, as shown in Fig. 3.2, the overlap is controlled by slightly changing the angle of the beam splitter that sends the probe or pump to the objective lens. This small change in angle will lead to a shift in the relative position of either beam on the sample. The change is later calibrated to a real distance change on the sample. In the counter-propagating configuration, either one of the pump or probe objective lens is mounted on a linear computer-controlled stage. By moving the stage a certain distance, the relative positions of the probe and pump are changed by that same distance.

4.3.3 Deduction of carrier diffusion coefficient and mobility from ultrafast pump-probe measurements

Finally, in order to deduce a diffusion coefficient, this spatial scan procedure is repeated at various time delays. Since the pump laser spot has a Gaussian shape, the spatial profile at each time delay will also be Gaussian. It is in fact a convolution of the Gaussian probe spot and the Gaussian carrier density profile. The spatial profiles are all fit to a Gaussian curve using the Levenberg-Marquardt algorithm through Origin software. From this we obtain the FWHM as a function of probe delay. The slope of a linear fit of the FWHM squared with probe delay divided by $16\ln(2) \approx 11$ then gives the diffusion coefficient, which is typically reported in units of cm^2/s.

Three important things to note are as follows: First, the decrease in height of the spatial profiles over time that is caused by the energy relaxation or carrier recombination does not affect the result. This affects the height, N_0, of the Gaussian curve and not its width. Second, the fact that this is a convolution of the carrier density profile with the probe laser spot also does not affect the result: The width of the spatial profile will be $w = \sqrt{w_N^2 + w_p^2}$, where w_N is the width of the carrier density distribution and w_p is the width of the probe spot. Therefore, since w_p^2 is present on both sides of Eq. (4.9), it will cancel. Third, while Eqs. (4.8) and (4.9) describe a three dimensional diffusion process, in the experiments presented here, the carriers essentially only diffuse in two dimensions. This is because the samples are relatively thin compared to the Raleigh range of the pump and probe beams, i.e. the distance over which the beams focus is larger than how far the carriers can diffuse into the sample along the beam propagation direction.

In order to determine the mobility from the diffusion coefficient for such measurements, it is necessary to know the carrier temperature, T. While this can change quickly while the carriers cool as they collide with the lattice and emit optical phonons, we are always able to at least obtain reasonable estimates based on the minimum and maximum temperatures that are possible. The maximum temperature possible is that caused by the initial excess energy given to the carriers after excitation. This can be calculated as described in Chapter 3, Sec. 3.2.2. The minimum temperature possible is that of the lattice, which will be the case once the carriers reach thermal

equilibrium with it.

4.3.4 Summary

Spatially and temporally resolved pump-probe techniques are essentially the same as time resolved techniques except for the added ability to measure the differential reflection and differential transmission as a function space in addition to time. A high spatial resolution is achieved by using a microscope objective lens to focus the laser spots. Then, the differential transmission or reflection can be measured as a function of time and space by going to a particular time delay and scanning either pump or probe with a mirror or lens. From Gaussian fits of the width of the profiles as a function of time, we are then able to deduce the diffusion coefficient and subsequently the mobility.

4.4 Results and discussion: Diffusion of carriers in bulk GaAs

4.4.1 Introduction

Similar to the techniques discussed in Chapter 3, spatially and temporally resolved pump-probe techniques can be applied to a wide variety of semiconductors to measure the carrier diffusion coefficient. In this section, results on bulk GaAs will be presented in detail, since it is easy to compare the measured diffusion coefficient with mobilities that have been measured by others, as this material has already been studied extensively, but there have been very few previous measurements of the diffusion coefficient in the bulk. After this, results for other materials including reduced graphene oxide, epitaxial graphene, CVD graphene, single walled carbon nanotubes and Si/SiGe quantum wells, will be presented, but with a more brief description, since each experiment follows the same procedure and involves the same measurements.

4.4.2 Bulk GaAs

While GaAs is most well known for being an ideal platform for the study of spintronics,[61] it is also an ideal material for the demonstration of a wide variety of ultrafast measurement techniques such as optical injection and detection of charge currents,[62] and detection of spin currents by second harmonic generation.[63] Therefore, it is a good material to begin with to demonstrate the measurement of ambipolar diffusion using the techniques discussed in this chapter. So far, most experimental studies of ambipolar diffusion in GaAs have been performed on GaAs quantum-well samples.[22,23,57,64–71] However, since the scattering rates of carriers in quantum-well samples are different from bulk crystals due to the change in the density of states caused by the quantum confinement, the diffusion coefficients in quantum-well samples are different from those in bulk samples. Furthermore, in quantum-well samples, the interface between the quantum well and the barrier causes additional scattering mechanisms. While quantum-well samples have been studied extensively,[22,23,57,64–71] studies on bulk GaAs are rare.[17]

The sample studied for this experiment is a 400 nm GaAs layer on a glass substrate. Carriers are injected with a 750 nm, 100 fs pump pulse focused to a spot size of 1.6 μm, which is obtained from second harmonic generation of the signal output of the OPO. The carriers are probed with a 100 fs probe pulse with a central wavelength of 800 nm, which is obtained from the Ti:sapphire laser and focused to a spot size of 1.2 μm. For this experiment, we use the counter-propagating pump-probe configuration and measure the differential transmission, which we confirm is proportional to the carrier density.

In order to verify that the carrier density profile is symmetric, we first acquire the differential transmission at different probe delays by scanning the probe spot in the x-y plane. Figure 4.1 shows the measured $\Delta T/T_0$ as a function of x and y for probe delays of 0, 10, 20, and 30 ps. (Data from Ruzicka *et al.*[3]) Here, and in general, $x = y = 0$ is defined as the position where the centers of the pump and the probe spots overlap, and the probe delay $t = 0$ is still defined as the time when the peaks of the pump and the probe pulses overlap. In this measurement, the pump pulse injects an average carrier density of about 10^{17} cm^{-3}, and the sample is cooled to 10 K. At $t = 0$, the
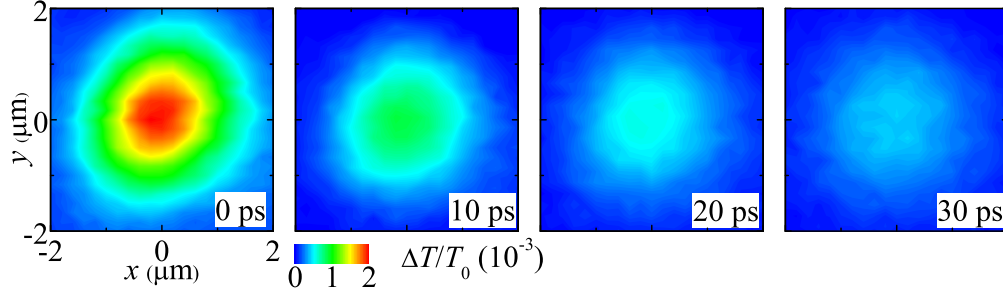
Figure 4.1: Differential transmission for the bulk GaAs sample as a function of position in the *x*-*y* plane for probe delays of 0, 10, 20, and 30 ps, with a sample temperature of 10 K. Data from Ruzicka *et al.*[3]

Gaussian shape of the $\Delta T/T_0$ profile is consistent with the pump and probe laser spots, since the size is the same as a convolution of the pump and probe spots. At later times, the profile remains Gaussian, as expected from the diffusion model described in Sec. 4.2.2, and becomes lower and wider due to the ambipolar diffusion.

Since no anisotropic diffusion is observed according to Fig. 4.1, to quantitatively study the diffusion process and deduce the ambipolar diffusion coefficient, it is sufficient and more efficient to measure the cross sections of the profile on the x-axis for a large number of probe delays. Figure 4.2(a) shows $\Delta T/T_0$ as a function of *x* and *t* with a $y = 0$, i.e. the probe spot is scanned along the x-direction. A few examples of the profiles at probe delays of -10, 10, 20, 30, 40, and 100 ps, along with the Gaussian fits, are plotted in Fig. 4.2(b). By fitting the profiles at these time delays and several in between, we deduce the squared width as a function of the probe delay, as shown as the symbols in Fig. 4.2(c). A linear expansion of the squared width, as expected from the diffusion model, is clearly observed over the whole time range measured. From a linear fit, we deduce an ambipolar diffusion coefficient of about 170 ± 10 cm^2/s.

In order to study the diffusion coefficient as a function of sample temperature, we use the same procedure and vary the sample temperature in the range 10 to 300 K. The results are summarized by the solid squares in Fig. 4.3. Due to the nonuniformity of the sample, the diffusion coefficient can be different at different sample positions. Therefore, at each temperature, multiple measurements at different sample locations were taken. The plot shows the average value and the error bar is
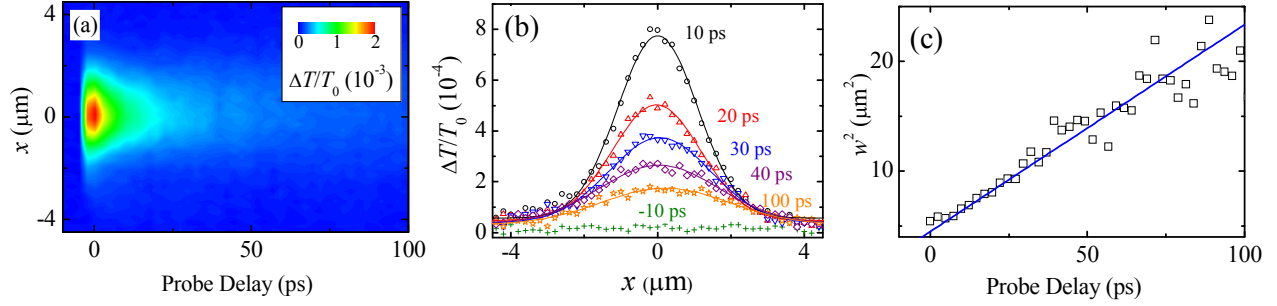
Figure 4.2: (a) Differential transmission for the bulk GaAs sample as a function of probe x position and probe delay. (b) Differential transmission as a function of probe x position for various time delays. (c) Plot of width (FWHM) squared as a function of probe delay with a linear fit. Data from Ruzicka *et al.*[3]

from the variance of the measurements. Clearly, the ambipolar diffusion coefficient decreases monotonically with temperature over the range studied, from about 170 cm^2/s at 10 K to about 20 cm^2/s at room temperature.

These results are reasonably consistent with a previous measurement for a temperature of 60 K (120 cm^2/s).[17] Also, it is interesting to compare these results with previously measured mobilities. The mobilities of electrons and holes in GaAs have been measured by many groups, and the results from high-purity samples are reasonably consistent. Hole mobilities (μ_h) that were measured in high-purity p-type GaAs at sample temperatures of 50, 100, 150, 200, 250, and 300 K are 15, 4.5, 3, 1.5, 0.8, and 0.36 $\times 10^3$ cm^2/Vs.[72,73] Electron mobilities (μ_e) have also been determined by using high-purity n-type samples, and the reported values are 32, 13, 3, 1.8, 1, and 0.75 $\times 10^4$ cm^2/Vs for these same temperatures.[73,74] Since the diffusion coefficients are measured by measuring the change in width over 100 ps, for all of these measurements, the carriers are in thermal equilibrium with the lattice. Hence, from these values, it is straightforward to deduce the diffusion coefficients of electrons and holes D_n and D_h for these temperatures by using the Einstein relation, Eq. (4.5). While these values are all Hall mobilities, here they are treated as drift mobilities for simplicity. From the diffusion coefficients of electrons and holes, the ambipolar diffusion coefficients can then be deduced using Eq. (4.10). The results are plotted as the open circles in Fig. 4.3. Clearly, these results agree very well with these transport measurements.

In summary, the ambipolar diffusion of photoexcited carriers in a bulk GaAs sample was stud-
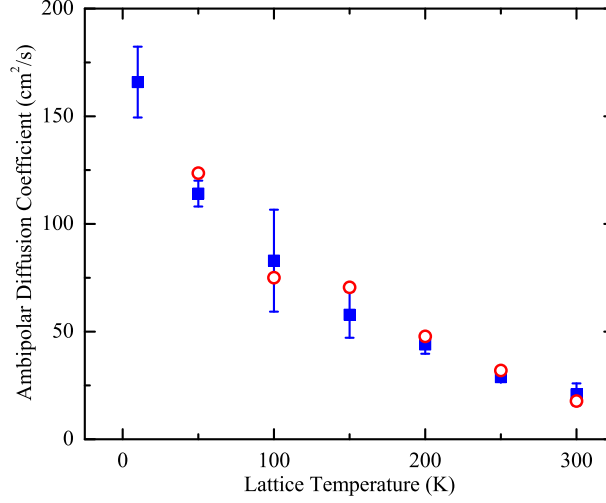
Figure 4.3: Ambipolar diffusion coefficient for bulk GaAs measured as a function of sample (blue squares) with values calculated from measured electron and hole mobilities (red circles). Data from Ruzicka *et al.*[3]

ied by using the temporally and spatially resolved pump-probe technique. The ambipolar diffusion coefficient was observed to decrease from about 170 cm^2/s at 10 K to about 20 cm^2/s at room temperature, which is reasonably consistent with values deduced from the previously measured mobilities by using the Einstein relation. This experiment demonstrates the accuracy of such a technique for measuring the diffusion coefficient.

4.4.3 Other semiconductors

The temporally and spatially resolved pump-probe technique for measuring the diffusion coefficient can be readily extended to a wide variety of semiconductors, as long as pump-probe measurements are possible (i.e. the band gap energy is obtainable) and it can be verified that the differential transmission or differential reflection is proportional to the carrier density. In this section, results on three different semiconductors will be briefly presented: graphene (epitaxial on SiC, reduced graphene oxide and graphene produced by CVD), Si/SiGe quantum wells, and carbon nanotubes. For each material, a study of the diffusive transport of photoexcited carriers is useful, since this provides an intrinsic measurement of the diffusion coefficient, which does not rely on any electrical contacts, which may drastically effect the results. First, a brief description of the sample and

the experimental conditions for each will be presented, followed by a summary of the results for all of the samples.

For graphene, samples produced by three different methods were studied, which are all of great technological relevance: epitaxial graphene, reduced graphene oxide and CVD graphene. The first has great potential to be used in semiconductor industry since it can be produced on large scales with a high degree of repeatability on an insulating substrate,[28] while the second two can be produced with low cost and involve techniques that are already well developed.[75,76] The epitaxial graphene samples are prepared on a Si-terminated 6H-SiC (0001) crystalline wafer surface by solid-state graphitization.[77,78] The reduced graphene oxide samples are the same samples discussed in Sec. 3.4.2. Finally, the CVD graphene samples were grown on copper foils using chemical vapor deposition by methane and subsequently transferred to glass substrates.

The carriers were excited in the reduced graphene oxide and the epitaxial graphene using 750 nm, 100 fs pump pulses, focused to a spot size of 1.6 μm FWHM. The carriers were probed by measuring the differential transmission of an 810 nm, 190 fs probe pulse that was focused to a spot size of 1.2 μm FWHM. Also, for these two samples, the peak fluence of the pump pulse was about 170 μJ/cm^2. For the CVD graphene sample, in order to avoid a secondary component of the signal of unknown origin (possibly due to residue from the fabrication process), the idler of the OPO (1761 nm) is used as a probe instead of the 810 nm Ti:Sa output. The peak pump fluence for this measurement is also around 200 μJ/cm^2. While the probe is different for the CVD graphene measurement, this is not expected to have any effect on the result, since graphene has no band gap.

The Si/SiGe quantum well samples are the same as those discussed in Sec. 3.4.3. Also, the same experimental conditions are used: an 810 nm probe pulse and a 750 nm pump pulse are focused to the sample to a spot size of approximately 2 μm FWHM. The peak pump fluence for this measurement is 110 μJ/cm^2. Finally, the same pump and probe conditions are true for the CNT samples, but a peak pump fluence of 190 μJ/cm^2 is used.

In each case, the same measurements were taken as for the bulk GaAs experiment, which includes data as in Fig. 4.1 and Fig. 4.2. The diffusion coefficients of all of the samples that
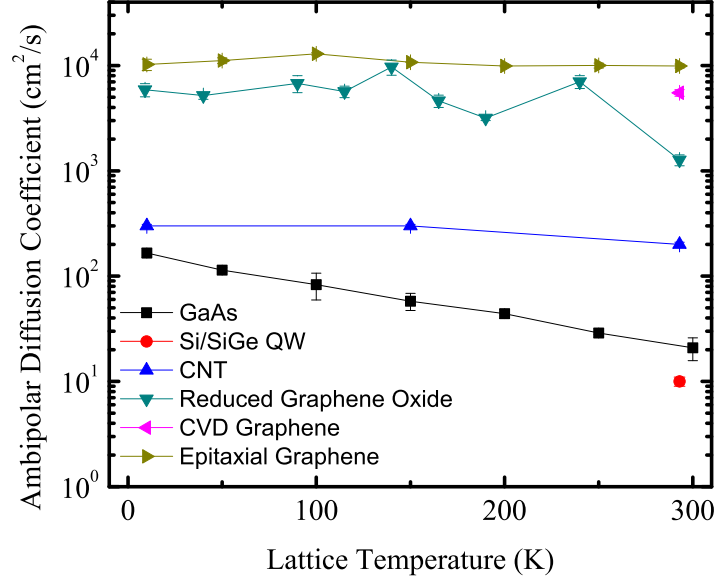
Figure 4.4: Summary of all diffusion coefficients measured at various temperatures. Data from Ruzicka *et al.*[3,4]

were discussed are shown in Fig. 4.4 as a function of lattice temperature (where relevant). We see that, as expected, the graphene samples have the highest diffusion coefficients overall. The epitaxial graphene sample shows slightly higher diffusion coefficient than the CVD graphene and the reduced graphene oxide samples. This is most likely due to larger grain size in the epitaxial sample compared to the other two. Most likely graphene produced by mechanical exfoliation of bulk graphite would exhibit an even higher diffusion coefficient. However, we are not able to obtain a uniform sample that is large enough to study diffusion in with the roughly 2 μm laser spot sizes. One important point to make as well, is that the CVD graphene samples were very nonuniform, and only in a very small area was it possible to obtain a diffusion coefficient measurement. Therefore, since during low temperature measurements it is impossible to visit all sample positions due to restrictions caused by the presence of the cryostat, the CVD graphene diffusion was only studied at room temperature.

The CNT diffusion coefficient then follows the graphene diffusion coefficients and is roughly a factor of ten smaller. The GaAs bulk then shows the next largest diffusion coefficient, and at low temperature its value is comparable to that of the carbon nanotubes. The larger effective mass in the GaAs compared to the graphene and CNTs is the cause of this result. At lower temperatures,

a larger diffusion coefficient in GaAs is due to the fact that the carriers are in thermal equilibrium with the lattice, and so also have a low temperature, in contrast with graphene, where the carriers remain at an elevated temperature, as discussed in Sec. 3.4.2.2. This results in reduced scattering, which leads to a larger diffusion coefficient (and mobility). Finally, the diffusion coefficient for the Si/SiGe quantum well sample is the lowest, which may be due to large scattering between the well and barrier layers.

4.5   Summary

Two quantities that are of great interest for describing transport in semiconductors, diffusion coefficient and mobility, can be studied using spatially and temporally resolved pump-probe techniques. By measuring the differential transmission as a function of both time and space, and observing how the carrier density profile expands over time, the ambipolar diffusion coefficient can be directly measured. If the carrier temperature is known, this can then be directly related to the more frequently discussed quantity, mobility, by the Einstein relation. Results on temperature dependent measurements of the diffusion coefficient in bulk GaAs were presented. The excellent agreement of these with previously measured Hall mobilities demonstrate the accuracy of the pump-probe method for measuring the carrier diffusion coefficient. This experiment has also been extended to other semiconductors such as epitaxial graphene on SiC, reduced graphene oxide, CVD graphene, Si/SiGe quantum wells, and single walled carbon nanotubes. Results on all of these materials were summarized and reasonable diffusion coefficients were obtained.

Chapter 5

Ballistic carrier transport

5.1   Introduction

In the previous chapter, diffusive transport was discussed in detail. However, as device sizes are approaching 20 nm,[10] they will soon be comparable to or even smaller than the mean free path. This means that carriers can move through the device with few or even on collisions. Therefore, this ballistic transport, i.e. transport that does not involve collisions, is also of great interest for electronic applications and in some cases is and will be the only transport of interest.

One goal when developing a method to study any material is to find a technique that is noninvasive and nondestructive. It was predicted many years ago that the interference between one- and two-photon transitions that connect the same initial and final states can lead to the injection of a variety of current types depending on the polarizations of the two. This includes a ballistic pure charge current from parallel linear polarizations,[79] a ballistic pure spin current from perpendicular linear polarizations,[80] and a spin-polarized charge current from same circular polarizations.[80] This quantum interference and control (QUIC) technique for the injection of currents has been well developed, first resulting in the demonstration of optical injection and electrical detection of charge currents in bulk GaAs.[81] This was then followed by several studies where an optical technique involving differential transmission/reflection, which will be discussed in more detail in the following

sections, was used to detect the currents as well. These include all-optical injection and detection of ballistic charge currents in bulk GaAs,[62] GaAs quantum wells,[62] and germanium;[82] pure spin currents in GaAs quantum wells[83,84] and germanium;[85] and spin polarized charge currents in bulk GaAs.[85]

Since no physical electrical contacts are required for the injection of current using this technique, it is a clear noninvasive option for studying currents in semiconductors. This, in combination with the variation on the pump-probe technique that is sensitive to currents, which is referred to as "differential pump probe," allows currents in semiconductors to be studied all-optically, with both optical injection and optical detection. These techniques give access to studies of ballistic currents in semiconductors with very high spatial and temporal resolution.

5.2   Quantum interference and control: Theoretical discussion

As mentioned in the previous section, QUIC techniques can be used to inject a pure charge current, pure spin current, and spin polarized charge current, depending on the relative polarizations of the two pump beams. However, of particular interest here is the discussion of the charge current injection. Therefore only charge current injection will be discussed in detail – the results for spin injection rely on the same interference principle, but the different polarizations of the two pump beams lead to different amounts of spin injection. Also, for simplicity, we consider only the electrons in this discussion.

A charge current is defined as a net flow of electrons. The classic mathematical definition of a charge current that is due to electrons moving with velocity $\mathbf{v}$ is thus

$$\mathbf{J} = -eN\mathbf{v}, \tag{5.1}$$

where e is the electron charge and N is the density of electrons. This is a more fundamental form of the drift current density [Eq. (4.2)], where no collisions are in the picture. As discussed previously, in a semiconductor there is not one velocity, but a distribution of velocities – more specifically a
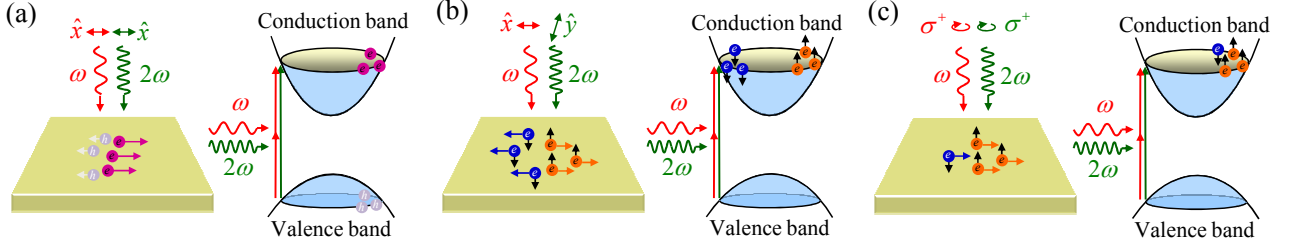
Figure 5.1: QUIC excitation scheme. Two pump pulses are incident on the semiconductor, one of angular frequency ω and the other of angular frequency 2ω. (a) Linear polarizations along the same direction ($\hat{x}$ here, for example) lead to the injection of a pure charge current. (b) Perpendicular linear polarizations lead to the injection of a pure spin current along the direction of the ω polarization. (c) Same circular polarizations lead to the injection of a spin polarized charge current. Schematic from Ruzicka and Zhao.[5]

distribution of carriers with different crystal momenta, $\hbar\mathbf{k}$. If the distribution function in terms of $\mathbf{k}$ is $f(\mathbf{k})$ (i.e. the number of electrons with wave vector $\mathbf{k}$ per unit volume), then the current density in the semiconductor will be

$$\mathbf{J} = -\sum_{\mathbf{k}} e\mathbf{v}(\mathbf{k})f(\mathbf{k}) = -\frac{e\hbar}{m_e^*}\sum_{\mathbf{k}}\mathbf{k}f(\mathbf{k}), \tag{5.2}$$

where m_e^* is the electron effective mass.[86] Therefore, in order for there to be a net current along any particular direction, the distribution function cannot be symmetric with respect to $\mathbf{k}$.

As illustrated in Fig. 5.1(a), this type of distribution can be achieved by using two frequency related laser pulses since their transitions will interfere, leading to a non-symmetric distribution of electrons in $\mathbf{k}$-space. Recall from Chapter 2, that the transition rate for direct interband absorption is proportional to the square of the matrix element connecting the final and initial states of the transition, as given by Fermi's golden rule:

$$R_{i\rightarrow f} \propto |M|^2. \tag{5.3}$$

The interaction of the semiconductor with light, which causes the transition, can be described using

the following perturbation Hamiltonian under the electric dipole approximation:

$$H^1 \simeq \frac{e}{2m_e^*} \mathbf{A} \cdot \mathbf{P} e^{-i\omega t}, \tag{5.4}$$

where $\mathbf{P}$ is the momentum operator and $\mathbf{A}$ is the field amplitude.[87] For a photon of frequency 2ω, with energy $\hbar 2\omega > E_g$, the transition amplitude will then be

$$\langle f| \frac{e}{2m_e^*} \mathbf{A}_{2\omega} \cdot \mathbf{P} |i\rangle = \frac{e}{2m_e^*} \mathbf{A}_{2\omega} \cdot \mathbf{P_k}, \tag{5.5}$$

where f and i represent the final and initial states, respectively, and $\mathbf{P_k}$ is the momentum matrix element, which depends on $\mathbf{k}$. If a photon of frequency ω, with energy $\hbar\omega < E_g < 2\hbar\omega$, two intermediate transitions will occur leading to the excitation of an electron to the same energy state as the 2ω transition. The first transition to the intermediate state will have amplitude

$$\langle int| \frac{e}{2m_e^*} \mathbf{A}_\omega \cdot \mathbf{P} \frac{1}{\hbar\omega} |i\rangle, \tag{5.6}$$

where int represents the intermediate state. Notice also that this amplitude is decreased inversely proportional to the amount of energy it is short of for reaching the conduction band. The transition from the intermediate state to the final state is similar to the interband transition, but instead of the momentum operator, the crystal momentum operator must be used:[37]

$$\langle f| \frac{e}{2m_e^*} \mathbf{A}_\omega \cdot \hbar\mathbf{k} |int\rangle. \tag{5.7}$$

Then, the transition amplitude for the two photon process is

$$\frac{e^2\hbar}{4m_e^{*2}} (\mathbf{A}_\omega \cdot \mathbf{P_k})(\mathbf{A}_\omega \cdot \mathbf{k}) \frac{1}{\hbar\omega}. \tag{5.8}$$

Therefore, when the one- and two-photon transitions occur simultaneously, the transition rate will

be proportional to

$$|\mathbf{A}_{2\omega} \cdot \mathbf{P_k} + (\mathbf{A}_\omega \cdot \mathbf{P_k})(\mathbf{A}_\omega \cdot \mathbf{k})|^2. \tag{5.9}$$

The interference term of the transition rate is the only one of interest, since this contains an odd $\mathbf{k}$ term. Also, recall that we are discussing charge current injection so the polarizations are along the same direction, say $\hat{x}$, so transition rate is finally proportional to

$$|\mathbf{P}_{\mathbf{k},x}|^2 k_x. \tag{5.10}$$

Using Eq. (5.2), the current injection rate along the x-direction will be

$$\frac{dJ_x}{dt} = -\frac{e\hbar}{m_e^*} \sum_{\mathbf{k}} k_x \frac{R_{i \to f}(k_x)}{V} \propto \sum_{\mathbf{k}} |\mathbf{P}_{\mathbf{k},x}|^2 k_x^2. \tag{5.11}$$

Clearly this is is nonzero, since it is an even function of k_x, and therefore a nonzero current density will be injected.

With a more detailed calculation, which has been performed by Bhat and Sipe in general[79] and for GaAs,[88] we can additionally see how the current injection rate relates to the magnitude and phase between the two fields:[62]

$$\frac{dJ_x}{dt} \propto 2|E_\omega|^2 E_{2\omega} \sin(\Delta\phi). \tag{5.12}$$

Here, E_ω and $E_{2\omega}$ are the amplitudes of the electric fields and $\Delta\phi = 2\phi_\omega - \phi_{2\omega}$, where ϕ_ω and $\phi_{2\omega}$ are the phases of the electric fields. In summary, the magnitude of the charge current can be controlled by the relative phase of the two pump fields and the direction of the current can be controlled by the direction of the polarizations of the fields.

Similarly, Bhat and Sipe have performed calculations to show that crossed linear polarizations will inject a pure spin current along the direction of the ω field with a magnitude proportional to $\cos(\Delta\phi)$ [Fig. 5.1(b)], and also that same circularly polarized fields will inject a spin polarized charge current with a direction $\mathbf{m} \equiv \hat{x}\sin(\Delta\phi) \pm \hat{y}\cos(\Delta\phi)$ [Fig. 5.1(c)]. The injection of spin can

be intuitively understood in terms of spin selection rules, which will not be discussed in detail here. Essentially either left (σ^+) or right (σ^-) circular polarization will inject more electrons with one type of spin compared to the other, hence the spin polarized charge current injected from same circular polarizations. The spin polarization of such a population of carriers is defined as

$$\frac{N^\uparrow - N^\downarrow}{N^\uparrow + N^\downarrow} = S/N, \tag{5.13}$$

where $N^\uparrow$ is the density of spin-up electrons, $N^\downarrow$ is the density of spin-down electrons, and $S = N^\uparrow - N_\downarrow$ is defined as the spin density.

The injection of a pure spin current from perpendicular linear polarizations is less intuitive, but relies on the fact that crossed linear polarizations are made up of a combination of left and right circular polarizations:[89]

$$
\begin{aligned}
H &= \tfrac{1}{2}(\sigma^- + \sigma^+) \\
V &= \tfrac{i}{2}(\sigma^- - \sigma^+).
\end{aligned}
\tag{5.14}
$$

A pure spin current is defined as

$$\mathbf{K} = \frac{\hbar}{2} N^\uparrow \mathbf{v}^\uparrow - \frac{\hbar}{2} N^\downarrow \mathbf{v}^\downarrow, \tag{5.15}$$

where $\mathbf{v}^{\uparrow(\downarrow)}$ is the average velocity of the spin-up (-down) electrons. Therefore, in order to have a pure spin current, there must be equal densities of spin up electrons moving at the same velocity, but in the opposite direction as spin down electrons. Since vertically and horizontally polarized light contain different linear combinations of left and right circular components [Eq. (5.14)], spin dependent calculations that are similar to those in Sec. 5.2 show that this leads to the discriminatory injection of one spin system at one k-state and another at the opposite k-state.[80] In other words, this causes the injection of equal densities of spin-up and spin-down electrons with opposite velocities ($\mathbf{v}^\uparrow = -\mathbf{v}^\downarrow$ and $N^\uparrow = N^\downarrow$), so a pure spin current is injected.

5.2.1 Summary

Two frequency related laser pulses can inject currents by the interference between one- and two-photon transitions. The quantum interference of the two transitions causes an imbalance in the distribution of charge or spin in k-space, which leads to a charge current, spin current, or spin polarized charge current. With parallel linear polarizations, a charge current will be injected along the polarization direction, with the injection rate proportional to $\sin(\Delta\phi)$, where $\Delta\phi$ is determined by the phase difference between the two fields. When the polarizations are perpendicular, a pure spin current will be injected along the direction of the ω polarization, with the injection rate proportional to $\cos(\Delta\phi)$. Finally, when the same circular polarizations are used, a spin polarized charge current will be injected, with the direction determined by the relative phase as $\mathbf{m} \equiv \hat{x}\sin(\Delta\phi) \pm \hat{y}\cos(\Delta\phi)$.

5.3 Experimental techniques: Differential pump-probe

5.3.1 Introduction

In order to detect charge and spin currents we again use differential transmission or reflection measurements. However, as discussed in previous chapters, differential transmission and differential reflection give information about the carrier density – they fundamentally cannot directly measure a current density. Therefore, we instead measure the spin or charge accumulation that is caused by the net flow of charge or spin. Experimentally, this essentially amounts to measuring the differential transmission or differential reflection at different positions along the current flow and modulating the *current density* instead of the pump power or carrier density, as we did in the previous two experiments, hence the name differential pump-probe. Finally, by analyzing the density of carriers that have accumulated at various positions, we are able to infer the average distance that charge or spin has traveled, otherwise known as the charge or spin transport length.

5.3.2 Derivative detection scheme

First, we consider a charge current injected using the QUIC technique. A Gaussian spatial profile of carriers will be generated, with an average velocity along a specific direction. For this example we will assume the current is moving along the $\hat{x}$ direction. Since the carriers are all moving along the same direction, after a short time the carrier density profile will have shifted, as shown in Fig. 5.2(a). Since this shift is extremely small (on the order of tens of nanometers), it is not directly observable using the techniques discussed in Chapter 4, since the laser spots are 2 μm FWHM – much larger than the transport length. However, this problem can by solved by instead measuring the difference between the moved and unmoved profiles, which is relatively large even for small movements due to the Gaussian shape of the profile and is directly related to the shift in length. Assuming the current is instantaneously injected at time $t = 0$, since the transport length, d, is much smaller than the width of the profile, w, the difference between the profiles before $[N(t = 0))]$ and after $[N(t > 0)]$ movement is

$$\Delta N = N(t > 0) - N(t = 0) \cong d\frac{\partial N}{\partial x}. \tag{5.16}$$

Since d is so small, ΔN will be derivative-like, i.e. it will approximately equal to the derivative of the Gaussian, as shown in Fig. 5.2(b). Then, using Eq. (5.16), for a Gaussian profile it can be shown that all of the measurable quantities are related to the transport length through

$$d = 0.707\frac{h}{H}w, \tag{5.17}$$

where h is the height of ΔN and H is the height of $N(t = 0)$.[62] Similarly, for spin transport the two spin profiles will separate by a small distance as shown in Fig. 5.2(c). By measuring the height of the derivative-like profile caused by the spin separation as shown in Fig. 5.2(d), it is also possible to deduce the spin separation distance using Eq. (5.17).

In Eq. (5.17), we see that in order to measure the transport length, we must measure the
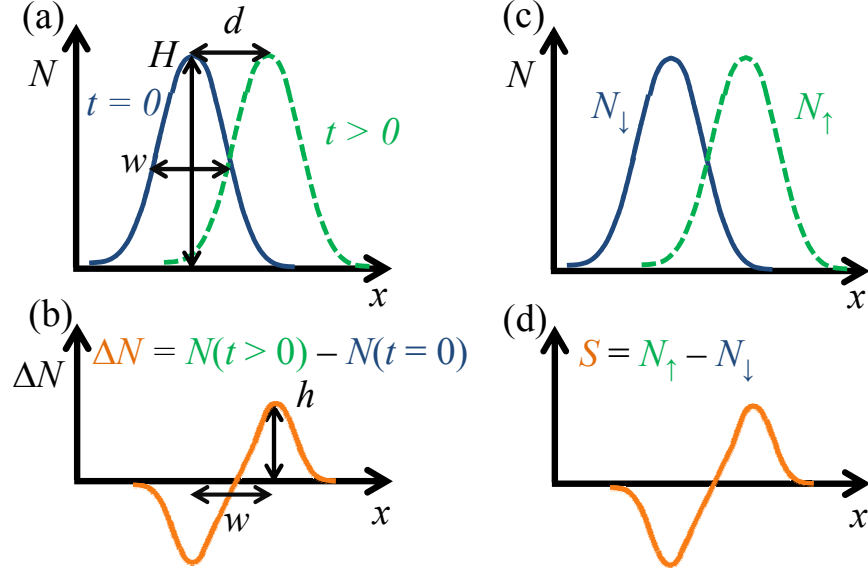
Figure 5.2: Derivative detection scheme to spatially resolve ballistic charge [(a),(b)] and spin [(c),(d)] currents. Panels (a) and (c) show the effects of charge and spin currents on the carrier density and spin density profiles, respectively (the magnitude of d is greatly exaggerated for clarity). Panels (b) and (d) show the resulting charge and spin accumulation, respectively.

height of the spatial profile, H, the width of the spatial profile, w, and the height of the derivative, h. The first two are measured as discussed in Chapter 4, by scanning the probe spot across the pump spot and measuring the differential transmission or reflection at a time close to zero delay, when the signal has reached a peak. The height H is proportional to $\Delta T/T_0$ or $\Delta R/R_0$ and w is obtained by fitting the spatial profile with a Gaussian function. The last quantity, h, is measured using the differential pump-probe scheme: Whereas to measure H we modulate the carrier density by modulating the intensity of the pumps with an optical chopper, to measure h we modulate the current density by modulating the relative phase of the ω and 2ω fields with an electro-optic phase modulator. As discussed in Sec. 5.2, the current density varies sinusoidally with the relative phase between the two fields (sine for charge current and cosine for spin current). Therefore, by modulating the phase of one field between 0 and $\pi/2$ and keeping the phase of the other stable at a fixed value, we can modulate the current density between zero and its maximum value. In the case of charge current, with zero current density the profile is in the same position as it is at time $t = 0$, i.e. carriers are excited but do not move. With maximum current density, at time $t > 0$, the profile

will have moved to a position that depends on the average velocity of the carriers. Therefore, in the same way as $\Delta T/T_0 \propto N$ and $\Delta R/R_0 \propto N$ when modulating the intensity of the pump, $\Delta T/T_0 \propto \Delta N$ and $\Delta R/R_0 \propto \Delta N$ when modulating the current density by modulating the phase. The situation is also the same for spin current density.

In summary, using the relation in Eq. (5.17), the problem of spatial resolution is essentially transformed into a problem of signal to noise ratio, which is a problem that can be solved using balanced lock-in detection, as discussed in Chapter 3. For example, this has been demonstrated in the detection of charge currents injected in bulk germanium using QUIC via the direct interband transition. Although the charge current is expected to be observed as being relatively weak due to the short carrier lifetime as carriers scatter to the lower energy valleys, values of H of 10^{-2} and values of h of 10^{-5} were observed.[82] Recall that H is essentially the peak differential transmission or reflection signal as measured by modulating the pump intensities and h is the peak differential pump-probe signal measured by modulating the current density. Since differential transmission or reflection signals as small as 10^{-7} can be detected using balanced lock-in detection, such a signal can easily be measured.

5.3.3 Experimental configuration: Differential pump-probe

The experimental setup for the QUIC current injection and derivative detection schemes is shown in Fig. 5.3. As in the spatially and temporally resolved pump-probe experiments, the probe delay is controlled by a mechanical stage with a retro-reflecting mirror and the probe position can be controlled by scanning the probe focusing lens. In this case, however, there is the addition of a second pump beam, which is spatially and temporally overlapped with the first on the sample. Since the two frequencies must be related by a factor of two for the quantum interference, this is usually achieved by using a BBO crystal, which allows for the generation of a second harmonic (2ω) of the fundamental pulse (ω).

As discussed in the previous section, in order to measure the spin or charge accumulation, h, the current density must be modulated by modulating the relative phase of the ω and 2ω fields.
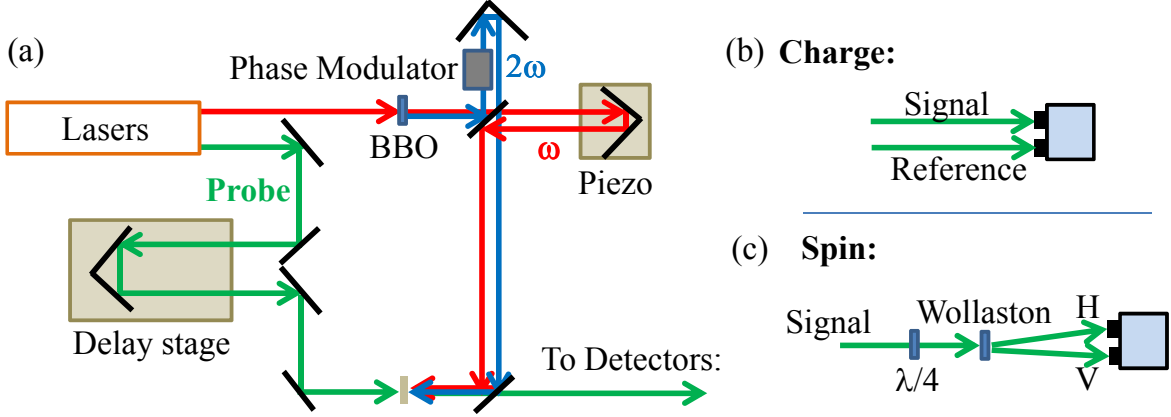
Figure 5.3: (a) Experimental setup for current injection by quantum interference and control. (b) Configuration for derivative detection of charge currents. (c) Configuration for derivative detection of spin currents.

In practice it is not possible to keep the phase of one of the fields constant due to laser drift or small movements in the optics caused by thermal expansion or air. Therefore, in the experiment, the phase of the 2ω beam is modulated with a depth of approximately $\pi/2$ using an electro-optic phase modulator and the phase of the ω beam is scanned by moving a retro-reflecting mirror with a computer-controlled piezoelectric transducer. By referencing the lock-in amplifier to the phase modulation frequency (which is around 2 kHz for these experiments), the output will be proportional to the change in transmission or reflection caused by the phase difference, $\Delta\phi$. The result of such a measurement should be sinusoidal for all three different types of currents, since the current density amplitudes are sinusoids of the phase difference. For example, for pure charge current the current density is proportional to $\sin(\Delta\phi) = \sin(2\phi_\omega - \phi_{2\omega})$. If ϕ_ω is modulated with amplitude Φ_ω and frequency Ω as $\phi_\omega = \Phi_\omega \sin(\Omega t)$, then the output of the lock-in will be proportional to $J(\Phi_\omega)\cos(\phi_{2\omega})$, where $J(\Phi_\omega)$ is the first order Bessel function of the first kind of the modulation amplitude. (See appendix A for further information.)

In order to implement the derivative detection scheme for charge currents [Fig. 5.3 (a) and (b)], we use the detection setup as shown in Fig. 3.2, but with the counter-propagating differential transmission configuration. This is necessary in order to have the ability to scan the probe with respect to the pumps and keep the pumps overlapped with each other in both time and space. In

order to increase the signal to noise ratio, the transmitted probe is sent to one arm of the balanced photoreceiver and a reference is sent to the other.

The implementation for spin currents [Fig. 5.3 (a) and (c)], however, involves a slightly different configuration since we need the ability to detect the spatial profile of each spin system separately. First, the linearly polarized probe pulse is sent through the sample. Since linearly polarized light is composed of equal amounts of left and right circularly polarized light, each circular component of the light essential performs a differential transmission measurement on one particular spin system. Therefore, if the two circular components are separated, each component will contain information about one spin system. This separation is achieved by sending the transmitted probe to a quarter wave plate followed by a Wollaston prism. The quarter wave plate converts each circular component to linear (one becomes vertical and the other becomes horizontal, depending on the orientation of the wave plate with respect to the polarization) and the Wollaston prism separates the vertical and horizontal components and sends them in different directions. By balancing the two arms when a pure linear polarization is incident on the quarter wave plate, the output of the balanced photoreceiver will be proportional to the difference in transmission of the two circular components, and the lock-in voltage will be proportional to the so-called "circular dichroism" $(\Delta T^+ - \Delta T^-)$. This balance also serves the dual purpose of increasing the signal to noise ratio, as in the case of charge detection.

5.3.4 Summary

Although charge and spin currents injected using QUIC only lead to charge transport lengths or spin separations on the order of tens of nanometers, this can be detected using a differential pump-probe scheme. The change in the carrier or spin density profiles can be directly measured using pump-probe techniques by modulating the current density, similar to how carrier or spin density profiles can be measured by modulating the carrier density. This is achieved by modulating the relative phase between ω and 2ω using an electro-optic phase modulator. Since the charge or spin transport distance is so small, the heights and widths of the initial and difference profiles can be

used to deduce the transport distance.

5.4 Results and discussion: Differential pump-probe study of currents injected by QUIC

5.4.1 Subpicosecond AC spin-polarized charge currents

Up to this point only dynamics relating to charge have been discussed, with little mention of spin. However, the control of the spin degree of freedom as well as charge for information transfer (a field known as spintronics), can potentially lead to many applications in industry. As such, the generation, manipulation, and detection of spin currents in semiconductors are the fundamental aims of spintronics.[61,90] Although it is possible to generate pure spin currents that are not accompanied by any charge currents through a spin Hall effect[91–93] or by the optical techniques discussed in the previous section,[83,94] spin currents are carried by charge currents in most cases via spin polarized charge currents.

In the past, spin polarized charge currents have been generated by dragging optically excited spin polarized carriers by an electric field[95,96] or through contact with magnetic materials.[97–99] However, since these currents are DC and, in most cases, steady state, they are of less interest for applications where AC spin currents may be desirable. Optical injection of spin-polarized charge currents has been demonstrated through quantum interference in bulk GaAs[85] and by the spin photogalvanic effect in several structures including GaAs quantum wells QWs,[100–102] InAs QWs,[103] Si/Ge QWs,[104] and AlGaN/ GaN superlattices.[105–108] Although these currents were injected optically, with no external electric fields, in each of these studies currents were not detected by optical techniques, but by measuring the steady-state voltage[85,100–108] caused only by the charge component of the currents. Therefore, the spin polarization of such currents was not measured. Additionally, these steady-state electrical detection techniques were not able to time-resolve the current dynamics, which is of course essential for demonstration of an AC spin-polarized charge

current.

In this experiment, we inject currents using the quantum interference between 1500 nm, 100 fs pulses and 750 nm pulses obtained from the OPO output and second harmonic generation of this output using a BBO crystal, respectively. The 2ω pulse (750 nm) is tightly focused to a spot size of 1.8 μm FWHM with a peak fluence of 5 μJ/cm^2, and therefore excites a peak areal density of 2×10^{12}/cm^2. The optical power and spot size of the ω pulse (1500 nm) is set to produce the same peak carrier density via two-photon absorption. The two pulses are both set to right-circular polarization with purities better than 97% by using a series of quarter wave plates and polarizers and are sent through the interferometer as shown in Fig. 5.3 for phase control. As discussed in Sec. 5.2, we inject the spin polarized charge current along the $\hat{x}$ direction by choosing $\Delta\phi = \pi/2$. The experiment is performed on the same 400-nm-thick bulk GaAs sample as the diffusion experiment, at room temperature. Since both heavy-hole and light-hole transitions are excited in this configuration, the spin polarization of electrons is expected to be about 0.5, according to the well established spin selection rules.[109] However, certain theoretical calculations have predicted slightly larger spin polarizations of the currents of 0.57 in bulk structures.[80]

The electron density is measured by focusing a linearly polarized 100 fs probe pulse obtained from the Ti:sapphire laser on the sample to a spot size of 1.8 μm FWHM. The differential transmission is measured with a reference to increase the signal to noise ratio. The probe pulse is tuned to a central wavelength of 820 nm, corresponding to an excess energy of 90 meV. We again measure $\Delta T/T_0$ as a function of pump pulse fluence to verify that, for the carrier densities used in this study, $\Delta T/T_0 \propto N$. The spin density is simultaneously measured by sending a portion of the transmitted probe pulse to a configuration as shown in Fig. 5.3(c). The measured circular dichroism is related to spin density by using a calibration process based on the well-established fact that interband transition induced by a circularly polarized pump pulse produces a spin polarization $S/N = 0.5$.[110]

Figure 5.4(a)-(d) summarizes measurements performed with a fixed probe delay of 0.3 ps. (Data from Ruzicka et al.[6]) The spatial profiles of N [(a) squares], ΔN [(a) circles], S [(c) squares] and ΔS [(c) circles] are measured by scanning the probe spot along $\hat{x}$ with $\Delta\phi = \pi/2$. Here, ΔS
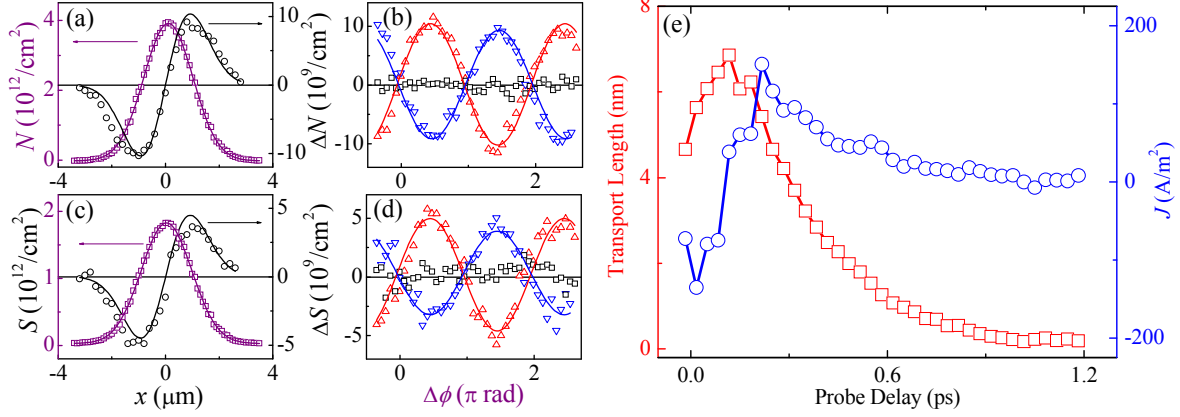
Figure 5.4: Profiles of electron density squares in (a), electron accumulation circles in (a), spin density squares in (c) and spin accumulation circles in (c) measured with a probe delay of 0.3 ps and $\Delta\phi = \pi/2$ at room temperature. Panel (b) [(d)] shows electron spin accumulation measured at a probe position of $x = +1.0$ μm (up triangles), -1.0 μm (down triangles) and zero (squares), respectively, when $\Delta\phi$ is varied. (e) Temporal evolutions of the transport length (squares) and current density (circles) at room temperature obtained by repeating the measurements summarized in (a) and (b) with different probe delays. Data from Ruzicka *et al.*[6]

is defined similarly to ΔN as $\Delta S = S(t > 0) - S(t = 0)$. The Gaussian profiles of N and S are consistent with the shape and size of the laser spots. The derivative-like ΔN profile shows that electrons accumulate and deplete along the $\hat{x}$ direction indicating that the electron density profile has moved along $+\hat{x}$. From these profiles, we deduce a transport length of $d = 3.8$ nm by using Eq. (5.17). Spin transport is also evident from the derivative-like ΔS profile. Therefore, the photogenerated currents are indeed spin polarized, since for a pure charge current, the accumulated electrons should be spin unpolarized and ΔS should be zero. The spin polarization of the accumulated electrons due to the current, $\Delta S/\Delta N \approx 0.6$, which indicates that the spin polarization of the current is also about 0.6.

Panels (b) and (d) of Fig. 5.4 demonstrate the phase control of the current injection. The up triangles in (b) show ΔN as a function of $\Delta\phi$ measured at a fixed position of $x = +1.7$ μm. The observed sinusoidal variation is consistent with the sinusoidal dependence of the injected average velocity along the $\hat{x}$ direction. The sinusoidal dependence is also observed at the other side of the profile with a fixed $x = -1.7$ μm (down triangles). The two curves are exactly out of phase by π. Furthermore, a measurement performed at $x = 0$ yields no signal above the noise level (squares).

All of these are consistent with the derivative-like profile of ΔN shown in panel (a). Similar results are also obtained for the spin accumulation ΔS, as shown in panel (d).

Additionally, these all-optical detection techniques provide a high enough temporal resolution to time resolve the current dynamics. The procedure summarized in panels (a) and (b) is used to measure the transport length as a function of probe delay. The results are shown as the squares in Fig. 5.4(e) and can be explained as follows: By using quantum interference, spin polarized electrons are injected with an average velocity along $+\hat{x}$. Therefore, upon injection, the electrons move with a velocity in the direction of $+\hat{x}$. The same quantum interference process also injects holes with opposite momentum, according to crystal momentum conservation. Therefore, the holes are simultaneously moving along $-\hat{x}$. Since the holes have a larger effective mass as compared to the electrons, they move with a smaller average velocity. Once the electrons and holes separate, a space-charge field develops, i.e. a coulomb force between the negatively charged electrons and positively charged holes, slowing down and eventually stopping the motions of electrons and holes. Once the velocity reaches zero and the electrons and holes reach maximum separation, the space-charge field becomes a driving force to pull the electrons and holes back to a common location. Since during the whole process, strong phonon and intercarrier scattering exists, this oscillator-like system is strongly damped. Therefore multiple oscillations are not observed. The dynamics exist for just over 1 ps. Apparently, although the holes only make weak contributions to the differential transmission of the probe, they do play important roles in determining the current dynamics.

The squares in Fig. 5.4(e) show the temporal evolution of the average position of electrons. Therefore, a time derivative of this curve gives the temporal evolution of the average velocity and thus the charge current density, as shown with the circles in Fig. 5.4. From this the AC and subpicosecond nature of the current is obvious, as one would infer from the temporal evolution of the current density. The current starts with the highest and negative density due to the instantaneous optical injection. It decays with time, then changes to positive, and eventually decays to zero within about 1 ps. Due to the strong damping, the AC current is single cycle.

Although Fig. 5.4(e) only shows the charge component of the current, the spin component is

simultaneously monitored in the experiment and a similar temporal behavior is observed. When taking the ratio, no temporal variation of the $\Delta S/\Delta N$ is observed over the 1.2 ps shown. This is consistent with the long spin-relaxation time of about 100 ps that is measured separately by monitoring the decay of S/N on longer time scales. By averaging the data, we obtain the spin polarization of the accumulated electrons, and thus the spin polarization of the current, to be 0.6 ± 0.1. This value is reasonably consistent with earlier theoretical prediction of 0.57.[80,110]

In summary, a spin polarized charge current was injected using QUIC from two same-circularly polarized pump pulses. The charge and spin transport lengths were deduced optically, using the differential pump-probe technique. The charge current was found to have a spin polarization of 0.6 ± 0.1. This spin-polarized charge current displayed a strongly damped oscillatory behavior caused by the space-charge field between the separated electrons and holes and decayed to zero within about 1 ps.

5.4.2   Efficiency of current injection by quantum interference

When using QUIC techniques to inject and control currents, it is of great importance to know the relative optical powers that are necessary in order for the two pump pulses to most efficiently inject a current. Since the average velocity that is injected as a result of the quantum interference depends on the relative strength of the two transition pathways driven by the two laser pulses, the overall power dependence of injected current density can be complicated. As such, theoretical calculations using different approaches have yielded qualitatively different results.[80,110–112] However, there has been no report on an experimental study of this issue.

Such a study cannot be performed on a charge current, since the space-charge field caused by the electron and hole separation can be complex, as discussed in the previous section. Therefore the maximum charge transport distance cannot be directly related to the *injected* current density. This leaves the only possibility for this study up to spin current injection, since there is no such mechanism that will cause the spin current to reverse. Additionally, it has been predicted that charge current injection has the same power dependence as spin current injection.[80,110] However,

although the spin accumulation can be readily related to a spin separation, these quantities are determined by not only the initial injected current density, but also the relaxation process of the current. The latter is influenced by carrier-carrier scattering, and therefore depends on the carrier density and lattice temperature. Hence, the power dependence of spin current injection cannot be obtained by simply measuring the power dependence of the spin separation – it is required that the total carrier density (i.e. the sum of the density of carriers injected by the two- and one-photon processes) and the lattice temperature remain constant. Only by doing this can the power dependence of the injected average velocity can be obtained, which is the goal of this experiment. Therefore, while we are not able to measure the injected average velocity directly, we can tell when the injected average velocity is largest, by looking at the spin separation.

This experiment is performed on both bulk and quantum-well GaAs samples, at room temperature and 80 K, respectively. The quantum-well sample is composed of ten periods of 14-nm GaAs layers sandwiched by 14-nm AlGaAs barriers. The same pump pulses are used as in the previous experiment to inject the current, but in this case the ω pulse is linearly polarized along the $\hat{x}$ direction and the 2ω pulse is linearly polarized along the perpendicular $\hat{y}$ direction. The 2ω pulse is focused to a spot size $w_0 = 1.4\ \mu$m FWHM. The ω pulse is focused by the same objective lens to a nominal spot size of $\sqrt{2}w_0$. This is achieved by expanding the beam to $\sqrt{2}$ times bigger than the 2ω beam, keeping in consideration that the spot size is proportional to the wavelength and inversely proportional to the beam size. Since the carrier density profile excited by the nonlinear two-photon absorption is $\sqrt{2}$ times narrower than the laser spot, the carrier profiles excited by the two pulses thus have the same width w_0. This is necessary since it ensures that the ratio of the carrier densities excited by each pump (i.e. $N_\omega/N_{2\omega}$, where N_ω and $N_{2\omega}$ is the density of carriers excited by the two- and one-photon transitions, respectively) is uniform across the whole profile.

The carriers are probed with a linearly polarized, 200 fs probe pulse with a central wavelength of 850 nm that is obtained by second-harmonic generation of the idler output of the OPO. It is focused to the sample to a spot size of about 1.4 μm. The same differential pump-probe techniques with the circular dichroism measurement, as discussed in the preceding sections, are used
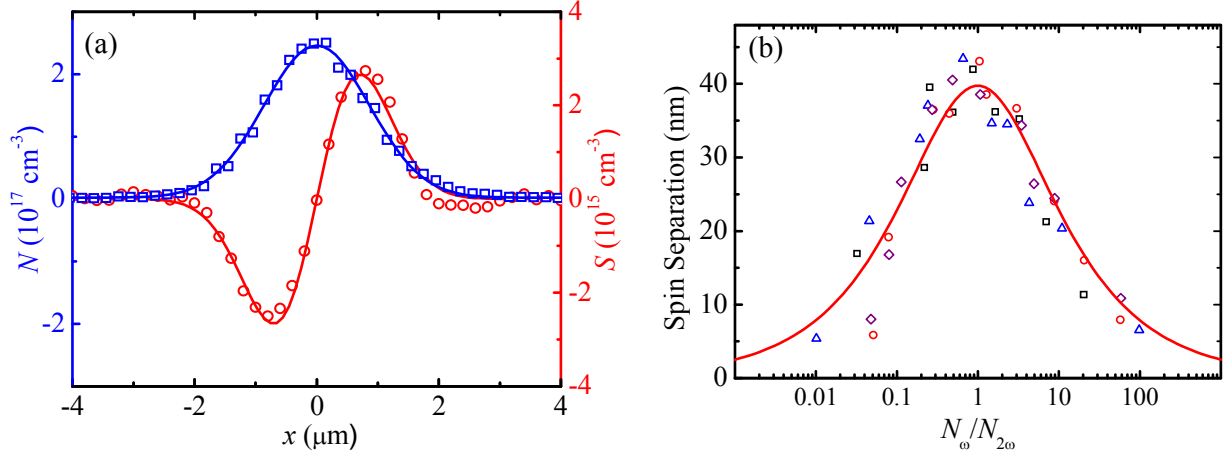
Figure 5.5: (a) Spatial profiles of the total electron density $N = N^\uparrow + N^\downarrow$ (squares, left axis) injected in the GaAs bulk sample at room temperature and the spin density $S = N^\uparrow - N^\downarrow$ (circles, right axis) resulting from spin transport. (b) Spin separation measured as a function of $N_\omega/N_{2\omega}$ by using the procedure summarized in (a). The squares, circles, and triangles show data measured from the bulk sample at room temperature, with a total electron density at the center of the profile of 1.4, 2.5, and 5.5×10^{17} /cm^3, respectively. The diamonds represent data measured from a quantum-well sample at 80 K, with a total electron density of 1.0×10^{17} /cm^3. The data sets shown as squares, triangles, and diamonds are scaled by multiplying factors of 1.30, 1.42, and 0.28, respectively. Data from Ruzicka and Zhao.[7]

to measure the spin separation, i.e. the separation of the spin-up and spin-down carrier density profiles.

In each measurement, the probe delay is fixed so that the probe pulse arrives at the sample 3 ps after the pump pulse. This probe delay is chosen for the following reasons: First, this time is long enough for the spin-up and spin-down systems to reach their maximum separation. Second, this probe delay time is longer than the spin-relaxation time of holes, which has been reported to be much shorter than 1 ps in bulk GaAs.[113] Therefore, the spin current that is measured is only that carried by electrons, since the hole spin current will have relaxed. Finally, this delay time is much shorter than the spin-relaxation time and lifetime of electrons, which are both known to be longer than 100 ps in GaAs. Therefore, the spin density caused by the current does not decay significantly.[84]

Fig. 5.5(a) shows an example of the profiles of electron and spin densities measured by scanning the probe spot along the $\hat{x}$ direction for the bulk sample at room temperature. (Data from

from Ruzicka and Zhao.[7]) In this measurement, the energy fluences of the two pump pulses are adjusted to produce electron densities of $N_\omega = N_{2\omega} = 1.25 \times 10^{17}$ /cm^3 at the center of the profile. As in Fig. 5.4(c), the Gaussian profile of the electron density (squares), N, is consistent with the size and shape of the laser spots. The spin-density profile, S, at the probe delay of 3 ps is shown as the circles. The solid line is a fit of a Gaussian derivative function. From these profiles, we deduce that the spin has separated a distance of 44 nm after 3 ps.

This procedure for measuring the spin separation is repeated with various combinations of N_ω and $N_{2\omega}$, by adjusting the energy fluences of the two pump pulses, but keeping the total electron density constant. This is achieved by keeping the peak of the differential transmission profile (N) the same. The spin separations deduced from these measurements are plotted as a function $N_\omega / N_{2\omega}$ as the circles in Fig. 5.5(b). The maximum spin separation occurs only when $N_\omega = N_{2\omega}$. This set of measurements is then repeated with other different total electron densities of 1.4 and 5.5×10^{17} /cm^3. Similar results are obtained in both sets of measurements, as shown as the squares and triangles in Fig. 5.5(b), respectively.

In order to gain more confidence that the spin separation we measured is indeed proportional to the average velocity and is not influenced by the relaxation of the current, the same measurement is performed on a GaAs quantum well sample cooled to 80 K, since at this temperature the phonon scattering should be suppressed. The total electron density for this measurement is fixed at 1.0×10^{17} /cm^3. As shown as the diamonds in Fig. 5.5(b), the results are similar.

Clearly, for all of the measurements, the maximum spin separation occurs when the carrier densities injected by the two- and one-photon absorption processes are equal. This, as well as the shape of the data, can be understood intuitively in terms of the interference of two classical waves. For example, when two optical beams with the same wavelength with intensities I_1 and I_2 interfere, the efficiency of the interference can be described by the contrast of the resulting interference pattern, $A = (I_{MAX} - I_{MIN})/(I_{MAX} + I_{MIN})$, where I_{MAX} and I_{MIN} are the maximum and minimum intensities seen in the interference pattern. It is well known that the most effective

interference ($I_{MIN} = 0$) occurs when $I_1 = I_2$, and that[114]

$$A = \frac{2\sqrt{I_1 I_2}}{I_1 + I_2}.$$ (5.18)

Interestingly, this same form is expected for the velocity of carriers injected by quantum interference according to calculations based on Fermi's golden rule:[80,110]

$$v = v_0 \frac{2\sqrt{N_\omega N_{2\omega}}}{N_\omega + N_{2\omega}},$$ (5.19)

where v_0 is the maximum average velocity. The solid line in Fig. 5.5(b) is from a fit of the data with Eq. (5.19), allowing a constant multiplying factor as the only adjustable parameter. As shown in the figure, this theory agrees reasonably well with the data and the important result that the most efficient interference occurs when the generated carrier densities are equal is demonstrated.

In summary, the dependence of current injection by quantum interference on the carrier density injected by the one- and two-photon absorption pathways was studied by measuring the power dependence of spin separation caused by a pure spin current. The most efficient current injection, corresponding to the largest injected initial average velocity, occurs when the carrier densities injected by the two pathways are equal. The dependence of the injection on carrier density is well described by calculations based on Fermi's golden rule, which leads to a classical wave interference-like relationship.

5.5   Summary

Ballistic currents can be injected into semiconductors optically using quantum interference of two frequency-related laser pulses. By controlling the polarizations and relative phase of the two pulses, the type and magnitude/direction of the current can be controlled. Two pulses with the same linear polarization will inject a pure charge current, two pulses with perpendicular linear polarizations will inject a pure spin current, and two pulses with the same circular polarization will

inject a spin-polarized charge current. These currents can all be detected optically as well, using differential pump-probe techniques.

Results on AC spin-polarized charge current pulses as well as the efficiency of current injection by quantum interference and control were presented. First, all-optical generation and detection of subpicosecond AC spin-current pulses was demonstrated in GaAs bulk at room temperature. The currents and their spin polarization are detected by spatially and temporally resolving nanoscale motion of electrons using high-resolution differential pump-probe technique. The spin polarization of the currents is measured to be 0.6 ± 0.1 with a peak current density on the order of 10^2 A/m^2. Finally, the efficiency of current injection using quantum interference and control was investigated using all-optical measurements of pure spin currents. The interference follows a classical interference pattern, as the most efficient injection occurs when the carrier density injected by each pump laser pulse is equal.

Chapter 6

Direct optical detection of charge currents

6.1 Introduction

The previous two chapters have focused on carrier transport in semiconductors. The spatially and temporally resolved pump-probe technique provides a real time method to observe and quantify diffusive transport of carriers, while the quantum interference and control technique in combination with differential pump-probe measurements provide a way to study ballistic transport of carriers. While both techniques provide valuable information about their respective transport processes, the technique for studying ballistic transport has a clear disadvantage since it requires an *indirect* measurement – the current density is not measured directly, but rather the transport distance. For studies of diffusion, since it is by definition a process that involves an average motion of a distribution of carriers, it makes sense to measure the carrier system, observe its properties at a later time, and deduce a diffusion coefficient. For studies of ballistic transport on the other hand, it makes much more sense to have a technique that directly senses the carrier velocity or current density.

Additionally, as discussed throughout the dissertation, it is useful to have a measurement technique that is noninvasive and nondestructive. Therefore, an optical technique that can be used to directly measure ballistic transport would be ideal. It was predicted previously that both a pure

spin current[115] and a pure charge current[86] cause a change in the second order susceptibility [$\chi^{(2)}$] in semiconductors. The change in $\chi^{(2)}$ is directly proportional to the spin or charge current density. Therefore, if a spin or charge current is present in a semiconductor, a probe laser pulse of frequency ω that is incident at the same location as the current will lead to the generation of light with frequency 2ω. The intensity of this second harmonic (SH) light can then be related to the current induced $\chi^{(2)}$, thus providing a method for direct detection of ballistic currents. This has recently been demonstrated for pure spin current,[63] and the demonstration for pure charge current will be discussed here.

6.2 Optical effect of charge currents: Theoretical discussion

6.2.1 Second order susceptibility

Classically, when an electric field is incident on a material, its response is determined mainly by the polarization, **P**, which is defined as the net dipole moment per unit volume.[116] While for small electric fields the polarization is proportional to the electric field strength, for large fields and in general the relationship is nonlinear. Hence for an isotropic material we can write the polarization as:[37]

$$P = \varepsilon_0 \chi^{(1)} E + \varepsilon_0 \chi^{(2)} E^2 + \varepsilon_0 \chi^{(3)} E^3 + \cdots, \tag{6.1}$$

where $\chi^{(n)}$ is the n$^{\text{th}}$-order susceptibility and E is the magnitude of the electric field. Of particular interest for this discussion is the second order term,

$$P^{(2)} = \varepsilon_0 \chi^{(2)} E^2, \tag{6.2}$$

since, as will be discussed in more detail in the following section, the $\chi^{(2)}$ is the quantity related to the current density.

When a laser pulse is incident on a material with a nonzero $\chi^{(2)}$, a polarization will be created as according to Eq. (6.2). With an electric field of frequency ω given by Eq. (2.1) at a fixed

position, say $\mathbf{r} = 0$:

$$E(t) = E_0 e^{-i\omega t} + \text{c.c.}, \tag{6.3}$$

this polarization will be[117]

$$P^{(2)} = 2\varepsilon_0 \chi^{(2)} E_0 E_0^* + \varepsilon_0 (\chi^{(2)} E_0^2 e^{-i2\omega t} + \text{c.c.}). \tag{6.4}$$

In other words, the electric field produces a time varying polarization at the SH frequency (2ω) of the electric field, which then emits radiation at this frequency. This process is known as second harmonic generation (SHG). The amplitude of the SH field and its relation to $\chi^{(2)}$ depends on the material being used and can be derived by solving coupled wave equations. However, since for the situations discussed here the SH field is much weaker the fundamental, the SH field is proportional to the square of the fundamental field:[117]

$$E_{2\omega} \propto \chi^{(2)} E_\omega^2. \tag{6.5}$$

6.2.2 Current-induced second order susceptibility

The current induced second order susceptibility is closely related to the quantum interference process described in Chapter 5, as illustrated in Fig. 6.1. In this case we consider a semiconductor with a nonzero current density already present, such that the k-space distribution is not symmetric along a certain direction, say $\hat{x}$, and therefore

$$J_x = -\frac{e\hbar}{m_e^*} \sum_{k_x} k_x f(k_x) \tag{6.6}$$

is not zero. If a photon with frequency ω is incident on the semiconductor and $2\hbar\omega < E_g$, i.e. twice the photon energy is less than the band gap energy, a two-photon virtual upward transition can occur, but due to energy conservation, since this is not enough energy to excite an electron from the valence band to the conduction band, it must be followed by a downward transition

78
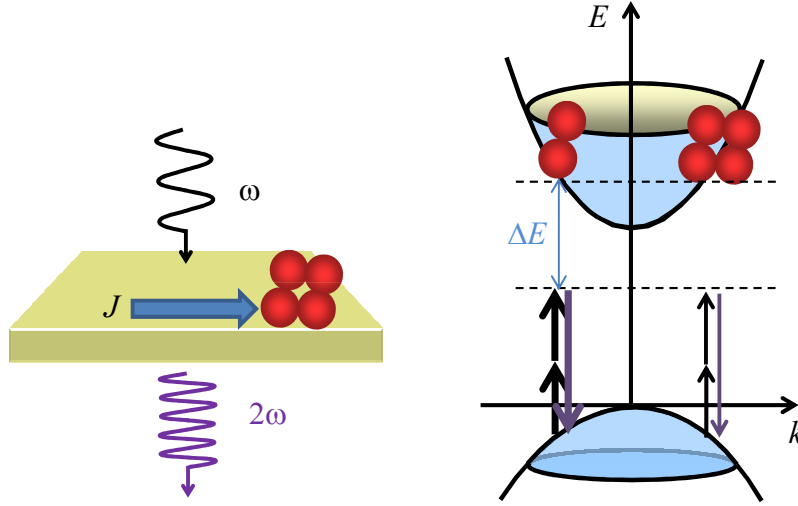
Figure 6.1: Schematic of current-induced second harmonic generation.

accompanied by the emission of photon of frequency 2ω. The amplitude for the virtual upward transition is similar to the amplitude for the two-photon transition [Eq. (5.6)], but it is decreased further by the amount of energy that the overall virtual transition is short of reaching the conduction band:

$$\frac{e^2\hbar}{4m_e^{*2}}(\mathbf{A}_\omega \cdot \mathbf{P_k})(\mathbf{A}_\omega \cdot \mathbf{k})\frac{1}{\hbar\omega\Delta E}. \tag{6.7}$$

Here $\Delta E = E_{cv} - 2\hbar\omega$ is this amount of energy that the transition is short from reaching the conduction band, and is known as the "average detuning." The downward 2ω transition on the other hand, has an amplitude proportional to

$$\frac{e}{m^*}\mathbf{P_k} \cdot \mathbf{A}_{2\omega}, \tag{6.8}$$

since this transition leads back into an actual state in the valence band.

The two transitions cannot exist without each other, so the transition rate is given by the "interference" term only and is proportional to, considering only the $\hat{x}$ direction,

$$|P_{\mathbf{k},x}|^2 \frac{k_x}{\hbar\omega\Delta E}A_\omega^2 A_{2\omega}, \tag{6.9}$$

79

while the total transition rate is found by summing over k_x. Clearly, this will sum to zero, since it is an odd function of k_x. However, this transition rate will be modified by the density of electrons at each k-state. If $f(k_x)$ is nonzero, then there will be $\rho(k_x) - f(k_x)$ fewer states available per unit volume, where $\rho(k_x)$ is the number of total states available per unit volume with wave vector k_x. Hence, the transition rate will be decreased by a factor $(1 - f(k_x)/\rho(k_x))$ and the total transition rate will then be proportional to

$$\sum_{k_x} |P_{\mathbf{k},x}|^2 \frac{k_x}{\hbar\omega\Delta E} A_\omega^2 A_{2\omega} (1 - \frac{f(k_x)}{\rho(k_x)}). \tag{6.10}$$

The term that is odd in k_x sums to zero, so the total transition rate will finally be proportional to

$$\sum_{k_x} \frac{|P_{\mathbf{k},x}|^2}{\rho(k_x)} \frac{k_x}{\hbar\omega\Delta E} A_\omega^2 A_{2\omega} f(k_x). \tag{6.11}$$

Now, by performing this summation it can be shown that the result is a quantity proportional to the current density:[86]

$$\sum_{k_x} \frac{|P_{\mathbf{k},x}|^2}{\rho(k_x)} k_x f(k_x) \propto J_x. \tag{6.12}$$

This can be understood intuitively in terms of the factors $|P_{\mathbf{k},x}|^2/\rho(k_x)$ serving as weights on the contributions of the current at each k-state ($k_x f(k_x)$) to the overall transition rate, which leads to a transition rate proportional to the total current density.

This leaves the transition rate proportional to

$$\frac{A_\omega^2 A_{2\omega}}{\hbar\omega\Delta E} J_x. \tag{6.13}$$

Now, clearly this transition physically corresponds to the development of a second order polarization in the material, $P^{(2)}$. Therefore, by comparing Eq. (6.13) with Eq. (6.4), the second order susceptibility induced by this current is

$$\chi_J^{(2)} \propto \frac{J_x}{\omega^2 \Delta E}. \tag{6.14}$$

Hence the $\chi_J^{(2)}$ is proportional to the current density and inversely proportional to the average detuning energy of the virtual two-photon transition and the square of the probe photon frequency. The proportionality constant depends on the matrix elements $P_{\mathbf{k},x}$, which must be calculated for the semiconductors under consideration

6.3   Experimental techniques: Coherent detection of current induced second harmonic generation

6.3.1   Introduction

In order to study currents by the SHG technique, the currents must first be injected, which can be achieved by a wide variety of methods. To study ballistic currents, the best method is to inject them optically, using the QUIC technique discussed in Chapter 5. In order to study a steady state current on the other hand, a semiconductor with a pair of electrodes can be used. In either case, the signal to noise ratio can be greatly improved by using lock-in detection techniques through current density modulation. In the case of QUIC currents the current density is modulated by modulating the phase difference between the two pulses ($\Delta\phi$), while in the case of electrically injected currents the current density is modulated by modulating the applied voltage with a function generator.

However, even with lock-in detection techniques, the SH that is induced by a charge current may still be too weak to be measured directly. Therefore, the signal must be amplified further in order to be measured. In some semiconductors, such as GaAs,[63] an intrinsic SH is already present due to an already nonzero $\chi^{(2)}$. This provides a very convenient method of amplification, since the intrinsic SH will travel in the same direction as the current generated SH and have close to the same phase. In other cases, however, no intrinsic SH is present, and so an externally generated SH must be used.
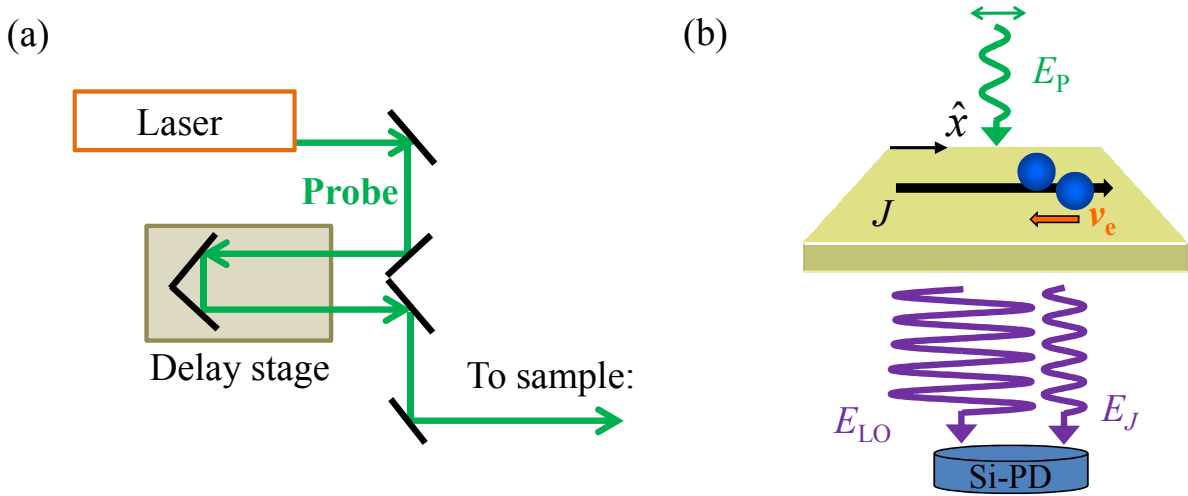
Figure 6.2: Experimental setup for homodyne detection of current induced second harmonic generation using surface second harmonic for amplification. (a) Probe beam configuration. (b) Homodyne detection scheme.

6.3.2 Experimental configuration: Homodyne detection

In order to amplify the weak SH signal induced by the current we use a homodyne detection scheme by a vectorial addition with a local oscillator.[118] Since the experiments discussed here were performed on GaAs samples, which already have a nonzero $\chi^{(2)}$ present at the surface due to symmetry breaking,[117] the local oscillator is actually the SH generated at the surface of the GaAs sample. This local oscillator has the same frequency and ideally the same phase, but a much larger amplitude. Similar results hold for the amplification of the current induced SH by an externally generated SH field, which will not be discussed here.

The experimental configuration is shown in Fig. 6.2. The current is injected in the sample by either the QUIC technique or by electrical methods (not shown). The probe beam is sent through the delay stage for the ability to time resolve current dynamics and is then sent to the sample as shown in Fig. 6.2(a). Then, the probe beam with electric field E_P, polarized along the same direction as the current is incident on the sample. A field at the SH frequency (E_{LO}) will be generated at the surface of the sample (in the case of GaAs, for example). If a current is present along the same direction as the polarization of the probe, an additional, but very small, SH field will be generated as well (E_J). Both fields are sent along the same direction to a silicon photodiode.

The total optical intensity of the SH field will then be

$$I = (c\varepsilon_0/2)(E_{\text{LO}} + E_J)^2. \tag{6.15}$$

Hence, this total intensity contains two main components:

$$I = I_{\text{LO}} + \Delta I, \tag{6.16}$$

where

$$I_{\text{LO}} = (c\varepsilon_0/2)E_{\text{LO}}^2 \tag{6.17}$$

is the intensity of of the local oscillator and

$$\Delta I = (c\varepsilon_0/2)(2E_{\text{LO}}E_J + E_J^2) \tag{6.18}$$

is the change of the total intensity caused by the current-induced SH field.

In general and for the experiments discussed here, $E_J \ll E_{\text{LO}}$. Therefore, we arrive at the simple relation

$$\Delta I \approx c\varepsilon_0 E_{\text{LO}}E_J. \tag{6.19}$$

Additionally, the current density is modulated using the methods discussed in Chapter 5 if the current is injected using QUIC or with a function generator if the current is injected electrically. Similar to the lock-in techniques discussed in the preceding chapters, if the output of the silicon photodiode is sent to a lock-in amplifier referenced to this modulation frequency, the voltage displayed by the lock-in will be proportional to the change in SH intensity caused by the current, ΔI. Hence, under this modulation and detection scheme, the lock-in voltage is proportional to the current induced SH field, E_J. Furthermore, since $E_J \propto \chi_J^{(2)}$ as discussed in Sec. 6.2.1, this voltage is proportional to $\chi_J^{(2)}$.

It is also important to note that since the silicon photodiode produces a voltage output that is

more easily related to the incident optical power, P, the measurements are reported in terms of this instead of the intensity. Hence instead of ΔI, we report ΔP, i.e. the change in optical power of the SH caused by the current. However, for a pulsed laser the two can be easily related as long as the repetition rate, f_{rep}, pulse duration, τ_{pulse}, and width of the laser spot ,w, are known, using:

$$I \approx \frac{P}{f_{rep}} \frac{1}{\tau_{pulse}} \frac{1}{\pi w^2}. \tag{6.20}$$

6.4 Results and discussion: Second harmonic generation by charge currents in GaAs

6.4.1 Electrical injection of a charge current

As stated previously, we can use a current generated in any way to demonstrate this effect. However, for demonstration purposes, it is best to first inject the currents electrically using a pair of electrodes as opposed to optically using the QUIC technique. This way it is clear that the $\chi^{(2)}$ is not being caused by the presence of two laser pulses, but is indeed due to the current, which in this configuration is generated in the simplest possible way. After this, we can use the QUIC technique to inject and study a ballistic charge current.

For the demonstration with electrical injection of current, we use a metal-semiconductor-metal device that was fabricated by depositing a pair of Au electrodes on a GaAs wafer of 0.5-mm thick, as shown schematically in Fig. 6.3(a). The electrodes are separated by a distance of about 14 μm and are approximately 1 by 2 mm in size. The wafer is n-type doped with a concentration of 10^{18} /cm^3 and its room-temperature resistivity is 2.3×10^{-5} $\Omega \cdot m$. Therefore, a 5-V voltage across the electrodes drives a direct current with a density of approximately 10^6 A/cm^2.

In order to observe the SH induced by this current, we use a 0.5-nJ, 170-fs, and 1800-nm probe pulse obtained from the idler output of the OPO, which is linearly polarized along the direction of the current flow, i.e. from electrode to electrode. It is focused to a spot size of approximately 4 μm
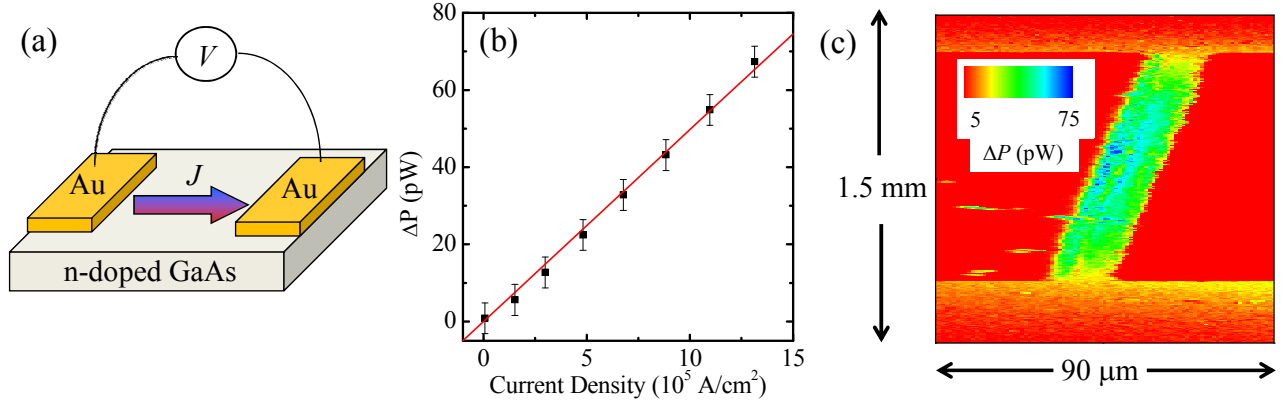
Figure 6.3: (a) Schematic of the device used for electrical injection of current. (b) Change in second harmonic power (ΔP) caused by the charge current as a function of current density. (c) Spatial map of ΔP in the device for a fixed current density of 10^6 A/cm^2. Data from Ruzicka *et al.*[8]

FWHM at the same side as the electrodes using a microscope objective lens, as in the previous experiments. This wavelength is chosen so that even the two photon transition should not be possible, since this transition energy (1.38 eV) should still be below the band gap (1.42 eV[119]) and therefore the probe will not excite any background carriers. With no current present, this sample emits a SH at the surface, with a power of about 100 nW, much larger than the expected power of the current-induced SH. Hence, this surface SH can be used as the local oscillator, as discussed in Sec. 6.3.2.

Finally, the transmitted SH of the probe pulse at 900 nm is collected by another objective lens, and is detected by a silicon photodiode. A combination of bandpass and color filters is used in front of the photodiode in order to block the probe and the photoluminescence of the sample. In addition, the photodiode is not sensitive to the strong probe at 1800 nm. For the lock-in detection, the current is modulated on and off by modulating the applied voltage with a square wave. Therefore, under this modulation scheme we are directly measuring ΔP, i.e. the change in power of the SH caused by the current. Also, in order to avoid any attenuation of the current caused by the frequency response of the device, we use a small modulation frequency of 10 Hz.

We start by changing the applied voltage (and therefore the current density) and measuring ΔP at the center of the gap between the two electrodes. As discussed in Sec. 6.2 and Sec. 6.3.2, if

this change in SH is current induced, ΔP should be proportional to J. Indeed, Fig. 6.3(b) shows that this is the case. (Data from Ruzicka *et al.*[8]) Furthermore, although not shown in the figure, ΔP flips sign when the direction of the current is reversed, but retains the same amplitude. This is expected as well based on Eq. (6.14). Since $\chi_J^{(2)} \propto J_x$ and there is no constraint on the sign of $\chi_J^{(2)}$, a negative J_x leads to a negative $\chi_J^{(2)}$, which in turn flips the sign of the current induced field, E_J. The magnitude of the field does not change, but since the experiment is under the unique conditions of $\Delta P \propto E_J$ [Eq. (6.19)] and the lock-in detection technique is sensitive to the phase of the the field, this sign flip is observed.

Next, we measure ΔP at various positions throughout the device by scanning the laser spot and the result is shown in Fig. 6.3(c). For this measurement it is important to note a few key points. First, in order for such a measurement of ΔP to be reliable, we must verify that the surface SH, P, does not change. From the top to the bottom of the figure, where no electrodes are present we saw less than 5% variation on ΔP indicating that the focus did not change substantially despite movie a rather large distance. There was however some variation in P in some random areas of the device that may be due to some dirt, defects, or residue material from the fabrication of the electrodes. These spots show up as the randomly positioned dark/light blue spots in the figure. Additionally, when the probe spot approaches the electrodes, obviously P will change dramatically as more of the laser hits the metal rather than the semiconductor. For this reason, the value of ΔP near the electrodes is not accurate. Hence, this is likely the cause of the apparent inbalance in ΔP (and therefore the current density) between the left and right side of the gap – it is very difficult to accurately measure and model P and ΔP at these positions. Finally, the the step size in the vertical direction was about 5 μm and the step size in the horizontal direction was 1 μm, while the spot size was 4 μm FWHM. Hence the figure is not to scale with respect to the vertical and horizontal dimensions.

Despite these drawbacks, this measurement does qualitatively show the expected behavior at positions away from the electrodes. Namely, large signals are observed in the gap between the two electrodes (the greenish strip) and the signal goes to zero as we move farther away from the

electrodes. Although the geometry of this device is simple, this measurement demonstrates that the current-induced SHG can be used to obtain a real space image of current density. As such, it can be used to determine the spatial distribution of current density in a much more complex device, and will have even more success if the probe spot size can be reduced further.

It should also be noted that in this configuration, the current is generated by the applied electric field, and such a field is known to induce a SHG.[120–125] However, in such a highly conductive sample, the field effect is expected to be small compared to the current effect. We confirm this by a simple order-of-magnitude estimate: Theoretical calculations based on the detailed theory of Jacob Khurgin[86] give the relation between nonlinear susceptibility and current density as $\chi_J^{(2)}/J \approx 2 \times 10^{-22}$ m^3/W under these experimental conditions. On the other hand, calculations for the electric field induced effect based on Miller's rule[117] and experimental data[126] indicate that the the same relation for this effect is $\chi_E^{(2)}/J < 0.5 \times 10^{-23}$ m^3/W, where $\chi_E^{(2)}$ is the electric field induced $\chi^{(2)}$.

6.4.2 Optical injection of a ballistic charge current

Now that the current-induced SH effect has been demonstrated for a current injected electrically, we can use this to study a ballistic current injected by the QUIC technique. To inject the current, electrons are excited in the 400-nm bulk GaAs sample of the spin-polarized charge current experiment discussed in Sec. 5.4.1 by one-photon absorption of a 290-fs 750-nm pulse and and two-photon absorption of a 75-fs, 1500-nm pulse. Both pulses are incident normal to the sample and are tightly focused to 2-3 μm at the sample surface. Since the goal is to inject a pure charge current, both pulses are linearly polarized along an arbitrarily chosen $\hat{x}$ direction. This causes electrons to be excited to the conduction band with an average velocity $v_0 \sin(\Delta\phi)\hat{x}$, where $\Delta\phi$ is again the relative phase of the two transitions and v_0 is on the order of 30 nm/ps for this experiment.[79,81,82,93,127,128] With a carrier density on the order of 10^{17}-10^{18} /cm^3, the injected current density will be $J \approx 10^5$ A/cm^2. Since there is no driving force, the current is transient, but the sample is cooled to 10 K in order to extend its lifetime.
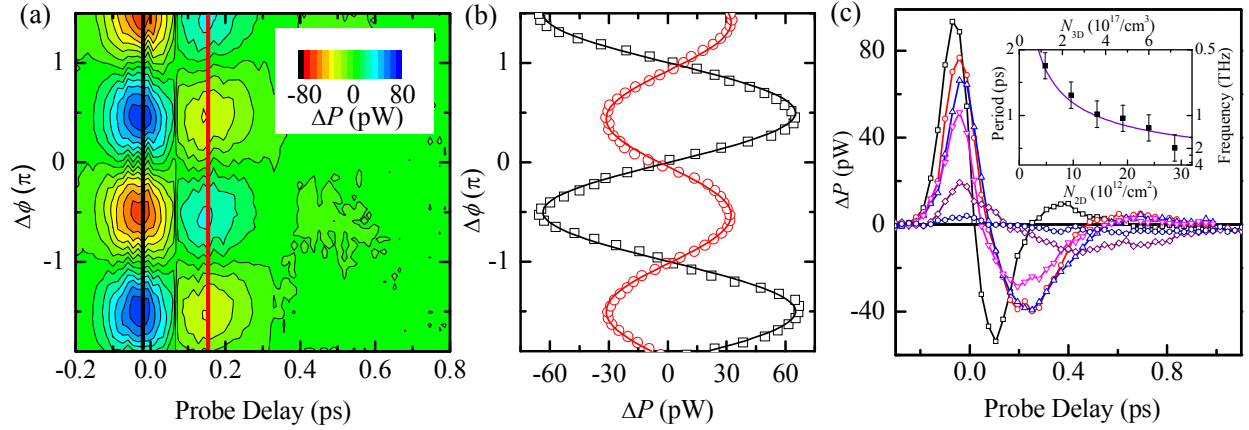
Figure 6.4: Second harmonic generation induced by a ballistic charge current injected using quantum interference and control. (a) The measured ΔP as a function of the probe delay and $\Delta\phi$, when the pump and probe spots are overlapped ($x = 0$). (b) Two cross sections of (a) with fixed probed delays of -0.02 and 0.15 ps, respectively, as indicated by the vertical lines in (a). (c) ΔP as a function of probe delay for carrier densities of 7.2 (squares), 6.0 (circles), 4.8 (up triangles), 3.6 (down triangles), 2.4 (diamonds), and 1.2×10^{17} /cm^3 (hexagons), measured with a fixed $\Delta\phi = \pi/2$. The inset shows the period (left axis) and the frequency (right axis) of the oscillations for the carrier density used (top axis) and corresponding two dimensional carrier density (bottom axis). The solid line is a fit with $\sqrt{N_{2D}}$. Data from Ruzicka et al. [8]

The SHG induced by the optically injected current is observed by using an $\hat{x}$-polarized, 0.1-nJ, 170-fs probe pulse obtained from the idler output of the OPO. For this experiment, the output is tuned to 1760 nm. The probe is focused to a spot size of 2.1 μm from the back side of the sample and the SH of the probe pulse (at 880 nm) is collected by the pump-focusing lens and subsequently sent to the silicon photodiode. Similar to the DC measurement, the current-induced SH is amplified by the surface SH, which for this sample and the powers used here (about 10 mW probe power) has an optical power of 4 nW. A combination of bandpass and color filters is again used in front of the photodiode, this time in order to block the unwanted beams, which includes the pumps, the probe, and the photoluminescence of the sample. Also, the photodiode is again not sensitive to the strong probe at 1760 nm and the 1500-nm pump.

Figure 6.4(a) shows the detected ΔP as we vary $\Delta\phi$ and the time delay between the current-injecting pulses and the probe pulse. (Data from Ruzicka et al. [8]) At each probe delay, $\Delta P \propto \sin(\Delta\phi)$, as shown by the solid black and red lines in Figs. 6.4(a) and (b). Since $J \propto \sin(\Delta\phi)$, we

again confirm that $\chi_J^{(2)} \propto J$, which is consistent with Fig. 6.3(b). In this case where the current was injected by the QUIC technique, we know for certain that the current only travels in one direction. Hence, we are able to confirm by rotating a polarizer in front of the detector that the SH is linearly polarized along the $\hat{x}$ direction, i.e. the direction of the current. Furthermore, we verify that with a $\hat{y}$-polarized probe pulse (i.e. perpendicular to the direction of the current) the ΔP is reduced by at least 1 order of magnitude. Therefore, in this configuration the SHG effect can be used to measure both the magnitude and the direction of the current density.

Figure 6.4(c) shows ΔP as a function of probe delay for a certain fixed value of $\Delta\phi$ with different carrier densities. As expected from a plasma oscillation, similar to what was observed in spin polarized charge current measurements of Sec. 5.4.1, ΔP oscillates in time. Again, this arises due to the fact that electrons and holes are injected with opposite crystal momenta. Once they separate, a strongly nonuniform space charge field develops, which decelerates the carriers and causes the current density to drop. After the carriers reach their maximum displacements and the current density simultaneously drops to zero, they are driven back towards the origin by the space charge field, which gives rise to a negative current. As shown in the data, such a plasma oscillation is strongly damped, due to scattering and the field inhomogeneity,[129] so its magnitude decreases greatly even before the first period is complete. Furthermore, we find that with different $\Delta\phi$, and hence different injected average velocity, the magnitude, but not the frequency, of the oscillation changes. This is also consistent with a plasma oscillation, in which the amplitude of the oscillation is determined by the initial velocity, but the frequency is independent of it.

These measurements with different carrier densisites and fixed $\Delta\phi = \pi/2$ in Fig. 6.4(c) also demonstrate that both the magnitude and the frequency of the oscillation increase with the carrier density. The inset of Fig. 6.4(c) shows the periods and the frequencies of the oscillation plotted against the two- and three-dimensional carrier density (N_{2D} and N_{3D}, respectively). The periods are deduced by using the time difference between the first and the second zero-crossing points for each curve. Because of the large uncertainties of the data, we do not attempt to accurately analyze the dependence of the frequency on the carrier density. However, we found that the data is consistent

with the $\sqrt{N_{2D}}$ dependence expected for a two-dimensional plasma oscillation,[129] as indicated by the solid line. These measurements demonstrate that the current-induced SHG can be used to *time-resolve* the ultrafast dynamics of these currents. Also, in comparison to the differential pump-probe measurements presented in Chapter 5 where the charge separation was measured, these are direct measurements of the current density.

Since in this experiment we can accurately know the injected current density and the transition properties of the GaAs, we are able to estimate the size of the nonlinearity induced by the transient current from the measured values of ΔP and compare this with the expected theoretical value. For the GaAs sample used in this experiment, calculations performed by Jacob Khurgin using his theory[86] indicate that a current density of 10^5 A/cm^2 is expected to induce a $\chi_J^{(2)} \approx 0.07$ pm/V. To obtain the $\chi_J^{(2)}$ from the measurements, we assume a perfect phase matching in the SHG and solve coupled wave equations,[117] which is valid since the sample thickness is smaller than the coherence length. Also, since $E_J \ll E_{LO}$ in this experiment, we can use Eq. (6.19). Calculations performed by Hui Zhao using these assumptions indicate that the ΔP of 20 pW from a 10 mW probe of a 10^5 A/cm^2 current density corresponds to a $\chi_J^{(2)} \approx 0.05$ pm/V.[8] Therefore, the theoretically predicted value is reasonably consistent with the value measured experimentally.

6.5   Summary

A charge current in a semiconductor induces a second order susceptibility, $\chi^{(2)}$, that is proportional to the current density. This $\chi^{(2)}$ can be used as a method to measure current density, since a probe electric field that is incident on a material with a nonzero $\chi^{(2)}$ will lead the generation of an electric field with double the frequency of the probe field. This current induced SHG is very weak, but can be amplified using a homodyne detection scheme. Hence it is possible to detect a current density by measuring a current induced SHG.

Experimental results from a steady state current that was injected by a pair of electrodes and driven by a function generator were presented. We observed that the SHG increased linearly with

increasing current density and used this technique to map out the current density in a simple device. This measurement was then extended to study a ballistic charge current that was injected using the QUIC technique. Using the SHG technique we observed a plasma oscillation with multiple oscillations. These results serve as a demonstration that this optical effect of charge current can be detected and that this effect has many potential experimental applications. Also, the measurements demonstrate that this technique can be used to spatially map out a current density, and directly time resolve the dynamics of a ballistic charge current.

Chapter 7

Summary and future work

Ultrafast laser techniques can be used to study a wide variety of properties of semiconductors. This is achieved through the interaction of light with semiconductors, which allows a great deal of information to be obtained. First, time resolved pump probe measurements were discussed. In these measurements, a pump laser pulse is used to excite carriers in a sample by choosing the correct wavelength. The carriers are then studied by using a second probe laser pulse. The differential transmission or reflection, i.e. the normalized change in transmittance or reflectance caused by the photoexcited carriers, is directly proportional to the density of carriers at the probing energy. Therefore, by changing the time delay between the pump and probe laser pulses, information can be obtained about the carrier energy relaxation time or lifetime.

Since these signals can be small compared to the fluctuation in the probe laser intensity, lock-in detection techniques are used: The transmitted or reflected probe beam is sent to a photodiode and the output of the photodiode is sent to a lock-in amplifier. If the intensity of the pump beam is modulated and the lock-in amplifier is referenced to this modulation frequency, its voltage output will be proportional the the change in transmission or reflection caused by pump, and is therefore proportional to the density of carriers excited by the pump at the probing energy. This lock-in technique in conjunction with the time delay probe pulse was used to measure important quantities in reduced graphene oxide. The results that were discussed indicate that this type of graphene is

similar to other types of graphene and also some properties of the optical phonon emission time were deduced.

By adding spatial resolution to the time resolved pump-probe measurements, we are also able to obtain information about the diffusion of carriers in semiconductors. This is achieved by measuring the carrier density profile as a function of time by scanning the probe beam across the pump beam and measuring the differential transmission or reflection at each position for various time delays. Since the laser spots are Gaussian in shape and a diffusion of Gaussian profile of carriers will cause the profile to remain Gaussian, but grow wider, these measurements can be used to directly deduce the carrier diffusion coefficient. This measurement, which since it is all optical does not affect the properties of the material, can then be used as a direct way to measure the carrier mobility, as long as the carrier temperature is known. Results on the temperature dependence of the diffusion coefficient in a GaAs bulk sample were presented, and the calculated mobilities at each temperature agreed well with mobilities measured by electrical methods. The technique was also extended to several other semiconductors including graphene, single walled carbon nanotubes, and Si/SiGe quantum well structures.

Ultrafast laser techniques can be used to study ballistic transport as well. A ballistic current can be injected by simultaneously using one-photon absorption of a photon of frequency 2ω and two-photon absorption of photons of frequency ω to excite carriers in a semiconductor. The two transitions will interfere, resulting a non-symmetric distribution of carriers in k-space. By controlling the phase between the two optical fields, the injected velocity can be directly controlled. Additionally, different types of currents can be injected by controlling the relative polarizations of the ω and 2ω fields. Parallel linear polarizations will inject a pure charge current along the polarization direction, perpendicular linear polarizations will inject a pure spin current along the ω polarization direction, and same circular polarizations will inject a spin polarized charge current along a direction determined by the relative phase of the two fields. These ballistic currents can be detected using a differential pump-probe technique. In this case the accumulation of charge or spin is used to deduce the distance that the charge or spin traveled. To detect such a signal, we

modulate the current density by modulating the phase of the two fields.

These techniques for studying ballistic currents were used to demonstrate the injection and temporal resolution of an oscillating spin polarized charge current pulse in GaAs. Also, results were present in which the efficiency of the injection of currents using quantum interference was studied using pure spin current. It was found that the efficiency of the interference follows the classical pattern of two interfering optical fields and that the most efficient interference occurs when the carrier densities injected by the two different transitions are the same.

Finally, an optical effect of charge currents that can be used to directly optically sense the current density was discussed. Theoretical calculations have predicted that a charge current will induce a nonzero second order susceptibility, $\chi^{(2)}$. This $\chi^{(2)}$ is proportional to the density of the current, regardless of the material being studied. This $\chi^{(2)}$ can be observed through second harmonic generation – a probe beam of frequency ω is sent to the location of the current and if a nonzero current is present, the nonzero $\chi^{(2)}$ will lead to the generation of a field of second harmonic frequency, 2ω. This effect was demonstrated on a steady state current that was driven through an n-doped GaAs bulk sample via a pair of metal electrodes. This measurement shows that such an effect can be used to spatially resolve a current density distribution as well as temporally resolve the dynamics of a ballistic current.

Each of these techniques have provided interesting and important information about several different materials, as discussed throughout the dissertation. The more unique techniques – namely the spatially and temporally resolved pump-probe measurements of diffusion coefficient, QUIC techniques for injection of ballistic currents, and current induced second harmonic technique for the detection of currents – are remarkably special for their abilities to study carrier transport. Since they can all be readily extended to a wide variety of semiconductors and materials, they provide excellent methods for studying carrier transport in materials in which these properties are otherwise difficult to access, specifically low dimensional materials in which it is structurally difficult to use electrical methods for transport studies. Therefore they have the potential to provide some very unique and interesting information about both diffusive and ballistic carrier transport and in some

cases may be the only techniques that can be used to gain such important knowledge.

Appendix A

Lock-in detection techniques

This section describes the output of the lock-in amplifier for the various modulation schemes that were used. While everything is discussed in terms of transmission only, the same results apply for measurements involving reflection. The first section describes the measurement of the linear transmission, T_0. This is then followed by a discussion of the differential transmission caused by modulation of the pump intensity and then by differential transmission caused by modulation of the phase between ω and 2ω fields, which is used for quantum interference and control experiments. This discussion is based on an unpublished note by Hui Zhao.[130]

A.1 Linear transmission

To measure the transmission of the probe pulse, T_0, we chop the probe and send the probe beam to a detector after it passes through the sample. Assume the detector consists of a photodiode with efficiency A. Then, the voltage out of the photodiode is

$$V_S(t) = AI(t)T_0, \tag{A.1}$$

where $I(t)$ is the intensity of the probe beam before the sample. Although the beam is pulsed with an 80 MHz repetition rate, since this rate is much smaller than the bandwidth of the detector, the

laser intensity can be considered as constant. Since the probe is being chopped, the intensity will be modulated with a square wave:

$$I(t) = I_0 \left[\frac{1}{2} + \frac{2}{\pi} \sum_{n=1,3,5,...}^{\infty} \frac{1}{n} \sin(n\Omega_C t + \theta_C) \right], \tag{A.2}$$

where I_0 is the intensity of the probe before the chopper, Ω_C is the chopping frequency, and θ_C describes the phase of the resulting intensity function.[38] The photodiode will then output a voltage described by

$$V_S(t) = A T_0 I_0 \left[\frac{1}{2} + \frac{2}{\pi} \sum_{n=1,3,5,...}^{\infty} \frac{1}{n} \sin(n\Omega_C t + \theta_C) \right]. \tag{A.3}$$

This output voltage, which we call the signal, is then sent to a lock-in amplifier. The lock-in amplifier essentially multiplies the signal by a reference voltage $V_R \sin(\Omega_R t + \theta_R)$. The lock-in reference voltage is synced with the chopper, and therefore has the same frequency ($\Omega_R = \Omega_C$) as the signal. We also choose the phase of the reference voltage so that it is equal to the signal ($\theta_R = \theta_C$). Assume for simplicity that $\theta_C = \theta_R = 0$. The lock-in then filters out the frequency components of the signal that are different from the chopping frequency. This ammounts to integrating the signal multiplied by the reference voltage over the integration time, T_{int}, which is much longer than the period of oscillation of the signal. This results in an output voltage of

$$
\begin{aligned}
V_{\text{out}} &= \frac{1}{T_{\text{int}}} \int_0^{T_{\text{int}}} V_R \sin(\Omega_R t) V_S(t) dt \\
&= \frac{1}{T_{\text{int}}} \int_0^{T_{\text{int}}} V_R \sin(\Omega_R t) A T_0 I_0 \left[\frac{1}{2} + \frac{2}{\pi} \sum_{n=1,3,5,...}^{\infty} \frac{1}{n} \sin(n\Omega_C t) \right] dt \\
&= V_R A T_0 I_0 \frac{1}{T_{\text{int}}} \int_0^{T_{\text{int}}} \sin(\Omega_R t) \left[\frac{1}{2} + \frac{2}{\pi} \sum_{n=1,3,5,...}^{\infty} \frac{1}{n} \sin(n\Omega_C t) \right] dt \\
&= V_R A T_0 I_0 \frac{2}{\pi} \frac{1}{T_{\text{int}}} \int_0^{T_{\text{int}}} \sin(\Omega_R t) \sin(\Omega_C t) dt \\
&= V_R A T_0 I_0 \frac{2}{\pi} \frac{1}{T_{\text{int}}} \int_0^{T_{\text{int}}} \sin^2(\Omega_R t) dt \\
&= V_R A I_0 \frac{T_0}{\pi}. \tag{A.4}
\end{aligned}
$$

Here, we have taken advantage of the fact that the average value of two sine functions multiplied together (both with fundamental frequency ω_f, and therefore period $2\pi/\omega_f = T_f$) is:[131]

$$\langle \sin(m\omega_f x)\sin(n\omega_f x)\rangle = \frac{1}{T_f}\int_0^{T_f}\sin(m\omega_f x)\sin(n\omega_f x)\,dt = \begin{cases} 0 & \text{if } m \neq n \\ \frac{1}{2} & \text{if } m = n \neq 0 \end{cases}. \qquad (A.5)$$

Since $T_{\text{int}} \gg 2\pi/\theta_C$, this holds for our experiment (typical values are a chopping frequency of 2.1 kHz, which corresponds to a period of 0.5 ms – typical integration times for measurements are 300 ms to 1 s). Therefore, by chopping the probe and sending the probe pulse through the sample to a detector, which is connected to a lock-in amplifier, we can measure the linear transmission, T_0, of the probe pulse through the sample.

A.2 Differential transmission

To measure the differential transmission of the probe pulse, we send both pump and probe pulses to the sample, chop the pump pulse, and send the probe pulse to the detector. If the pump beam intensity is I_{pump}^0 before the chopper, then with chopper modulation, the pump intensity that reaches the sample will be

$$I_{\text{pump}}(t) = I_{\text{pump}}^0\left[\frac{1}{2} + \frac{2}{\pi}\sum_{n=1,3,5,\ldots}^{\infty}\frac{1}{n}\sin(n\Omega_C t + \theta_C)\right]. \qquad (A.6)$$

We know that for our experiments, the pump modifies the transmission by

$$\Delta T = BI_{\text{pump}}^0, \qquad (A.7)$$

98

i.e. the differential transmission is proportional to the pump intensity. Since the probe (still of intensity I_0) is being detected, the voltage signal out of the photodiode will be

$$
\begin{aligned}
V_S(t) &= AI_0(T_0 + \Delta T) \\
&= AI_0 T_0 + AI_0 BI_{\text{pump}}^0 [\frac{1}{2} + \frac{2}{\pi} \sum_{n=1,3,5,...}^{\infty} \frac{1}{n} \sin(n\Omega_C t + \theta_C)].
\end{aligned}
\tag{A.8}
$$

The signal from the photodiode is then sent to the lock-in amplifier, which produces the output signal in the same way as above (assuming again that the reference and signal frequencies are the same and that both have phase 0):

$$
\begin{aligned}
V_{\text{out}} &= \frac{1}{T_{\text{int}}} \int_0^{T_{\text{int}}} V_R \sin(\Omega_R t) V_S(t) \, dt \\
&= V_R AI_0 BI_{\text{pump}}^0 \frac{1}{\pi} \\
&= V_R AI_0 \frac{\Delta T}{\pi}.
\end{aligned}
\tag{A.9}
$$

Therefore, by chopping the pump and detecting the probe, we directly measure the change in transmission caused by the pump.

A.3 Phase dependent differential transmission

To measure the differential transmission of the probe pulse that is caused by the phase difference between the two pump pulses, for example during the QUIC experiments, we modulate the phase difference between the two pump fields. Assuming the transmission of the probe is determined by both the intensity and the phase of the two pumps, it will be

$$
T = T_0 + \Delta T(\Delta\phi).
\tag{A.10}
$$

As discussed in Chapter 5, the dependence of ΔT on $\Delta\phi$ depends on the type of current being studied. For this discussion we will consider only a pure charge current, which means that

$$\Delta T = \Delta T(\pi/2)\sin(\Delta\phi), \tag{A.11}$$

where $\Delta T(\pi/2)$ is the maximum change in transmission, ocurring when $\Delta\phi = \pi/2$. Similar results will follow for pure spin current and spin polarized charge current.

If we modulate the phase difference as a sine function with amplitude Φ and frequency Ω, then

$$\Delta\phi(t) = \Phi\sin(\Omega t), \tag{A.12}$$

and following the steps of the previous two sections, the signal coming out of the photodiode will be

$$V_S(t) = I_0 A T_0 + I_0 A \Delta T(\pi/2) \cdot \sin[\Phi\sin(\Omega t)]. \tag{A.13}$$

The output of the lock-in amplifier that receives this signal will then be

$$
\begin{aligned}
V_{\text{out}} &= \frac{1}{T_{\text{int}}} \int_0^{T_{\text{int}}} V_R \sin(\Omega_R t) V_S(t)\, dt \\
&= \frac{1}{T_{\text{int}}} \int_0^{T_{\text{int}}} V_R \sin(\Omega_R t)\{I_0 A T_0 + I_0 A \Delta T(\pi/2)\sin[\Delta\phi(t)]\}\, dt \\
&= \frac{1}{T_{\text{int}}} V_R I_0 A \Delta T(\pi/2) \int_0^{T_{\text{int}}} \sin(\Omega_R t)\sin[\Phi\sin(\Omega t)]\, dt \\
&\simeq V_R I_0 A \Delta T(\pi/2) \cdot J(\Phi), \tag{A.14}
\end{aligned}
$$

where $J(\Phi)$ is the first order Bessel function of the first kind of the modulation amplitude, Φ. Hence, the signal is maximum when $\Phi \approx \pi/2$.[38]

Appendix B

Review of graphene

B.1 Basic properties of graphene

B.1.1 Overview of graphene

Graphene in its purest form is a single layer of carbon atoms arranged in a two dimensional hexagonal lattice. This widely studied material has gained popularity very quickly in the past few years, leading to the award of the 2010 Nobel Prize in Physics to Andre Geim and Konstantin Novoselov "for groundbreaking experiments regarding the two-dimensional material graphene." While graphene was not widely popularized until it was explored by Novoselov *et al.* in 2004,[132] it was theoretically studied as early as 1947 by Wallace, as a first step in his discussion of the band theory of graphite.[133] After the 2004 paper by Novoselov *et al.* a flurry of experiments were performed, which outlined properties of graphene that are superior to those for all other known materials. The most well known superior properties of graphene include a high mobility,[132,134] large thermal conductivity,[135] and a large intrinsic strength.[136] These superior properties of graphene, compounded with the low cost of the source material (graphite), and the relative ease of production then led to an explosion of studies on graphene that were directed towards industrial application. For example, graphene has been cited as a great material for use in the development of high speed transistors,[137] DNA biosensors,[138] ultracapacitors,[139] optical modulators,[140] ultrafast

lasers,[141] and as a transparent electrode in solar cells.[142] Related to these potential applications for graphene, new, more efficient methods of producing large area graphene have also been quickly developed, including epitaxial growth of graphene on silicon carbide in 2004,[143] chemically derived graphene,[144,145] and graphene produced by chemical vapor deposition.[146,147] In addition to the application possibilities of graphene, graphene's unique band structure, which causes carriers to move as though they have zero mass and with a very high speed (10^6 m/s)[134] has led to the study of some interesting physics, such as the unconventional quantum hall effect[148] and the Klein paradox.[149]

Many of the superior properties and potential applications of graphene are related to the properties of either phonons or excited electrons and holes, also known as charge carriers. Therefore, optical studies of graphene have proven to be an invaluable resource. For example, Raman spectroscopy has been identified as having the ability to distinguish single layer graphene from multilayer graphene,[150] and as such is widely used as a clear-cut method to demonstrate that one is actually studying graphene in experiment. Besides this, properties of graphene have been studied through experiments involving photoluminescence,[151] second harmonic generation,[152] and optical studies of ultrafast photoexcited carrier dynamics.[153] Of particular interest here are ultrafast time-resolved optical studies of graphene. However, before discussing the results such experiments in detail, a few basic properties of graphene must be discussed.

B.1.2   Fabrication

The method of fabrication of graphene can greatly alter its properties. Currently there are four main methods for the production of graphene: graphene produced by mechanical exfoliation, chemically derived graphene, epitaxial graphene grown on silicon carbide (SiC), and graphene produced by chemical vapor deposition (CVD graphene). While each method of fabrication has certain strengths and weaknesses, as far as the relative ease/cost of production and quality of the graphene itself goes, all four of these methods are widely used in the attempted fabrication of devices and in purely experimental studies, with some showing more prominence in some areas than others.

(~ 10 times)
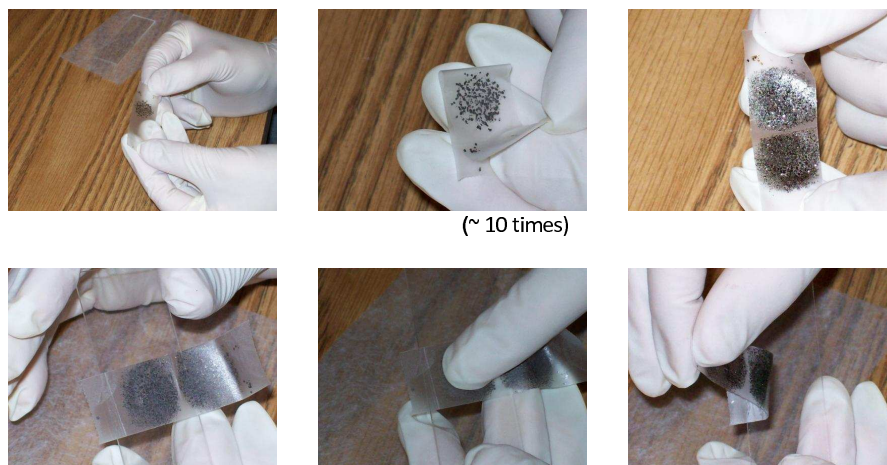
Figure B.1: Procedure for producing graphene by mechanical exfoliation of bulk graphite.

B.1.2.1 Mechanical exfoliation of bulk graphite

Mechanically exfoliated graphene involves using tape to mechanically peel graphene layers from bulk graphite, usually beginning with large graphite flakes, and ending with small areas of pure graphene. The basic steps of this procedure are outlined in Fig. B.1. In this method, as the title suggests, bulk graphite is repeatedly exfoliated using a piece of tape until a thin film of graphite remains. Then, the piece of tape with the thin graphite films is pressed onto a substrate and subsequently peeled off, leaving very small areas of graphene behind on the substrate. Due to the main tool involved in this method being the tape, this method is also widely known as the "Scotch tape method." While a crude following of this method can only produce very small patches of graphene with areas about 5 μm^2, careful cleaning of the substrate with various acid/water solutions and careful choice of the substrate and type of starting graphite can lead to patches of graphene as large as 200 μm^2, or even larger.[154]

Although this method of production of graphene is very simple, the main difficulty lies in actually finding the graphene once it has been produced. Subtle interference effects make this type of graphene visible to the naked eye when the substrate used is SiO$_2$ with a thin silicon coating, but since the pieces are typically much smaller than the unwanted yet unavoidable and much thicker graphite films, they can be difficult to locate and use to fabricate a device.[155] Also, since it is very

hard to repeatedly and uniformly produce large area graphene pieces, this method of production of graphene has nearly no hope for future use in industry. However, graphene produced by this method does have several advantages. First, the graphene will typically be of higher quality, i.e. contain fewer grain boundaries and lattice defects, since this type of graphene is derived from graphite, which contains, by definition pure graphene sheets stacked together. This is because the strong carbon-carbon bonds in the graphene planes which stack together to make up graphite are much stronger than the relatively weak inter-layer bonds of graphite. So, graphene produced in this way is ideal for studying the intrinsic properties of graphene, especially when suspended so that the substrate no longer plays a role,[135,156,157] and as a result this type of graphene has been demonstrated to have the highest mobility of 120,000 cm^2/Vs.[158] The mobility of this type of graphene is typically on the order of 10,000 cm^2/Vs.

B.1.2.2 Chemical derivation

This method of production of graphene may refer to a large variety of methods, any of which typically use liquid chemicals as the main production tool. One such method that is widely used involves the reduction of graphene or graphite oxide to produce graphene. First, graphite oxide is synthesized from graphite powder using a modified Hummers method, which involves mixing the powder with a mixture of sulfuric acid, sodium nitrate and potassium permanganate.[49,159] The graphite oxide is then mixed with water, and is easily exfoliated by sonication, leading to the formation of graphene oxide, i.e. the graphite oxide is pulled apart layer by layer, similar to the mechanical exfoliation. This dispersion can then be deposited onto a substrate by a variety of methods, for example by spin coating or simple drop coating. The oxygen is then removed by chemical reduction with the hydrazine vapor, which also reestablishes the carbon-carbon bonds, leaving graphene on the substrate.[160] Graphene produced by this method is referred to as reduced graphene oxide.

Reduced graphene oxide has many benefits compared to other types of graphene. Since it is in solution form as a step in its production process, it can be readily applied to large-area substrates.

It has also been demonstrated that this type of graphene can be printed onto large-scale flexible substrates, indicating that this type of graphene may be a candidate for use in transparent electronics on flexible substrates. All-graphene source-drain channel electronics have been fabricated with hole and electron mobilities as high as 365 and 281 cm^2/Vs, respectively.[145] This, in addition to its relative ease of production, and low cost of materials required makes this type of graphene a good potential candidate for use in electronic devices. However, one disadvantage of this type of graphene is that it has a typically lower carrier mobility than graphene produced by other methods. This is due to the large number of grain boundaries and defects, which is something unavoidable due to the method used for production. The mobility of graphene produced by this method is typically on the order of 300 cm^2/Vs.

B.1.2.3 Epitaxial growth on silicon carbide

This method of production of graphene was actually being developed almost concurrently with the demonstration of graphene by Novoselov *et al.*, but it is likely that they did not realize that they were actually studying graphene. In this method, a silicon carbide (SiC) crystal is heated at a high temperature ($> 1200\ ^{\circ}$C) for a certain amount of time, causing desorption of the silicon, leaving graphene layers on the surface of the crystal. The number of graphene layers is determined mainly by the temperature,[143] and this method can produce typically between a few and 100 graphene layers.[161] It was later found that although there may be multiple graphene layers present, the each layer still acts like graphene due to rotational stacking faults, which cause neighboring layers to be uncoupled, and hence electrons are not able to travel between layers.[162]

This type of graphene does have potential use in industry, specifically in the fabrication graphene-based transistors. It can be patterned using standard nanolithography methods, leading to the ability to form submicrometer structures.[163] Also, like chemically derived graphene, this production method can produce large-scale graphene samples.[164] Finally, an insulating substrate (the SiC) is already present, which is convenient for the fabrication of epitaxial graphene FETs,[164] and 100-GHz graphene transistors have already been demonstrated, using epitaxial graphene.[137] Of course,

epitaxial graphene on SiC also has its disadvantages. For example, the first graphene layer will be highly doped due to charges from the silicon, which can change the overall structure of the sample, and has been cited as playing a role in time-resolved optical experiments.[153,165] The mobility of graphene produced by this method is typically on the order of 1,000 cm^2/Vs.

B.1.2.4   Chemical vapor deposition

This method of production of graphene involves using a chemical vapor to deposit carbon atoms onto a substrate. First, a substrate is chosen, usually nickel or copper. Then, after exposure a gas mixture containing methane, hydrogen and argon, if the sample is cooled quickly enough, graphene will remain. The thickness of the graphene samples (i.e. number of graphene layers deposited) can be controlled by varying the thickness of the substrate and the growth time.[146] The graphene can then be transferred to another substrate by coating the product with a material, in this case polydimethylsiloxane (PDMS) and then etching away the nickel with $FeCl_3$, but also polymethylmethacrylate (PMMA) can be used as a coat, which is then transferred to another arbitrary substrate and subsequently dissolved in acetone.[166]

One advantage of this type of graphene is that it can easily be patterned, by simply patterning the growth substrate. This makes this type of graphene great for use in devices, as nearly arbitrary shapes of graphene can be made. Also, this method can produce large-area graphene films, centimeters in size, with predominantly single layers.[147] Even after transfer to different substrates, graphene produced in this way typically displays mobilities on the order of 3,000 cm^2/Vs. One problem with this type of graphene is that residue materials that are left behind, specifically those used to transfer to the graphene to a different substrate, may cause difficulty for certain optical experiments.

B.1.3   Electronic properties

Graphene's unique electronic properties are what make graphene such an interesting material. The most well known of these is the linear dispersion relation, which describes electrons and holes.
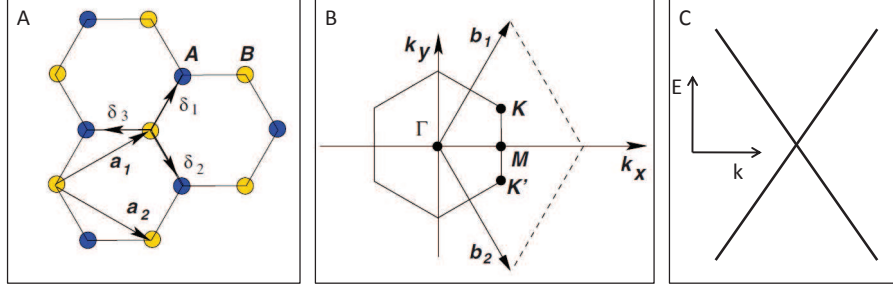
Figure B.2: The lattice structure, Brillouin zone, and energy band structure of graphene. A: The lattice structure of graphene. $\mathbf{a}_1$ and $\mathbf{a}_2$ are the lattice vectors and the δ_i are the nearest-neighbor vectors. B: the corresponding Brillouin zone. $\mathbf{b}_1$ and $\mathbf{b}_2$ are the reciprocal lattice vectors. C: The energy band structure of graphene near the corners of the Brillouin zone, as calculated using the tight-binding model. Panels A and B taken from Castro Neto $et\ al.$[167]

Since the majority of the experiments discussed here involve the dynamics of excited electrons and holes, a brief discussion of some basic electronic properties is necessary.

B.1.3.1   Lattice structure and dispersion relation

As stated previously, graphene consists of a single two dimensional layer of carbon atoms arranged in a hexagonal lattice. The carbon atoms in graphene are held together by a strong σ bond, which arises due to the sp^2 hybridization between one s orbital and two p orbitals.[167] Figure B.2 shows the lattice structure, Brillouin zone, and approximate energy band structure of graphene. The lattice vectors can be written as

$$\mathbf{a}_1 = \frac{a}{2}(3, \sqrt{3}) \quad \text{and} \quad \mathbf{a}_2 = \frac{a}{2}(3, -\sqrt{3}), \tag{B.1}$$

where $a \approx 1.42$ Å is the carbon-carbon distance.[167] Using the standard definition,[168] the reciprocal lattice vectors are then:

$$\mathbf{b}_1 = \frac{2\pi}{3a}(1, \sqrt{3}) \quad \text{and} \quad \mathbf{b}_2 = \frac{2\pi}{3a}(1, -\sqrt{3}). \tag{B.2}$$

Three of the four valence electrons are tightly bound to the carbon atoms,[133,167] and therefore a good approximation of the energy band structure of graphene can be calculated using the tight-

binding model. Due to the hexagonal structure of the lattice, tight-binding model calculations indicate that near the corners of the Brillouin zone [$\mathbf{K}$ and $\mathbf{K}'$ points in Fig. B.2(b)], the energy dispersion relation is

$$E(\mathbf{k}) \approx \pm \hbar v_F |\mathbf{k}|, \tag{B.3}$$

where v_F is the Fermi velocity ($v_F \approx 10^6$ m/s), $+$ $(-)$ is for electrons (holes) in the conduction (valence) band, and $\mathbf{k}$ is the wave vector relative to $\mathbf{K}$ and $\mathbf{K}'$ ($|\mathbf{k}| \ll |\mathbf{K}|, |\mathbf{K}'|$).[133,167] This linear approximation of the dispersion relation is valid for energies that are smaller than 1 eV,[32] and since this is the range of energies used in most experiments, this is the description that will be used from this point on.

B.1.3.2 Equation of motion for carriers in graphene

Due to the linear dispersion relation, it is clear that the effective mass approximation will not work for graphene. Hence, a description of the motion of carriers in graphene is slightly more complicated than using the free electron model. The two different but equivalent sublattices [labeled A and B in Fig. B.2(a)] cause carriers to have a pseudospin quantum number in addition to the spin and orbital quantum numbers. This means that the motion of carriers is described in the same way as massless Dirac fermions, i.e. the Dirac equation should be used rather than the Schrodinger equation.[32,167] For this reason, the point at which the conduction and valence bands meet is often referred to as the Dirac point. A detailed discussion of this is not necessary here, however there are two important points that should be noted. First, this means that carriers act as if they have no mass, and the second is the existence of the pseudospin. Also, while this could be seen more as a result of the linear energy dispersion, carriers in graphene always move at the same velocity, $v_F \approx 10^6$ m/s.

B.1.3.3 Energy distribution and density of states

Since carriers in graphene are Fermions, any thermalized energy distribution, i.e. a collection of carriers with different energies that can be characterized by a single temperature, will be described

using Fermi-Dirac statistics. Hence, the probability for finding a carrier with energy E, when the distribution is at temperature T is

$$f_0(E) = \frac{1}{1 + e^{(E-E_f)/k_B T}},$$ (B.4)

where E_f is the Fermi energy and k_B is Boltzmann's constant.[169] Also, the linear electronic band structure leads to a linear density of states:

$$g(E) = \frac{g_s g_v E}{2\pi(\hbar v_F)^2},$$ (B.5)

where g_s and g_v are the spin and valley degeneracy factors (both 2 for graphene) and v_F is the Fermi velocity from above.[32]

B.2 Optical properties of graphene

This review is concerned with ultrafast optical studies of graphene, so a brief review of previous steady state optical studies of graphene is necessary. Here, the optical properties of graphene are broken down into four main sections: general optical properties, including its absorption properties, properties of phonons in graphene, photoluminescence, and second harmonic generation. Ultrafast optical studies of graphene, which are the main focus of this review will be discussed in detail separately.

B.2.1 General optical properties

The most basic optical property of graphene, which must be discussed before the others concerns its absorption of light. The absorbance of graphene is about 2.3% over the range of 400 to about 2500 nm. Interestingly, graphene's absorbance is not just a random value, but is determined by the fine structure constant, $\alpha = e^2/\hbar c \approx 1/137$. Specifically, the absorbance of a single graphene layer is $\pi\alpha$. This is a consequence of the two-dimensional nature of graphene and the zero-gap energy

spectrum of electrons.[170,171]

B.2.2 Photoluminescence

Photoluminescence experiments give insight into the relaxation mechanisms of excited carriers in graphene. For this experiment, the graphene is first excited by a laser. The photoluminescence, as well as the reflected excitation laser light is sent to a detector – either a photodiode or spectrometer CCD – and the excitation laser light is removed using filters. Interestingly, although graphene has no band gap, a sizeable emission of light has been observed to occur over the entire visible spectrum range (1.7-3.5 eV), even when the excitation energy is not at the maximum of this range.[151,172,173]

The presence of this broadband and ultrafast photoluminescence in graphene indicates two important things. First, since the photoluminescence is observed at energies higher than the excitation energy, this indicates that carriers are thermalized on very short time scales, i.e. the carrier-carrier scattering rate is very high. Ultrafast pump-probe experiments indicate a carrier relaxation time on the order of a few picoseconds (this will be discussed in more detail later). So, since the carriers are initially excited to form a nonequilibrium distribution, this means that they must be thermalized on a time scale much less then this in order for there to be time for photoluminescence to occur. Second this indicates that electron-hole recombination does play a role in the relaxation of carriers.

B.2.3 Second harmonic generation

Second harmonic generation in graphene is a subject that has not been explored widely, and has only been observed by one group in graphene produced by mechanical exfoliation of bulk graphite, which is on a substrate of Si coated with a 300 nm thick SiO_2 layer.[152,174] An example configuration for this type of experiment is shown in Fig. B.3. A laser of fundamental frequency ω is incident upon the graphene sample. A second order electric susceptibility will then, for sufficiently large electric fields, lead to the generation of the second harmonic of the excitation field, with frequency 2ω. Either the reflected second harmonic or transmitted second harmonic can be
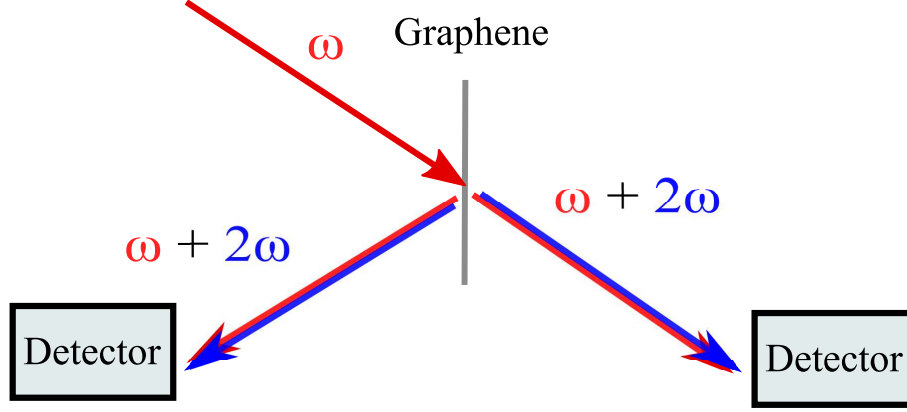
Figure B.3: Example configurations for a second harmonic generation experiment. Either transmitted or reflected second harmonic can be collected by the detector.

collected, and the fundamental beam is either removed with a filter or a detector is chosen that is only sensitive to the second harmonic wavelength.

Although graphene itself is a single layer of carbon atoms, second harmonic generation in graphene can still be treated as coming from either surface, i.e. the part of the graphene where it is in contact with another material In these studies the graphene is surrounded by air on one side, and SiO_2 on the other. It was observed that the magnitude of the second harmonic generation from a single layer of graphene is relatively small, however this is due to the overall cancellation of second harmonic sources on either side of the graphene, which means that the second harmonic generation may be different for different angles of incidence (in these experiments an angle of $60°$ was used), or for graphene on a different substrate. In addition to this, an anisotropic response of the second harmonic generation with respect to the relative orientation of the graphene and the incident light polarization was observed for multilayer graphene (thin graphite films). A threefold symmetry was observed, which arises due to the AB stacking structure.

B.3   Introduction to ultrafast optical studies of graphene

Ultrafast optical studies of graphene can provide much information about the behavior of carriers that is not available from other types of studies, such as those involving steady-state optical or

all electrical measurements. One great advantage of ultrafast optical studies is, of course, the high temporal resolution. This is limited by the temporal width of the laser pulse used in the measurement and can be as low as tens of femtoseconds. In addition to this, several experimental parameters in optical measurements can be easily controlled. The wavelength of a particular laser can typically be readily tuned, giving access to a large range of energies. Also, the wide variety of optics available allow for measurements with high spatial resolution, which is determined by the size of the laser spot on the sample and can be less than 1 μm.

B.3.1 Energy relaxation of carriers

Of particular interest in most ultrafast pump-probe experiments of graphene is the energy relaxation of carriers. As stated earlier, graphene has been cited as an ideal material for use in the fabrication of high-speed transistors due to its very high mobility, and in fact a 100 GHz wafer-scale epitaxial graphene based field-effect transistor (FET) has been demonstrated,[137] among others with lower cutoff frequencies. Of course, in applications such as this graphene based FET, and graphene based solar cells,[175] electromechanical resonators,[176] and ultracapacitors,[139] charge carriers play a crucial role. So, the dynamics, and in particular the energy relaxation of charge carriers in graphene are indeed very important subjects in light of possible industrial applications of graphene. Ultrafast pump-probe experiments are ideal for such studies, since can provide much insight into the energy relaxation dynamics of excited carriers. Using the simple interpretation discussed above, just by monitoring how the differential reflection or transmission signal decays over time, one can ascertain information about the energy relaxation of carriers, as the decrease in the signal directly mirrors the decrease in the density of carriers with energy equal to the probing energy.

For an example differential transmission curve, see Dawlaty *et al.*, which was the first pump-probe experiment published on graphene (in this case epitaxial graphene on SiC). The differential transmission, $\Delta T/T$, is proportional to the density of carriers at the probing energy, so this can be considered as a plot of the density of carriers at the probing energy as a function of time delay. The time difference between which the pump and probe arrive at the sample is called the time delay –

negative time delay means before the pump has arrived, and positive after – and this is controlled by changing the length of the delay stage. These measurements show that the differential transmission signal decays exponentially, with two different time constants. The initial, fast decay time constant is on the order of 100 fs, while the second, slower decay time constant is typically on the order of 1 ps.

The behavior of a differential transmission curve such that in Dawlaty *et al*. can be understood using the schematic of carrier dynamics shown in Fig. B.4, which is based on the results of this and other experiments pump-probe experiments on graphene. The left panel shows the energy band structure of graphene for low energies, with the arrow representing excitation by the pump, and the right panel shows the density of carriers that would be observed at a particular probing energy, $n(E)$, over various time ranges. The pump will excite carriers in the graphene sample, briefly leading to the formation of a nonequilibrium, Gaussian distribution of electrons in the conduction band and holes in the valence band. The distribution will be Gaussian because the energy spectrum of ultrafast short pulse width lasers is typically Gaussian. Also, the average energy of the carriers will be one half of the pump energy if the sample is undoped, since graphene has zero band gap. Then, the carriers will quickly thermalize, within 100 fs, due to carrier-carrier scattering. This is typically the temporal resolution of optical pump-probe experiments, and so cannot be temporally resolved. The experiment performed by Dawlaty *et al.* is a degenerate pump-probe – i.e. the pump and probe are of the same wavelength – and so the rising time of the signal must be determined purely by the pulse width of the lasers. However, in the case of a nondegenerate pump-probe experiment, the rising time is still generally determined by the pulse width of the lasers, since the thermalization time is on the same order of magnitude of the pulse widths of the lasers, and the rapid thermalization, which causes the carriers to spread out in energy into the Fermi-Dirac distribution, is what leads to the increase in density of carriers at the probing energy, and hence an increase in the differential transmission signal. Throughout this process, carriers are radiatively recombining, as discussed in the photoluminescence section, but the carriers are also losing their energy via the emission of optical phonons,[177] and this is the dominant process that causes the

113
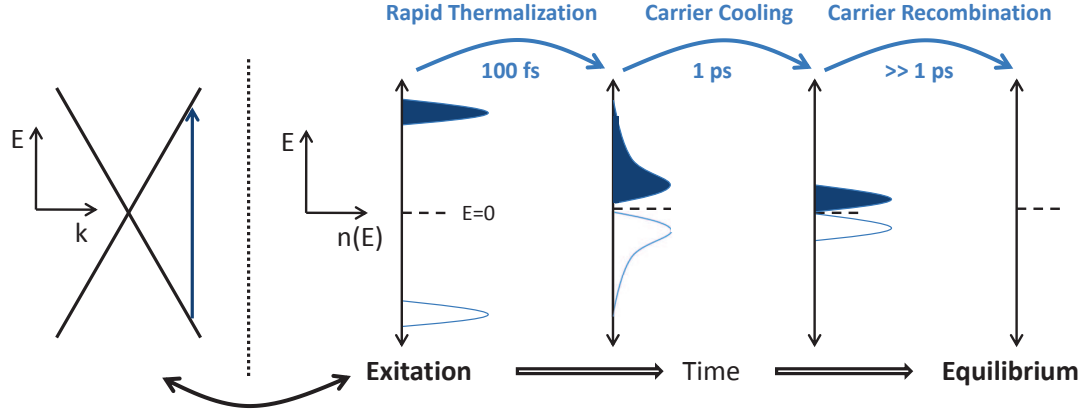
Figure B.4: A schematic showing the dynamics of carriers after excitation. Carriers are first excited to the conduction band (blue arrow), which results in a nonequilibrium distribution of carriers with average energy $\hbar\omega_{pump}/2$ (assuming the Fermi level is at the intersection of the valence and conduction bands). After excitation, they quickly reach a thermal distribution via carrier-carrier scattering within a time scale on the order of 100 fs.[153,178–182] Then, the carriers relax via carrier-phonon scattering (mainly through the emission of optical phonons) on a slower time scale, which is on the order of 1 ps.[179,183] Carrier recombination also occurs, but on a much longer time scale than both of these processes, which eventually results in the initial equilibrium distribution. The equilibrium distribution in this figure is one with no excited carriers.

slower decay of the differential transmission signal. As the carriers emit the phonons, their average energy will decrease, resulting in a decrease in the density of carriers at certain energies. In pump-probe experiments, the probe energy is always large enough such that this is the case. This process occurs on a time scale on the order of several picoseconds. Then, on a much longer time scale, the carriers will recombine, leading to the recovery of the initial, equilibrium distribution of carriers in graphene – in the case of the figure, there are no excited carriers. This process is generally not observed for these types of experiments, because by the time its contribution to the decrease in signal could be noticeable, the carriers have already lost their energy due to phonon cooling and moved out of the probing window, and so they are not visible anymore in the differential transmission signal.

As stated previously, the energy relaxation of carriers is dominated by the emission of optical phonons. Therefore, the exact role optical phonons play in the energy relaxation of carriers has been investigated in detail.[183,184] First, it was observed that with increasing pump fluence (carrier density), the value of the slow decay time constant increases to a constant value at high fluences. It

was proposed that this is due to the hot phonon effect: at high carrier densities, as the carriers relax, they produce a large number of optical phonons. These optical phonons can then give their energy back to electrons, and the result is a slowed energy relaxation of the electron distribution, which at sufficiently high carrier densities is therefore determined by the relaxation of optical phonons into acoustic phonons.[184] After this, real differential transmission measurements were successfully modeled using coupled rate equations between the carriers and optical phonons, accounting for carrier cooling through the emission of optical phonons and calculated optical phonon emission rates, and from this, average optical phonon lifetimes in the range of 2.5 to 2.55 ps were obtained,[183] which agree well with first-principles calculations.[185]

The role of substrate phonons on the relaxation of photoexcited carriers in graphene has been discussed in detail as well.[157,186] Mechanically exfoliated graphene[186] as well as CVD graphene[157] were both suspended and compared with the same type of graphene on glass. Interestingly, different results were found for the two types of graphene. In the case of mechanically exfoliated graphene, differential reflection was measured with 1100 to 1400 nm, 240 fs probe pulses and 830 nm, 180 fs pump pulses and a total fluence of 0.03 J/m^2. It was found that relaxation (i.e. the decay of the differential reflection signal) was nearly the same for suspended samples as compared to samples on glass. This would imply that only intrinsic phonons contribute to the energy relaxation of carriers in graphene. For CVD graphene, differential reflection was measured as well, with 800 nm probe and 400 nm pump pulses and a time resolution of 300 fs. The pump fluence was 0.3 to 5 mJ/cm^2 for suspended and 1.7 to 35 mJ/cm^2 for substrate supported. In this case, however, it was found that the differential reflection signal decays much more quickly for supported graphene than for suspended, and that the bi-exponential decay becomes a single exponential decay. This indicates that in this graphene sample, the substrate surface optical phonon modes do indeed play a large role in the energy relaxation of carriers, providing additional energy relaxation pathways. The fact that the two give such different results may be due to one type of graphene being easier to transfer energy to the substrate than the other. Mechanically exfoliated graphene should be more pure than CVD graphene, i.e. have fewer lattice defects and no residue from the transfer process,

therefore it is possible that these can cause carriers in CVD graphene to more readily transfer their energy to surface optical phonons of a glass substrate as compared to carriers in mechanically exfoliated graphene.

Differential transmission and/or reflection measurements have been performed on a wide variety of samples, and these time scales for the ultrafast response of graphene are typical. For example, a signal with a bi-exponential decay with a short time constant on the order of hundreds of femtoseconds and a long time constant on the order of picoseconds have been observed in reduced graphene oxide in solution,[182] reduced graphene oxide thin films,[187] mechanically exfoliated graphene on Si coated with SiO_2,[181] mechanically exfoliated graphene on SiO_2,[188] mechanically exfoliated graphene on mica,[189] suspended mechanically exfoliated graphene,[186] CVD graphene on quartz,[190,191] CVD graphene on glass,[157] and several other epitaxial graphene samples produced in the same way.[153,183,184,192] The fact that the same temporal behavior is observed in such a wide variety of samples indicates that this is an intrinsic effect of graphene and that substrate effects and differences in growth method play a very minor role if any in the energy relaxation of carriers in graphene.

B.3.2 Coherent control of photocurrents

In materials such as gallium arsenide (GaAs), germanium and graphene, a pair of frequency-related laser pulses can be used to inject a photocurrent by quantum interference. This has been observed GaAs,[193,194] germanium,[195] and by Sun *et al.* in graphene.[196] A fundamental laser pulse ω and its second harmonic laser pulse 2ω are incident on the graphene. Considering both laser pulses separately, they will each cause electrons to make a transition to a higher energy level in the conduction band, leaving holes behind in the valence band. The density of carriers excited with a certain velocity will depend on the transition amplitude, and for a single frequency excitation the density will be the same for all velocities. The second harmonic laser pulse will excite carriers directly across the band gap via one photon absorption, and the fundamental laser pulse will do the same, but also excited carriers to the same energy levels as the second harmonic laser pulse
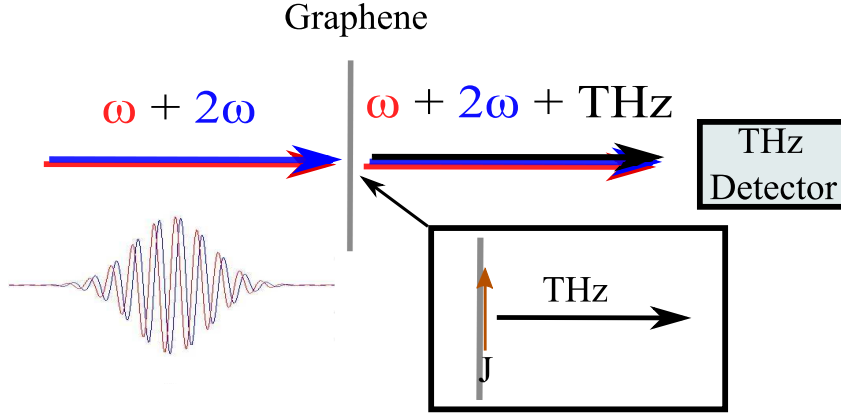
Figure B.5: Experimental configuration for current generated by quantum interference and control (QUIC) and detected by THz emission. A pair of laser pulses, one of frequency ω and the other of second harmonic frequency 2ω are used to generate a current in the graphene. The relative phase between the two pulses controls the magnitude of the current. The current produces a THz electric field, which is detected.

via two-photon absorption. Since one photon absorption of the second harmonic pulse and two-photon absorption of the fundamental pulse excite carriers to the same energy levels, their transition amplitudes will interfere, resulting in a net flow of electrons in certain directions, or a current.

By calculating the transition amplitudes of each transition and finding the overall transition amplitudes when each is present – i.e. considering the interference – one can determine what properties of the excitation electric fields control the current and how they do so. Rioux *et al.*[197] have done the calculations and a summary is as follows. For graphene, the direction of the current depends on the polarization of each beam. Co-circularly polarized beams inject the largest current, with the direction of the current controlled by the phase difference between the two transition amplitudes, while opposite circular polarizations will inject no current. Linear polarizations will inject a current with the magnitude proportional to $\sin(\Delta\phi)$, where $\Delta\phi$ is the phase difference between the two transition amplitudes. The direction of the current depends on the angle between the two polarizations – when the beams are either co-linear or cross polarized, the direction of the current will be in the direction of the 2ω field. The carriers will be instantaneously injected with a nonzero velocity and so this current is considered to be ballistic. After the initial ballistic current, collisions with each other and the lattice will cause the current to be quickly destroyed.

The experimental configuration used by Sun *et al.* for detection of a current produced by quantum interference in graphene is shown in Fig. B.5. Here, a pair of cross-polarized and phase controlled pulses illuminate an epitaxial graphene sample on SiC. The pulses inject a charge current and the magnitude, as discussed above, is controlled by the relative phase of the two pulses. The accelerating charges will produce a THz electric field, which is sent to a detector. The magnitude of the THz electric field increases with increasing current density. A sinusoidal dependence of the THz signal with phase difference between the two pulses was observed, as was the expected dependence on polarization angle between the two fields. However, due to the nature of detecting a THz electric field, no dynamics of the charge current were able to be observed. So, a temporally and spatially resolved study of the dynamics of charge currents in graphene is warranted in the future.

B.3.3 Carrier transport

Of course, from a electronic graphene-based device point of view, carrier transport is equally as important as energy relaxation. However, ultrafast optical studies of carrier transport are rare. The only study which has been performed which actually involves ballistic motion of the carriers in graphene is the quantum interference and control of photocurrents study. A ballistic current was generated and detected, but as just discussed, the current was not temporally or spatially resolved. So, the dynamics of ballistic currents in graphene remain experimentally unexplored.

On the other hand, diffusive transport of carriers in graphene has been studied widely via electrical measurements of mobility or sample conductivity. A sample of mobilities reported for various types of graphene is shown in Table 1. Clearly, the type of graphene plays a large role in the carrier mobility. Devices made of mechanically exfoliated graphene has the highest reported mobilities, followed by epitaxial graphene, then CVD and chemically derived graphene. It is not surprising that devices made of mechanically exfoliated graphene have the highest mobilities, as these come from graphite and so are the purest type of graphene – they have the fewest lattice defects and no other compounds which may be left over from the fabrication or transfer process.

Type of graphene	Reported mobility (cm^2/V·s)	Year
Exfoliated graphene	7,000	2007 [198]
	10,000	2004 [132]
	13,500	2008 [199]
	15,000	2008 [200]
Epitaxial graphene	535	2007 [164]
	1,200	2007 [161]
	1,500	2010 [137]
	27,000	2006 [163]
	3,000	2011 [201]
CVD graphene	3,750	2009 [146]
Chemically derived graphene	0.2	2008 [202]
	281	2010 [145]

Table B.1: Measured mobilities for various graphene samples.

It is also not surprising that chemically derived graphene has the lowest mobilities, as this type of graphene is expected to have the largest number lattice defects, and also have more grain boundaries.

B.3.4   Differential transmission as a probe of Fermi level

In addition to studying the dynamics of carriers alone, a differential transmission signal can be used as a probe of the Fermi level of a graphene layer. This has been specifically demonstrated in epitaxial graphene grown on SiC.[165,203] For a graphene sample where the Fermi level lies at the Dirac point, any pump-probe experiment will always cause a positive differential transmission (or a negative differential reflection). The pump will excite carriers and after thermalization the carrier density at all energies will have increased, which leads to an increase in transmission (or decrease in reflection) of the probe. If, however, the Fermi level lies above the Dirac point – i.e. there are some carriers already present in graphene – for certain probing energies the differential transmission may become negative at some time delays. This can occur if the pump excites carriers from the Fermi level and below higher into the band and then the probe is able to excite carriers

119

into those states which are now open because of the pump – i.e. intraband absorption by the pump will lead to an increase in absorption of the probe. This will result in a negative differential transmission.

It has been observed that when the probing energy approaches twice the Fermi energy for a particular layer, the differential transmission will become strongly negative at a fixed time delay.[165,203] For probing energies slightly above twice the Fermi level, the differential transmission will become strongly positive. This indicates that differential transmission measurements may be used as a different powerful tool – they allow the direct measurement of the doping density of a layer of graphene. However, a flip in sign of differential transmission signal can be caused by several other things, such as lattice heating effects, and has been observed for probing energies that are inconsistent with the Fermi energy of a graphene layer.[204]

Appendix C

Review of single-walled carbon nanotubes

Single-walled carbon nanotubes (SWNTs) have attracted consideration attention for the last two decades. A SWNT can be viewed as a rolled-up graphene sheet. Depending on the tube diameter and chirality, a SWNT can be semiconducting or metallic, with a wide range of energy gaps. Because of its nanometer scale diameter and micrometer scale length along the tube, it provides an ideal platform to study one-dimensional (1D) physics. Its unique mechanical, electrical and optical properties have made it an attractive candidate in many applications, for example high-strength composition materials, nanoelectonics, photovoltaics, and photodetectors.

Owing to the unusually strong Coulomb interactions in these 1D materials, the interaction between electrons in SWNTs and light is dominated by excitons. Hence, understanding the excitonic dynamics in SWNTs is important for many optoelectronic applications. Photoemission[205,206] and transient absorption[207–215] measurements on samples of SWNT bundles, where semiconducting and metallic SWNTs entangled together, have shown ultrafast excitonic dynamics characterized by a energy relaxation time of about 0.1 ps and an exciton lifetime of 1 ps. Other transient absorption studies on samples of insolating or individual SWNTs revealed that these fast dynamics are induced by fast transfer of excitons from semiconducting to metallic tubes. When such channels are eliminated in isolated tubes, the exciton energy relaxation can take several picoseconds[216–224], and the exciton lifetimes of several 10 ps[217,218,220,221,224] to several 100 ps[216,219,223] have been

measured. Time-resolved photoluminescence measurements have shown the decay times of several 10 ps.[225–231] The lifetime is dominated by nonradiative recombination. Several experiments have concluded that exciton-exciton annihilation is the major nonradiative recombination mechanism.[232–234] Other aspects of excitonic dynamics have also been studied, including exciton dephasing,[235] exciton-phonon interactions,[236–239] multiple exciton generation,[240,241] intraexciton transition,[242] and excitonic nonliearities.[243–247]

In contrast to these extensive studies in time and energy domains, the excitonic dynamics in real space, i.e. exciton diffusion along the tubes, has been less studied. Since the size of excitons (about 2 nm) is much smaller than the length of the SWNTs, exciton diffusion plays an essential role in excitation energy transfer in many SWNT-based optoelectronic applications. From a fundamental point of view, studies of exciton diffusion can provide valuable information on microscopic interactions between excitons and their environment. For example, exciton diffusion is an important aspect in understand exciton-exciton annihilation and long-term delay.

Direct measurements of the exciton diffusion are rather challenging, since electric techniques that are typically used for transport studies are less effective on excitons that are electrically neutral. Recently, several attempts have been made to measure the exciton diffusion coefficient in SWNT samples. However, mainly due to the complexity of the procedures used to deduce the diffusion coefficient, the results differ by orders of magnitude. Korovyanko *et al* observed a polarization memory effect in transient absorption measurements, and by attributing the depolarization to the exciton diffusion in curved SWNTs, they deduced a diffusion coefficient of 120 cm^2/s.[211] By measuring exciton lifetime as a function of exciton density, one can determine the exciton-exciton annihilation rate, which can be modeled to deduce the diffusion coefficient.[232,248] However, measurements used transient absorption technique and time-resolved PL technique have yielded rather different results: the former found very small diffusion coefficients of 0.1 cm^2/s[249] to 4 cm^2/s;[250] while the latter gave a value of about 90 cm^2/s.[251] Other transient absorption measurements were interpreted by considering exciton diffusion to quenching sites like defects or tube ends, and resulted a diffusion coefficient of about 10 cm^2/s.[252–254]

In addition to these ultrafast studies in the time domain, stepwise quenching of exciton luminescence by single-molecule reactions can be used to deduce the exciton diffusion lengths of 60 nm[255] to 200 nm,[256] and simulation of near-field microscopy measurements of PL quenching at the tube ends gave a diffusion length of about 100-200 nm.[257,258] Furthermore, by modeling the power dependence of PL with different tube lengths as a one-dimensional diffusion, a diffusion length of 610 nm.[259] Since in these studies the exciton lifetime was not measured, one has to assume a certain lifetime in order to estimate the diffusion coefficient. This and the rather large range of the diffusion lengths measured has resulted in a large range of estimated diffusion coefficients of 0.4 cm^2/s,[255] 2.5-10 cm^2/s,[257] and 44 cm^2/s.[259] The discrepancy in these studies could be partially attributed to sample variations, since the exciton transport can be influenced by the environment of the SWNTs. However, the more important issue is the lack of a model-independent technique to directly measure the diffusion coefficient.

Appendix D

Calculation of laser fluence and carrier density

D.1 Fluence of a Gaussian laser beam

The fluence of a laser indicates the energy per unit area that a laser pulse delivers to a certain location. In the experiments discussed in this dissertation, it is important to know the peak pump laser fluence that is being delivered when focusing a laser beam to a small spot on a sample, so that the density of photoexcited carriers can be calculated

Assume the laser produces Gaussian laser pulses at a frequency of f_{rep} (measured in Hz), which is known as the repetition rate of the laser. In order to find the peak fluence of the laser pulse, we must first find the energy delivered by each laser pulse, E_{pulse}. To do this, we measure the power of the laser, P, with a power meter, which reports the time averaged power of a laser. Then, the energy delivered per pulse is:

$$E_{\text{pulse}} = \frac{P}{f_{rep}}. \tag{D.1}$$

The peak laser fluence is usually of interest, when focusing the beam to a small spot with a lens. During pump-probe experiments, rather than measuring the laser spot size directly, it is more convenient to measure the full width at half maximum (FWHM) of the differential transmission profile,

w_{DT}. Since this comes from both pump and probe beams, this spatial profile that is measured is actually a convolution of the pump and probe laser spots. Usually, the spots are close to the same size, so it is safe to assume that the width of the pump, w_0, is given by:

$$w_0 = \frac{w_{DT}}{\sqrt{2}}. \tag{D.2}$$

To find the peak laser fluence, recall that the beam is Gaussian. For a Gaussian beam, the intensity profile of the beam will be Gaussian in space:

$$I(r) = I_0 e^{-2r^2/w^2}, \tag{D.3}$$

where I_0 is the peak intensity of the beam, r is the distance from the center of the beam (i.e. the beam radius), and w is the radius at which the beam intensity drops to $1/e^2$ of I_0. The intensity of the beam describes the power per unit area of the beam, while the fluence describes the energy per unit area of the beam. Therefore, the fluence can be described in the same way as the intensity:

$$F(r) = F_{peak} e^{-2r^2/w^2}, \tag{D.4}$$

where F_{peak} is the peak fluence of the pulse. By definition, the energy of each pulse can be found by integrating the fluence over all space:

$$
\begin{aligned}
E_{pulse} &= \int F(r)\,da \\
&= \int_0^\infty F_{peak} e^{-2r^2/w^2} 2\pi r\,dr \\
&= F_{peak} 2\pi \frac{1}{2}\left(\frac{2}{w^2}\right)^{-1} \\
&= F_{peak}\frac{\pi w^2}{2},
\end{aligned}
\tag{D.5}
$$

and therefore

$$F_{\text{peak}} = \frac{2E_{\text{pulse}}}{\pi w^2}. \tag{D.6}$$

Now, since the FWHM of the beam, w_0, is the quantity that is actually measured, this must be related to w:

$$
\begin{aligned}
I(w_0) &= 0.5I_0 \\
&= I_0 e^{-2(w_0/2)^2/w^2}, \tag{D.7}
\end{aligned}
$$

which means that

$$w = \frac{w_0}{\sqrt{2\ln 2}}. \tag{D.8}$$

Finally, these measured quantities can be related to the peak fluence for each laser pulse:

$$F_{\text{peak}} = \frac{8\ln 2}{\pi} \frac{P}{f_{rep} w_{\text{DT}}^2}. \tag{D.9}$$

D.2   Carrier density

The fluence, as calculated in the previous section, indicates the peak energy delivered by the laser to the sample per unit area. This must then be used to calculate the density of carriers excited in the sample. Each photon has energy

$$E_{ph} = \frac{hc}{\lambda} = h\nu = \hbar\omega, \tag{D.10}$$

where $\hbar$ is Planck's constant (6.626×10^{-34} J$\cdot$s or 4.135 eV$\cdot$s), c is the speed of light in a vacuum (3×10^8 m/s), λ is the wavelength of the photon, ν is the frequency of the photon, $\hbar$ is $h/2\pi$, and ω is the angular frequency of each photon. Therefore, if a beam of peak fluence F_{peak} is incident on the sample, $F_{\text{peak}}/(h\nu)$ will be the peak number of photons incident on the sample.

Now, assume the absorption coefficient of the sample is α, where α is defined as

$$I_t = I_0 e^{-\alpha L}. \tag{D.11}$$

This means that if you have light of intensity I_0 incident on a sample of thickness L, with the sample's absorption coefficient being α, the intensity of light that comes out of the sample will be I_t. Also, assume that each photon that is absorbed creates one excited carrier in the sample. Then, the peak number of carriers excited per unit volume, n_{3D}, as a function of the depth into the sample, z, will be

$$n_{3D}(z) = \alpha \frac{F_{\text{peak}}}{h\nu} e^{-\alpha z}. \tag{D.12}$$

Note that this is defining $z = 0$ as the front of the sample, and $z = L$ as the back of the sample. The two dimensional carrier density, i.e. the number of photoexcited carriers per unit area, can be calculated by integrating this equation over some depth. For example, in graphene, we can define each graphene layer as having an effective thickness of 0.33 nm, i.e. the spacing between layers in bulk graphite. For the layer that begins at depth a, and ends at depth b ($b - a = 0.33$ nm), the areal carrier density, of that layer only, will be:

$$n_{2D} = \int_a^b n_{3D}(z)\,dz = \frac{F_{\text{peak}}}{h\nu}(e^{-\alpha a} - e^{-\alpha b}). \tag{D.13}$$

References

[1] B. A. Ruzicka, L. K. Werake, H. Zhao, S. Wang, and K. P. Loh, "Femtosecond pump-probe studies of reduced graphene oxide thin films," Appl. Phys. Lett. **96**, 173106 (2010).

[2] B. A. Ruzicka, N. Kumar, S. Wang, K. P. Loh, and H. Zhao, "Two-probe study of hot carriers in reduced graphene oxide," J. Appl. Phys. **109**, 084322 (2011).

[3] B. A. Ruzicka, L. K. Werake, H. Samassekou, and H. Zhao, "Ambipolar diffusion of photoexcited carriers in bulk GaAs," Appl. Phys. Lett. **97**, 262119 (2010).

[4] B. A. Ruzicka, S. Wang, L. K. Werake, B. Weintrub, K. P. Loh, and H. Zhao, "Hot carrier diffusion in graphene," Phys. Rev. B **82**, 195414 (2010).

[5] B. A. Ruzicka and H. Zhao, "Optical studies of ballistic currents in semiconductors," J. Opt. Soc. Am. B **29**, A43 (2012).

[6] B. A. Ruzicka, K. Higley, L. K. Werake, and H. Zhao, "All-optical generation and detection of subpicosecond ac spin-current pulses in GaAs," Phys. Rev. B **78**, 045314 (2008).

[7] B. A. Ruzicka and H. Zhao, "Power dependence of pure spin current injection by quantum interference," Phys. Rev. B **79**, 155204 (2009).

[8] B. A. Ruzicka, L. K. Werake, J. B. Khurgin, E. Y. Sherman, and H. Zhao, "Second-harmonic generation induced by electric currents in gaas," Phys. Rev. Lett. **108**, 077403 (2012).

[9] D. A. Neamen, *Semiconductor physics and devices* (McGraw-Hill, Boston, 2002).

[10] Intel, "Intel 22nm technology," (2011).

[11] J. Shah, *Ultrafast spectroscopy of semiconductors and semiconductor nanostructures* (Springer, Germany, 1996).

[12] J. Hegarty, L. Goldner, and M. D. Sturge, "Localized and delocalized two-dimensional excitons in GaAs-AlGaAs multiple-quantum-well structures," Phys. Rev. B **30**, 7346 (1984).

[13] K. Hattori, T. Mori, H. Okamoto, and Y. Hamakawa, "Carrier transport property in the amorphous silicon/amorphous silicon carbide multilayer studied by the transient grating technique," Appl. Phys. Lett. **51**, 1259 (1987).

[14] H. Schwab, K.-H. Pantke, J. M. Hvam, and C. Klingshirn, "Measurements of exciton diffusion by degenerate four-wave mixing in CdSSe," Phys. Rev. B **46**, 7528 (1992).

[15] J. Erland, B. S. Razbirin, K.-H. Pantke, V. G. Lyssenko, and J. M. Hvam, "Exciton diffusion in CdSe," Phys. Rev. B **47**, 3582 (1993).

[16] V. Mizeikis, V. G. Lyssenko, J. Erland, and J. M. Hvam, "Excitonic optical nonlinearities and transport in the layered compound semiconductor GaSe," Phys. Rev. B **51**, 16651 (1995).

[17] A. C. Schaefer, J. Erland, and D. G. Steel, "Nondiffusive excitonic transport in GaAs and the effects of momentum scattering," Phys. Rev. B **54**, 11046 (1996).

[18] L.-L. Chao, G. S. Gargill-III, E. Snoeks, T. Marshall, J. Petruzzello, and M. Pashley, "Diffusion lengths of excited carriers in CdZnSe quantum wells," Appl. Phys. Lett. **74**, 741 (1999).

[19] F. P. Logue, D. T. Fewer, S. J. Hewlett, J. F. Heffernan, C. Jordan, P. Rees, J. F. Donegan, E. M. McCabe, J. Hegarty, S. Taniguchi, T. Hino, K. Nakano, and A. Ishibashi, "Optical measurement of the ambipolar diffusion length in a ZnCdSe-ZnSe single quantum well," J. Appl. Phys. **81**, 536 (1997).

[20] A. Vertikov, I. Ozden, and A. Nurmikko, "Investigation of excess carrier diffusion in nitride semiconductors with near-field optical microscopy," Appl. Phys. Lett. **74**, 850 (1999).

[21] V. Malyarchuk, J. W. Tomm, V. Talalaev, C. Lienau, F. Rinner, and M. Baeumler, "Nanoscopic measurements of surface recombination velocity and diffusion length in a semiconductor quantum well," Appl. Phys. Lett. **81**, 346 (2002).

[22] H. Hillmer, A. Forchel, and C. W. Tu, "Enhancement of electron-hole pair mobilities in thin GaAs/AlGaAs quantum wells," Phys. Rev. B **45**, 1240 (1992).

[23] H. Akiyama, T. Matsusue, and H. Sakaki, "Carrier scattering and excitonic effects on electron-hole-pair diffusion in nondoped and p-type-modulation-doped GaAs/AlGaAs quantum-well structures," Phys. Rev. B **49**, 14523 (1994).

[24] K. S. Novoselov, A. K. Geim, S. V. Morozov, D. Jiang, Y. Zhang, S. V. Dubonos, I. V. Grigorieva, and A. A. Firsov, "Electric field effect in atomically thin carbon films," Science **306**, 666 (2004).

[25] M. Orlita, C. Faugeras, P. Plochocka, P. Neugebauer, G. Martinez, D. K. Maude, A. L. Barra, M. Sprinkle, C. Berger, W. A. de Heer, and M. Potemski, "Approaching the Dirac point in high-mobility multilayer epitaxial graphene," Phys. Rev. Lett. **101**, 267601 (2008).

[26] C. Lee, X. Wei, J. W. Kysar, and J. Hone, "Measurement of the elastic properties and intrinsic strength of monolayer graphene," Science **321**, 385 (2008).

[27] A. A. Balandin, S. Ghosh, W. Bao, I. Calizo, D. Teweldebrhan, F. Miao, and C. N. Lau, "Superior thermal conductivity of single-layer graphene," Nano Lett. **8**, 902 (2008).

[28] C. Berger, Z. Song, X. Li, X. Wu, N. Brown, C. Naud, D. Mayou, T. Li, J. Hass, A. N. Marchenkov, E. H. Conrad, P. N. First, and W. A. de Heer, "Electronic confinement and coherence in patterned epitaxial graphene," Science **312**, 1191 (2006).

[29] A. Reina, X. T. Jia, J. Ho, D. Nezich, H. B. Son, V. Bulovic, M. S. Dresselhaus, and J. Kong, "Large area, few-layer graphene films on arbitrary substrates by chemical vapor deposition," Nano Lett. **9**, 30 (2009).

[30] S. A. Wang, P. K. Ang, Z. Q. Wang, A. L. L. Tang, J. T. L. Thong, and K. P. Loh, "High mobility, printable, and solution-processed graphene electronics," Nano Lett. **10**, 92 (2010).

[31] J. M. Dawlaty, S. Shivaraman, J. Strait, P. George, M. Chandrashekhar, F. Rana, M. G. Spencer, D. Veksler, and Y. Q. Chen, "Measurement of the optical absorption spectra of epitaxial graphene from terahertz to visible," Appl. Phys. Lett. **93**, 131905 (2008).

[32] S. Das Sarma, S. Adam, E. H. Hwang, and E. Rossi, "Electronic transport in two-dimensional graphene," Rev. Mod. Phys. **83**, 407 (2011).

[33] R. A. Soref, "Silicon-based optoelectronics," Proc. of the IEEE **81**, 1687 (1993).

[34] F. Wang, G. Dukovic, L. E. Brus, and T. F. Heinz, "The optical resonances in carbon nanotubes arise from excitons," Science **308**, 838 (2005).

[35] S. Ren, M. Bernardi, R. R. Lunt, V. Bulovic, J. C. Grossman, and S. Gradecak, "Toward efficient carbon nanotube/p3ht solar cells: Layer morphology, electrical and optical properties," Nano Lett. **11**, 5316 (2011).

[36] R. H. Baughman, A. A. Zakhidov, and W. A. de Heer, "Carbon nanotubes—the route toward applications," Science **297**, 787 (2002).

[37] M. Fox, *Optical properties of solids* (Oxford University Press, 2010), 2nd ed.

[38] M. J. Stevens, "Optical injection and coherent control of ballistic spin currents, carrier density, and carrier spin in semiconductors," Ph.D. thesis, The University of Iowa (2004).

[39] T. Dekorsy, T. Pfeifer, W. Kutt, and H. Kurz, "Subpicosecond carrier transport in gaas surface-space-charge fields," Phys. Rev. B **47**, 3842 (1993).

[40] P. Langot, N. D. Fatti, D. Christofilos, R. Tommasi, and F. Vallee, "Femtosecond investigation of the hot-phonon effect in gaas at room temperature," Phys. Rev. B **54**, 14487 (1996).

[41] P. Langot, R. Tommasi, and F. Vallee, "Nonequilibrium hole relaxation dynamics in an intrinsic semiconductor," Phys. Rev. B **54**, 1775 (1996).

[42] S. M. Goodnick and P. Lugli, "Influence of electron-hole scattering on subpicosecond carrier relaxation in AlGaAs/GaAs quantum wells," Phys. Rev. B **38**, 10135 (1988).

[43] J. M. Dawlaty, S. Shivaraman, M. Chandrashekhar, F. Rana, and M. G. Spencer, "Measurement of ultrafast carrier dynamics in epitaxial graphene," Appl. Phys. Lett. **92**, 042116 (2008).

[44] H. Choi, F. Borondics, D. A. Siegel, S. Y. Zhou, M. C. Martin, A. Lanzara, and R. A. Kaindl, "Broadband electromagnetic response and ultrafast dynamics of few-layer epitaxial graphene," Appl. Phys. Lett. **94**, 172102 (2009).

[45] D. Sun, Z. K. Wu, C. Divin, X. B. Li, C. Berger, W. A. de Heer, P. N. First, and T. B. Norris, "Ultrafast relaxation of excited Dirac fermions in epitaxial graphene using optical differential transmission spectroscopy," Phys. Rev. Lett. **101**, 157402 (2008).

[46] Y. M. Lin, C. Dimitrakopoulos, K. A. Jenkins, D. B. Farmer, H. Y. Chiu, A. Grill, and P. Avouris, "100-GHz transistors from wafer-scale epitaxial graphene," Science **327**, 662 (2010).

[47] M. D. Stoller, S. Park, Y. Zhu, J. An, and R. S. Ruoff, "Graphene-based ultracapacitors," Nano Lett. **8**, 3498 (2008).

[48] X. Wang, L. J. Zhi, and K. Mullen, "Transparent, conductive graphene electrodes for dye-sensitized solar cells," Nano Lett. **8**, 323 (2008).

[49] W. S. Hummers and R. E. Offeman, "Preparation of graphitic oxide," J. Am. Chem. Soc. **80**, 1339 (1958).

[50] L. Huang, G. V. Hartland, L. Q. Chu, Luxmi, R. M. Feenstra, C. Lian, K. Tahy, and H. Xing, "Ultrafast transient absorption microscopy studies of carrier dynamics in epitaxial graphene," Nano Lett. **10**, 1308 (2010).

[51] H. Wang, J. H. Strait, P. A. George, S. Shivaraman, V. B. Shields, M. Chandrashekhar, J. Hwang, F. Rana, M. G. Spencer, C. S. Ruiz-Vargas, and J. Park, "Ultrafast relaxation dynamics of hot optical phonons in graphene," Appl. Phys. Lett. **96**, 081917 (2010).

[52] P. R. Wallace, "The band theory of graphite," Phys. Rev. **71**, 622 (1947).

[53] S. Berciaud, M. Y. Han, K. F. Mak, L. E. Brus, P. Kim, and T. F. Heinz, "Electron and optical phonon temperatures in electrically biased graphene," Phys. Rev. Lett. **104**, 227401 (2010).

[54] W. K. Tse and S. Das Sarma, "Phonon-induced many-body renormalization of the electronic properties of graphene," Phys. Rev. Lett. **99**, 236802 (2007).

[55] W. K. Tse, E. H. Hwang, and S. Das Sarma, "Ballistic hot electron transport in graphene," Appl. Phys. Lett. **93**, 023128 (2008).

[56] K. Y. Wang, W. P. Huang, H. H. Cheng, G. Sun, R. A. Soref, R. J. Nicholas, and Y. W. Suen, "Observation of type-I and type-II excitons in strained Si/SiGe quantum-well structures," Appl. Phys. Lett. **91**, 072108 (2007).

[57] H. Zhao, M. Mower, and G. Vignale, "Ambipolar spin diffusion and D'yakonov-Perel' spin relaxation in GaAs quantum wells," Phys. Rev. B **79**, 115321 (2009).

[58] H. Zhao, S. Moehl, and H. Kalt, "Coherence length of excitons in semiconductor quantum wells," Phys. Rev. Lett. **89**, 097401 (2002).

[59] H. Zhao, S. Moehl, S. Wachter, and H. Kalt, "Hot exciton transport in ZnSe quantum wells," Appl. Phys. Lett. **80**, 1391 (2002).

[60] H. Zhao, B. Dal Don, S. Moehl, H. Kalt, K. Ohkawa, and D. Hommel, "Spatio-temporal dynamics of quantum-well excitons," Phys. Rev. B **67**, 035306 (2003).

[61] I. Žutić, J. Fabian, and S. Das Sarma, "Spintronics: Fundamentals and applications," Rev. Mod. Phys. **76**, 323 (2004).

[62] H. Zhao, E. J. Loren, A. L. Smirl, and H. M. van Driel, "Dynamics of charge current injected in GaAs by quantum interference," J. Appl. Phys. **103**, 053510 (2008).

[63] L. K. Werake and H. Zhao, "Observation of second-harmonic generation induced by pure spin currents," Nat. Phys. **6**, 875 (2010).

[64] L. M. Smith, D. R. Wake, J. P. Wolfe, D. Levi, M. V. Klein, J. Klem, T. Henderson, and H. Morkoç, "Picosecond imaging of photoexcited carriers in quantum wells: Anomalous lateral confinement at high densities," Phys. Rev. B **38**, 5788 (1988).

[65] L. M. Smith, J. S. Preston, J. P. Wolfe, D. R. Wake, J. Klem, T. Henderson, and H. Morkoç, "Phonon-wind-driven transport of photoexcited carriers in a semiconductor quantum well," Phys. Rev. B **39**, 1862 (1989).

[66] H. W. Yoon, D. R. Wake, J. P. Wolfe, and H. Morkoç, "In-plane transport of photoexcited carriers in GaAs quantum wells," Phys. Rev. B **46**, 13461 (1992).

[67] M. Achermann, B. A. Nechay, F. Morier-Genoud, A. Schertel, U. Siegner, and U. Keller, "Direct experimental observation of different diffusive transport regimes in semiconductor nanostructures," Phys. Rev. B **60**, 2101 (1999).

[68] P. Vledder, A. V. Akimov, J. I. Dijkhuis, J. Kusano, Y. Aoyagi, and T. Sugano, "Transport of superradiant excitons in GaAs single quantum wells," Phys. Rev. B **56**, 15282 (1997).

[69] M. Yoshita, M. Baba, S. Koshiba, H. Sakaki, and H. Akiyama, "Solid-immersion photoluminescence microscopy of carrier diffusion and drift in facet-growth GaAs quantum wells," Appl. Phys. Lett. **73**, 2965 (1998).

[70] G. D. Gilliland, M. S. Petrovic, H. P. Hjalmarson, D. J. Wolford, G. A. Northrop, T. F. Kuech, L. M. Smith, and J. A. Bradley, "Time-dependent heterointerfacial band bending

and quasi-two-dimensional excitonic transport in GaAs structures," Phys. Rev. B **58**, 4728 (1998).

[71] K. Fujiwara, U. Jahn, and H. T. Grahn, "Cathodoluminescence spectroscopy of ambipolar diffusion in (Al,Ga)As barriers and capture of nonequilibrium carriers in GaAs quantum wells," Appl. Phys. Lett. **93**, 103504 (2008).

[72] A. L. Mears and R. A. Stradling, "Cyclotron resonance and Hall measurements on the hole carriers in GaAs," J. Phys. C **4**, L22 (1971).

[73] J. S. Blakemore, "Semiconducting and other major properties of gallium arsenide," J. Appl. Phys. **53**, R123 (1982).

[74] G. E. Stillman, C. M. Wolfe, and J. O. Dimmock, "Hall coefficient factor for polar mode scattering in n-type GaAs," J. Phys. Chem. Solids **31**, 1199 (1970).

[75] G. Eda, G. Fanchini, and M. Chhowalla, "Large-area ultrathin films of reduced graphene oxide as a transparent and flexible electronic material," Nat. Nanotechnol. **3**, 270 (2008).

[76] K. S. Kim, Y. Zhao, H. Jang, S. Y. Lee, J. M. Kim, K. S. Kim, J. H. Ahn, P. Kim, J. Y. Choi, and B. H. Hong, "Large-scale pattern growth of graphene films for stretchable transparent electrodes," Nature **457**, 706 (2009).

[77] H. Huang, W. Chen, S. Chen, and A. T. S. Wee, "Bottom-up growth of epitaxial graphene on 6H-SiC(0001)," ACS Nano **2**, 2513 (2008).

[78] W. Chen, K. P. Loh, H. Xu, and A. T. S. Wee, "Nanoparticle dispersion on reconstructed carbon nanomeshes," Langmuir **20**, 10779 (2004).

[79] R. Atanasov, A. Haché, J. L. P. Hughes, H. M. van Driel, and J. E. Sipe, "Coherent control of photocurrent generation in bulk semiconductors," Phys. Rev. Lett. **76**, 1703 (1996).

[80] R. D. R. Bhat and J. E. Sipe, "Optically injected spin currents in semiconductors," Phys. Rev. Lett. **85**, 5432 (2000).

[81] A. Haché, Y. Kostoulas, R. Atanasov, J. L. P. Hughes, J. E. Sipe, and H. M. van Driel, "Observation of coherently controlled photocurrent in unbiased, bulk GaAs," Phys. Rev. Lett. **78**, 306 (1997).

[82] E. Loren, H. Zhao, and A. L. Smirl, "All-optical injection and detection of ballistic charge currents in germanium," J. Appl. Phys. **108**, 083111 (2010).

[83] M. J. Stevens, A. L. Smirl, R. D. R. Bhat, A. Najmaie, J. E. Sipe, and H. M. van Driel, "Quantum interference control of ballistic pure spin currents in semiconductors," Phys. Rev. Lett. **90**, 136603 (2003).

[84] H. Zhao, A. L. Smirl, and H. M. van Driel, "Temporally and spatially resolved ballistic pure spin transport," Phys. Rev. B **75**, 075305 (2007).

[85] M. J. Stevens, A. L. Smirl, R. D. R. Bhat, J. E. Sipe, and H. M. van Driel, "Coherent control of an optically injected ballistic spin-polarized current in bulk GaAs," J. Appl. Phys. **91**, 4382 (2002).

[86] J. B. Khurgin, "Current induced second harmonic generation in semiconductors," Appl. Phys. Lett. **67**, 1113 (1995).

[87] R. Shankar, *Principles of Quantum Mechanics* (Springer, 1994).

[88] R. D. R. Bhat and J. E. Sipe, "Calculations of two-color interband optical injection and control of carrier population, spin, current, and spin current in bulk semiconductors," eprint arXiv:cond-mat/0601277 (2005).

[89] E. Hecht, *Optics* (Pearson, 2002).

[90] S. A. Wolf, D. D. Awschalom, R. A. Buhrman, J. M. Daughton, S. von Molnar, M. L. Roukes, A. Y. Chtchelkanova, and D. M. Treger, "Spintronics: A spin-based electronics vision for the future," Science **294**, 1488 (2001).

[91] Y. K. Kato, R. C. Myers, A. C. Gossard, and D. D. Awschalom, "Observation of the spin Hall effect in semiconductors," Science **306**, 1910 (2004).

[92] J. Wunderlich, B. Kaestner, J. Sinova, and T. Jungwirth, "Experimental observation of the spin-Hall effect in a two-dimensional spin-orbit coupled semiconductor system," Phys. Rev. Lett. **94**, 047204 (2005).

[93] H. Zhao, E. J. Loren, H. M. van Driel, and A. L. Smirl, "Coherence control of Hall charge and spin currents," Phys. Rev. Lett. **96**, 246601 (2006).

[94] J. Hübner, W. W. Rühle, M. Klude, D. Hommel, R. D. R. Bhat, J. E. Sipe, and H. M. van Driel, "Direct observation of optically injected spin-polarized currents in semiconductors," Phys. Rev. Lett. **90**, 216601 (2003).

[95] D. Hägele, M. Oestreich, W. W. Rühle, N. Nestle, and K. Eberl, "Spin transport in GaAs," Appl. Phys. Lett. **73**, 1580 (1998).

[96] J. M. Kikkawa and D. D. Awschalom, "Lateral drag of spin coherence in gallium arsenide," Nature **397**, 139 (1999).

[97] K. Tsukagoshi, B. W. Alphenaar, and H. Ago, "Coherent transport of electron spin in a ferromagnetically contacted carbon nanotube," Nature **401**, 572 (1999).

[98] S. A. Crooker, M. Furis, X. Lou, C. Adelmann, D. L. Smith, C. J. Palmstrom, and P. A. Crowell, "Imaging spin transport in lateral ferromagnet/semiconductor structures," Science **309**, 2191 (2005).

[99] I. Appelbaum, B. Q. Huang, and D. J. Monsma, "Electronic measurement and control of spin transport in silicon," Nature **447**, 295 (2007).

[100] S. D. Ganichev, H. Ketterl, W. Prettl, E. L. Ivchenko, and L. E. Vorobjev, "Circular photo-galvanic effect induced by monopolar spin orientation in p-GaAs/AlGaAs multiple-quantum wells," Appl. Phys. Lett. **77**, 3146 (2000).

[101] S. D. Ganichev, V. V. Bel'kov, P. Schneider, E. L. Ivchenko, S. A. Tarasenko, W. Wegscheider, D. Weiss, D. Schuh, E. V. Beregulin, and W. Prettl, "Resonant inversion of the circular photogalvanic effect in n-doped quantum wells," Phys. Rev. B **68**, 035319 (2003).

[102] H. Diehl, V. A. Shalygin, V. V. Bel'kov, C. Hoffmann, S. N. Danilov, T. Herrle, S. A. Tarasenko, D. Schuh, C. Gerl, W. Wegscheider, W. Prettl, and S. D. Ganichev, "Spin photocurrents in (110)-grown quantum well structures," New J. Phys. **9**, 349 (2007).

[103] S. D. Ganichev, E. L. Ivchenko, S. N. Danilov, J. Eroms, W. Wegscheider, D. Weiss, and W. Prettl, "Conversion of spin into directed electric current in quantum wells," Phys. Rev. Lett. **86**, 4358 (2001).

[104] C. M. Wei, K. S. Cho, Y. F. Chen, Y. H. Peng, C. W. Chiu, and C. H. Kuan, "Photogalvanic effects for interband transition in p-$Si_{0.5}Ge_{0.5}$/Si multiple quantum wells," Appl. Phys. Lett. **91**, 252102 (2007).

[105] K. S. Cho, C. T. Liang, Y. F. Chen, Y. Q. Tang, and B. Shen, "Spin-dependent photocurrent induced by rashba-type spin splitting in $Al_{0.25}Ga_{0.75}$N/GaN heterostructures," Phys. Rev. B **75**, 085327 (2007).

[106] K. S. Cho, Y. F. Chen, Y. Q. Tang, and B. Shen, "Photogalvanic effects for interband absorption in AlGaN/GaN superlattices," Appl. Phys. Lett. **90**, 041909 (2007).

[107] X. W. He, B. Shen, Y. Q. Tang, N. Tang, C. M. Yin, F. J. Xu, Z. J. Yang, G. Y. Zhang, Y. H. Chen, C. G. Tang, and Z. G. Wang, "Circular photogalvanic effect of the two-dimensional electron gas in $Al_X Ga_{1-X}$N/GaN heterostructures under uniaxial strain," Appl. Phys. Lett. **91**, 071912 (2007).

[108] Y. Q. Tang, B. Shen, X. W. He, K. Han, N. Tang, W. H. Chen, Z. J. Yang, G. Y. Zhang, Y. H. Chen, C. G. Tang, Z. G. Wang, K. S. Cho, and Y. F. Chen, "Room-temperature spin-oriented photocurrent under near-infrared irradiation and comparison of optical means with

shubnikov de-haas measurements in $Al_X Ga_{1-X}N$/GaN heterostructures," Appl. Phys. Lett. **91**, 071920 (2007).

[109] F. Meier and B. P. Zakharchenya, *Optical orientation*, vol. 8 of *Modern Problems in Condensed Matter Sciences* (North-Holland, Amsterdam, 1984).

[110] A. Najmaie, R. D. R. Bhat, and J. E. Sipe, "All-optical injection and control of spin and electrical currents in quantum wells," Phys. Rev. B **68**, 165348 (2003).

[111] H. T. Duc, T. Meier, and S. W. Koch, "Microscopic analysis of the coherent optical generation and the decay of charge and spin currents in semiconductor heterostructures," Phys. Rev. Lett. **95**, 086606 (2005).

[112] H. T. Duc, Q. T. Vu, T. Meier, H. Haug, and S. W. Koch, "Temporal decay of coherently optically injected charge and spin currents due to carrier-LO-phonon and carrier-carrier scattering," Phys. Rev. B **74**, 165328 (2006).

[113] D. J. Hilton and C. L. Tang, "Optical orientation and femtosecond relaxation of spin-polarized holes in GaAs," Phys. Rev. Lett. **89**, 146601 (2002).

[114] M. Born and E. Wolf, *Principle of Optics* (Cambridge University Press, Cambridge,UK, 1999), seventh ed.

[115] J. Wang, B. F. Zhu, and R. B. Liu, "Second-order nonlinear optical effects of spin currents," Phys. Rev. Lett. **104**, 256601 (2010).

[116] D. J. Griffiths, *Introduction to electrodynamics* (Prentice-Hall, 1999).

[117] R. W. Boyd, *Nonlinear Optics* (Academy Press, San Diego, USA, 2008), 3rd ed.

[118] P. C. D. Hobbs, *Building electro-optical systems* (John Wiley & Sons, Inc., Hoboken, New Jersey, 2009), 2nd ed.

[119] NSM, "GaAs band structure and carrier concentration," (2011). http://www.ioffe.ru/SVA/NSM/Semicond/GaAs/bandstr.htm.

[120] C. H. Lee, R. K. Chang, and N. Bloembergen, "Nonlinear electroreflectance in silicon and silver," Phys. Rev. Lett. **18**, 167 (1967).

[121] K. Hakuta, L. Marmet, and B. P. Stoicheff, "Electric-field-induced 2nd-harmonic generation with reduced absorption in atomic-hydrogen," Phys. Rev. Lett. **66**, 596 (1991).

[122] J. Bloch, J. G. Mihaychuk, and H. M. van Driel, "Electron photoinjection from silicon to ultrathin SiO_2 films via ambient oxygen," Phys. Rev. Lett. **77**, 920 (1996).

[123] C. K. Sun, S. W. Chu, S. P. Tai, S. Keller, U. K. Mishra, and S. P. DenBaars, "Scanning second-harmonic/third-harmonic generation microscopy of gallium nitride," Appl. Phys. Lett. **77**, 2331 (2000).

[124] J. Qi, M. S. Yeganeh, I. Koltover, A. G. Yodh, and W. M. Theis, "Depletion-electric-field-induced changes in second-harmonic generation from GaAs," Phys. Rev. Lett. **71**, 633 (1993).

[125] A. Devizis, A. Serbenta, K. Meerholz, D. Hertel, and V. Gulbinas, "Ultrafast dynamics of carrier mobility in a conjugated polymer probed at molecular and microscopic length scales," Phys. Rev. Lett. **103**, 027404 (2009).

[126] H. G. de Chatellus and E. Freysz, Opt. Exp. **9**, 586 (2001).

[127] T. M. Fortier, P. A. Roos, D. J. Jones, S. T. Cundiff, R. D. R. Bhat, and J. E. Sipe, "Carrier-envelope phase-controlled quantum interference of injected photocurrents in semiconductors," Phys. Rev. Lett. **92**, 147403 (2004).

[128] L. Costa, M. Betz, M. Spasenovic, A. D. Bristow, and H. M. van Driel, "All-optical injection of ballistic electrical currents in unbiased silicon," Nat. Phys. **3**, 632 (2007).

[129] E. Y. Sherman, R. M. Abrarov, and J. E. Sipe, "Mode coupling and evolution in broken-symmetry plasmas," Phys. Rev. B **80**, 161308 (2009).

[130] H. Zhao, "Lock-in detection of charge and spin," (Unpublished).

[131] M. L. Boas, *Mathematical Methods in the Physical Sciences* (John Wiley & Sons, Inc., 1996), 2nd ed.

[132] K. S. Novoselov, A. K. Geim, S. V. Morozov, D. Jiang, Y. Zhang, S. V. Dubonos, I. V. Grigorieva, and A. A. Firsov, "Electric field effect in atomically thin carbon films," Science **306**, 666 (2004).

[133] P. R. Wallace, "The band theory of graphite," Phys. Rev. **71**, 622 (1947).

[134] K. S. Novoselov, A. K. Geim, S. V. Morozov, D. Jiang, M. I. Katsnelson, I. V. Grigorieva, S. V. Dubonos, and A. A. Firsov, "Two-dimensional gas of massless dirac fermions in graphene," Nature **438**, 197 (2005).

[135] A. A. Balandin, S. Ghosh, W. Z. Bao, I. Calizo, D. Teweldebrhan, F. Miao, and C. N. Lau, "Superior thermal conductivity of single-layer graphene," Nano Lett. **8**, 902 (2008).

[136] C. Lee, X. D. Wei, J. W. Kysar, and J. Hone, "Measurement of the elastic properties and intrinsic strength of monolayer graphene," Science **321**, 385 (2008).

[137] Y. M. Lin, C. Dimitrakopoulos, K. A. Jenkins, D. B. Farmer, H. Y. Chiu, A. Grill, and P. Avouris, "100-ghz transistors from wafer-scale epitaxial graphene," Science **327**, 662 (2010).

[138] F. Liu, J. Y. Choi, and T. S. Seo, "Graphene oxide arrays for detecting specific dna hybridization by fluorescence resonance energy transfer," Biosensors and Bioelectronics **25**, 2361 (2010).

[139] M. D. Stoller, S. J. Park, Y. W. Zhu, J. H. An, and R. S. Ruoff, "Graphene-based ultracapacitors," Nano Lett. **8**, 3498 (2008).

[140] M. Liu, X. Yin, E. Ulin-Avila, B. Geng, T. Zentgraf, L. Ju, F. Wang, and X. Zhang, "A graphene-based broadband optical modulator," Nature **474**, 64 (2011).

[141] Z. P. Sun, T. Hasan, F. Torrisi, D. Popa, G. Privitera, F. Q. Wang, F. Bonaccorso, D. M. Basko, and A. C. Ferrari, "Graphene mode-locked ultratast laser," ACS Nano **4**, 803 (2010).

[142] X. Wang, L. J. Zhi, and K. Mullen, "Transparent, conductive graphene electrodes for dye-sensitized solar cells," Nano Lett. **8**, 323 (2008).

[143] C. Berger, Z. M. Song, T. B. Li, X. B. Li, A. Y. Ogbazghi, R. Feng, Z. T. Dai, A. N. Marchenkov, E. H. Conrad, P. N. First, and W. A. de Heer, "Ultrathin epitaxial graphite: 2d electron gas properties and a route toward graphene-based nanoelectronics," J. Phys. Chem. B **108**, 19912 (2004).

[144] S. Stankovich, D. A. Dikin, R. D. Piner, K. A. Kohlhaas, A. Kleinhammes, Y. Jia, Y. Wu, S. T. Nguyen, and R. S. Ruoff, "Synthesis of graphene-based nanosheets via chemical reduction of exfoliated graphite oxide," Carbon **45**, 1558 (2007).

[145] S. A. Wang, P. K. Ang, Z. Q. Wang, A. L. L. Tang, J. T. L. Thong, and K. P. Loh, "High mobility, printable, and solution-processed graphene electronics," Nano Lett. **10**, 92 (2010).

[146] K. S. Kim, Y. Zhao, H. Jang, S. Y. Lee, J. M. Kim, J. H. Ahn, P. Kim, J. Y. Choi, and B. H. Hong, "Large-scale pattern growth of graphene films for stretchable transparent electrodes," Nature **457**, 706 (2009).

[147] X. S. Li, W. W. Cai, J. H. An, S. Kim, J. Nah, D. X. Yang, R. Piner, A. Velamakanni, I. Jung, E. Tutuc, S. K. Banerjee, L. Colombo, and R. S. Ruoff, "Large-area synthesis of high-quality and uniform graphene films on copper foils," Science **324**, 1312 (2009).

[148] K. S. Novoselov, E. McCann, S. V. Morozov, V. I. Fal'ko, M. I. Katsnelson, U. Zeitler, D. Jiang, F. Schedin, and A. K. Geim, "Unconventional quantum hall effect and berry's phase of 2 pi in bilayer graphene," Nat. Phys. **2**, 177 (2006).

[149] M. I. Katsnelson, K. S. Novoselov, and A. K. Geim, "Chiral tunnelling and the klein paradox in graphene," Nat. Phys. **2**, 620 (2006).

[150] A. C. Ferrari, J. C. Meyer, V. Scardaci, C. Casiraghi, M. Lazzeri, F. Mauri, S. Piscanec, D. Jiang, K. S. Novoselov, S. Roth, and A. K. Geim, "Raman spectrum of graphene and graphene layers," Phys. Rev. Lett. **97** (2006).

[151] C. H. Lui, K. F. Mak, J. Shan, and T. F. Heinz, "Ultrafast photoluminescence from graphene," Phys. Rev. Lett. **105** (2010).

[152] J. J. Dean and H. M. van Driel, "Second harmonic generation from graphene and graphitic films," Appl. Phys. Lett. **95** (2009).

[153] D. Sun, Z. K. Wu, C. Divin, X. B. Li, C. Berger, W. A. de Heer, P. N. First, and T. B. Norris, "Ultrafast relaxation of excited dirac fermions in epitaxial graphene using optical differential transmission spectroscopy," Phys. Rev. Lett. **101**, 157402 (2008).

[154] P. Blake, "Graphene industries products," http://grapheneindustries.com/?Products.

[155] P. Blake, E. W. Hill, A. H. C. Neto, K. S. Novoselov, D. Jiang, R. Yang, T. J. Booth, and A. K. Geim, "Making graphene visible," Appl. Phys. Lett. **91**, 3 (2007).

[156] J. C. Meyer, A. K. Geim, M. I. Katsnelson, K. S. Novoselov, T. J. Booth, and S. Roth, "The structure of suspended graphene sheets," Nature **446**, 60 (2007).

[157] B. Gao, G. Hartland, T. Fang, M. Kelly, D. Jena, H. Xing, and L. Huang, "Studies of intrinsic hot phonon dynamics in suspended graphene by transient absorption microscopy," Nano Lett. **11**, 3184 (2011).

[158] K. I. Bolotin, K. J. Sikes, J. Hone, H. L. Stormer, and P. Kim, "Temperature-dependent transport in suspended graphene," Phys. Rev. Lett. **101** (2008).

[159] N. I. Kovtyukhova, P. J. Ollivier, B. R. Martin, T. E. Mallouk, S. A. Chizhik, E. V. Buzaneva, and A. D. Gorchinskiy, "Layer-by-layer assembly of ultrathin composite films from micron-sized graphite oxide sheets and polycations," Chemistry of Materials **11**, 771 (1999).

[160] S. Gilje, S. Han, M. Wang, K. L. Wang, and R. B. Kaner, "A chemical route to graphene for device applications," Nano Lett. **7**, 3394 (2007).

[161] W. A. de Heer, C. Berger, X. S. Wu, P. N. First, E. H. Conrad, X. B. Li, T. B. Li, M. Sprinkle, J. Hass, M. L. Sadowski, M. Potemski, and G. Martinez, "Epitaxial graphene," Solid State Commun. **143**, 92 (2007).

[162] J. Hass, F. Varchon, J. E. Millan-Otoya, M. Sprinkle, N. Sharma, W. A. De Heer, C. Berger, P. N. First, L. Magaud, and E. H. Conrad, "Why multilayer graphene on 4h-sic(000(1)over-bar) behaves like a single sheet of graphene," Phys. Rev. Lett. **100**, 4 (2008).

[163] C. Berger, Z. M. Song, X. B. Li, X. S. Wu, N. Brown, C. Naud, D. Mayou, T. B. Li, J. Hass, A. N. Marchenkov, E. H. Conrad, P. N. First, and W. A. de Heer, "Electronic confinement and coherence in patterned epitaxial graphene," Science **312**, 1191 (2006).

[164] G. Gu, S. Nie, R. M. Feenstra, R. P. Devaty, W. J. Choyke, W. K. Chan, and M. G. Kane, "Field effect in epitaxial graphene on a silicon carbide substrate," Appl. Phys. Lett. **90** (2007).

[165] D. Sun, C. Divin, C. Berger, W. A. de Heer, P. N. First, and T. B. Norris, "Spectroscopic measurement of interlayer screening in multilayer epitaxial graphene," Phys. Rev. Lett. **104**, 136802 (2010).

[166] A. Reina, X. T. Jia, J. Ho, D. Nezich, H. B. Son, V. Bulovic, M. S. Dresselhaus, and J. Kong, "Large area, few-layer graphene films on arbitrary substrates by chemical vapor deposition," Nano Lett. **9**, 30–35 (2009).

[167] A. H. Castro Neto, F. Guinea, N. M. R. Peres, K. S. Novoselov, and A. K. Geim, "The electronic properties of graphene," Rev. Mod. Phys. **81**, 109 (2009).

[168] C. Kittel, *Introduction to Solid State Physics* (John Wiley & Sons, Inc., 2005), 8th ed.

[169] S. S. Li, *Semiconductor physical electronics* (Plenum Press, 1993).

[170] R. R. Nair, P. Blake, A. N. Grigorenko, K. S. Novoselov, T. J. Booth, T. Stauber, N. M. R. Peres, and A. K. Geim, "Fine structure constant defines visual transparency of graphene," Science **320**, 1308 (2008).

[171] K. F. Mak, M. Y. Sfeir, Y. Wu, C. H. Lui, J. A. Misewich, and T. F. Heinz, "Measurement of the optical conductivity of graphene," Phys. Rev. Lett. **101** (2008).

[172] W.-T. Liu, S. W. Wu, P. J. Schuck, M. Salmeron, Y. R. Shen, and F. Wang, "Nonlinear broadband photoluminescence of graphene induced by femtosecond laser irradiation," Phys. Rev. B **82**, 081408 (2010).

[173] R. J. Stohr, R. Kolesov, J. Pflaum, and J. Wrachtrup, "Fluorescence of laser-created electron-hole plasma in graphene," Phys. Rev. B **82** (2010).

[174] J. J. Dean and H. M. van Driel, "Graphene and few-layer graphite probed by second-harmonic generation: Theory and experiment," Phys. Rev. B **82** (2010).

[175] Z. F. Liu, Q. Liu, Y. Huang, Y. F. Ma, S. G. Yin, X. Y. Zhang, W. Sun, and Y. S. Chen, "Organic photovoltaic devices based on a novel acceptor material: Graphene," Adv. Mat. **20**, 3924 (2008).

[176] J. S. Bunch, A. M. van der Zande, S. S. Verbridge, I. W. Frank, D. M. Tanenbaum, J. M. Parpia, H. G. Craighead, and P. L. McEuen, "Electromechanical resonators from graphene sheets," Science **315**, 490 (2007).

[177] S. Berciaud, M. Y. Han, K. F. Mak, L. E. Brus, P. Kim, and T. F. Heinz, "Electron and optical phonon temperatures in electrically biased graphene," Phys. Rev. Lett. **104**, 227401 (2010).

[178] J. M. Dawlaty, S. Shivaraman, M. Chandrashekhar, F. Rana, and M. G. Spencer, "Measurement of ultrafast carrier dynamics in epitaxial graphene," Appl. Phys. Lett. **92**, 042116 (2008).

[179] P. A. George, J. Strait, J. Dawlaty, S. Shivaraman, M. Chandrashekhar, F. Rana, and M. G. Spencer, "Ultrafast optical-pump terahertz-probe spectroscopy of the carrier relaxation and recombination dynamics in epitaxial graphene," Nano Lett. **8**, 4248 (2008).

[180] H. Choi, F. Borondics, D. A. Siegel, S. Y. Zhou, M. C. Martin, A. Lanzara, and R. A. Kaindl, "Broadband electromagnetic response and ultrafast dynamics of few-layer epitaxial graphene," Appl. Phys. Lett. **94**, 172102 (2009).

[181] R. W. Newson, J. Dean, B. Schmidt, and H. M. van Driel, "Ultrafast carrier kinetics in exfoliated graphene and thin graphite films," Opt. Express **17**, 2326 (2009).

[182] S. Kumar, M. Anija, N. Kamaraju, K. S. Vasu, K. S. Subrahmanyam, A. K. Sood, and C. N. R. Rao, "Femtosecond carrier dynamics and saturable absorption in graphene suspensions," Appl. Phys. Lett. **95**, 191911 (2009).

[183] H. Wang, J. H. Strait, P. A. George, S. Shivaraman, V. B. Shields, M. Chandrashekhar, J. Hwang, F. Rana, M. G. Spencer, C. S. Ruiz-Vargas, and J. Park, "Ultrafast relaxation dynamics of hot optical phonons in graphene," Appl. Phys. Lett. **96**, 081917 (2010).

[184] L. B. Huang, G. V. Hartland, L. Q. Chu, Luxmi, R. M. Feenstra, C. X. Lian, K. Tahy, and H. L. Xing, "Ultrafast transient absorption microscopy studies of carrier dynamics in epitaxial graphene," Nano Lett. **10**, 1308 (2010).

[185] N. Bonini, M. Lazzeri, N. Marzari, and F. Mauri, "Phonon anharmonicities in graphite and graphene," Phys. Rev. Lett. **99** (2007).

[186] P. J. Hale, S. M. Hornett, J. Moger, D. W. Horsell, and E. Hendry, "Hot phonon decay in supported and suspended exfoliated graphene," Phys. Rev. B **83**, 121404 (2011).

[187] X. Zhao, Z.-B. Liu, W.-B. Yan, Y. Wu, X.-L. Zhang, Y. Chen, and J.-G. Tian, "Ultrafast carrier dynamics and saturable absorption of solution-processable few-layered graphene oxide," Appl. Phys. Lett. **98**, 121905 (2011).

[188] K. F. Mak, C. H. Lui, and T. F. Heinz, "Measurement of the thermal conductance of the graphene/SiO$_2$ interface," Appl. Phys. Lett. **97**, 221904 (2010).

[189] M. Breusing, S. Kuehn, T. Winzer, E. Malicacute, F. Milde, N. Severin, J. P. Rabe, C. Ropers, A. Knorr, and T. Elsaesser, "Ultrafast nonequilibrium carrier dynamics in a single graphene layer," Phys. Rev. B **83**, 153410 (2011).

[190] J. Z. Shang, T. Yu, J. Y. Lin, and G. G. Gurzadyan, "Ultrafast electron-optical phonon scattering and quasiparticle lifetime in cvd-grown graphene," ACS Nano **5**, 3278 (2011).

[191] K.-J. Yee, J.-H. Kim, M.-H. Jung, B.-H. Hong, and K.-J. Kong, "Ultrafast modulation of optical transitions in monolayer and multilayer graphene," Carbon **49**, 4781 (2011).

[192] P. Plochocka, P. Kossacki, A. Golnik, T. Kazimierczuk, C. Berger, W. A. de Heer, and M. Potemski, "Slowing hot-carrier relaxation in graphene using a magnetic field," Phys. Rev. B **80** (2009).

[193] H. Zhao, E. J. Loren, A. L. Smirl, and H. M. van Driel, "Dynamics of charge currents ballistically injected in gaas by quantum interference," J. Appl. Phys. **103** (2008).

[194] B. A. Ruzicka, K. Higley, L. K. Werake, and H. Zhao, "All-optical generation and detection of subpicosecond ac spin-current pulses in gaas," Phys. Rev. B **78** (2008).

[195] E. J. Loren, H. Zhao, and A. L. Smirl, "All-optical injection and detection of ballistic charge currents in germanium," J. Appl. Phys. **108** (2010).

[196] D. Sun, C. Divin, J. Rioux, J. E. Sipe, C. Berger, W. A. de Heer, P. N. First, and T. B. Norris, "Coherent control of ballistic photocurrents in multilayer epitaxial graphene using quantum interference," Nano Lett. **10**, 1293 (2010).

147

[197] J. Rioux, G. Burkard, and J. E. Sipe, "Current injection by coherent one- and two-photon excitation in graphene and its bilayer," Phys. Rev. B **83**, 195406 (2011).

[198] J. R. Williams, L. DiCarlo, and C. M. Marcus, "Quantum hall effect in a gate-controlled p-n junction of graphene," Science **317**, 638 (2007).

[199] J. H. Chen, C. Jang, S. Adam, M. S. Fuhrer, E. D. Williams, and M. Ishigami, "Charged-impurity scattering in graphene," Nat. Phys. **4**, 377 (2008).

[200] S. V. Morozov, K. S. Novoselov, M. I. Katsnelson, F. Schedin, D. C. Elias, J. A. Jaszczak, and A. K. Geim, "Giant intrinsic carrier mobilities in graphene and its bilayer," Phys. Rev. Lett. **100** (2008).

[201] D. Waldmann, J. Jobst, F. Speck, T. Seyller, M. Krieger, and H. B. Weber, "Bottom-gated epitaxial graphene," nat. mat. **10**, 357 (2011).

[202] G. Eda, G. Fanchini, and M. Chhowalla, "Large-area ultrathin films of reduced graphene oxide as a transparent and flexible electronic material," Nat. Nnanotechnol. **3**, 270 (2008).

[203] S. Winnerl, M. Orlita, P. Plochocka, P. Kossacki, M. Potemski, T. Winzer, E. Malic, A. Knorr, M. Sprinkle, C. Berger, W. de Heer, H. Schneider, and M. Helm, "Carrier dynamics in epitaxial graphene close to the dirac point," arXiv:1105.2518v2 (2011).

[204] J. Z. Shang, Z. Q. Luo, C. X. Cong, J. Y. Lin, T. Yu, and G. G. Gurzadyan, "Femtosecond uv-pump/visible-probe measurements of carrier dynamics in stacked graphene films," Appl. Phys. Lett. **97** (2010).

[205] T. Hertel and G. Moos, "Electron-phonon interaction in single-wall carbon nanotubes: A time-domain study," Phys. Rev. Lett. **84**, 5002 (2000).

[206] T. Hertel, R. Fasel, and G. Moos, "Charge-carrier dynamics in single-wall carbon nanotube bundles: a time-domain study," Appl. Phys. A-Mater. Sci. Process. **75**, 449 (2002).

[207] Y. C. Chen, N. R. Raravikar, L. S. Schadler, P. M. Ajayan, Y. P. Zhao, T. M. Lu, G. C. Wang, and X. C. Zhang, "Ultrafast optical switching properties of single-wall carbon nanotube polymer composites at 1.55 mu m," Appl. Phys. Lett. **81**, 975 (2002).

[208] J. S. Lauret, C. Voisin, G. Cassabois, C. Delalande, P. Roussignol, O. Jost, and L. Capes, "Ultrafast carrier dynamics in single-wall carbon nanotubes," Phys. Rev. Lett. **90**, 057404 (2003).

[209] S. Tatsuura, M. Furuki, Y. Sato, I. Iwasa, M. Q. Tian, and H. Mitsu, "Semiconductor carbon nanotubes as ultrafast switching materials for optical telecommunications," Adv. Mater. **15**, 534 (2003).

[210] H. Han, S. Vijayalakshmi, A. Lan, Z. Iqbal, H. Grebel, E. Lalanne, and A. M. Johnson, "Linear and nonlinear optical properties of single-walled carbon nanotubes within an ordered array of nanosized silica spheres," Appl. Phys. Lett. **82**, 1458 (2003).

[211] O. J. Korovyanko, C. X. Sheng, Z. V. Vardeny, A. B. Dalton, and R. H. Baughman, "Ultrafast spectroscopy of excitons in single-walled carbon nanotubes," Phys. Rev. Lett. **92**, 017403 (2004).

[212] Y. Z. Ma, J. Stenger, J. Zimmermann, S. M. Bachilo, R. E. Smalley, R. B. Weisman, and G. R. Fleming, "Ultrafast carrier dynamics in single-walled carbon nanotubes probed by femtosecond spectroscopy," J. Chem. Phys. **120**, 3368 (2004).

[213] C. Manzoni, A. Gambetta, E. Menna, M. Meneghetti, G. Lanzani, and G. Cerullo, "Intersubband exciton relaxation dynamics in single-walled carbon nanotubes," Phys. Rev. Lett. **94**, 207401 (2005).

[214] L. Perfetti, T. Kampfrath, F. Schapper, A. Hagen, T. Hertel, C. M. Aguirre, P. Desjardins, R. Martel, C. Frischkorn, and M. Wolf, "Ultrafast dynamics of delocalized and localized electrons in carbon nanotubes," Phys. Rev. Lett. **96**, 027401 (2006).

[215] H. Zhao, S. Mazumdar, C. X. Sheng, M. Tong, and Z. V. Vardeny, "Photophysics of excitons in quasi-one-dimensional organic semiconductors: Single-walled carbon nanotubes and pi-conjugated polymers," Phys. Rev. B **73**, b73075403 (2006).

[216] L. B. Huang, H. N. Pedrosa, and T. D. Krauss, "Ultrafast ground-state recovery of single-walled carbon nanotubes," Phys. Rev. Lett. **93**, 017403 (2004).

[217] C. X. Sheng, Z. V. Vardeny, A. B. Dalton, and R. H. Baughman, "Exciton dynamics in single-walled nanotubes: Transient photoinduced dichroism and polarized emission," Phys. Rev. B **71**, 125427 (2005).

[218] G. N. Ostojic, S. Zaric, J. Kono, M. S. Strano, V. C. Moore, R. H. Hauge, and R. E. Smalley, "Interband recombination dynamics in resonantly excited single-walled carbon nanotubes," Phys. Rev. Lett. **92**, 117402 (2004).

[219] R. J. Ellingson, C. Engtrakul, M. Jones, M. Samec, G. Rumbles, A. J. Nozik, and M. J. Heben, "Ultrafast photoresponse of metallic and semiconducting single-wall carbon nanotubes," Phys. Rev. B **71**, 115444 (2005).

[220] J. P. Yang, M. M. Kappes, H. Hippler, and A. N. Unterreiner, "Femtosecond transient absorption spectroscopy of single-walled carbon nanotubes in aqueous surfactant suspensions: Determination of the lifetime of the lowest excited state," Phys. Chem. Chem. Phys. **7**, 512 (2005).

[221] D. J. Styers-Barnett, S. P. Ellison, B. P. Mehl, B. C. Westlake, R. L. House, C. Park, K. E. Wise, and J. M. Papanikolas, "Exciton dynamics and biexciton formation in single-walled carbon nanotubes studied with femtosecond transient absorption spectroscopy," J. Phys. Chem. C **112**, 4507 (2008).

[222] L. Luer, G. Lanzani, J. Crochet, T. Hertel, J. Holt, and Z. V. Vardeny, "Ultrafast dynamics in metallic and semiconducting carbon nanotubes," Phys. Rev. B **80**, 205411 (2009).

[223] X. Xu, K. Chuang, R. J. Nicholas, M. B. Johnston, and L. M. Herz, "Terahertz excitonic response of isolated single-walled carbon nanotubes," J. Phys. Chem. C **113**, 18106 (2009).

[224] F. Hennrich, M. M. Kappes, M. Klinger, and A.-N. Unterreiner, "Ultrafast dynamics of the first excited-state of quasi monodispersed single-walled (9,7) carbon nanotubes," J. Chem. Phys. C **115**, 23711 (2011).

[225] F. Wang, G. Dukovic, L. E. Brus, and T. F. Heinz, "Time-resolved fluorescence of carbon nanotubes and its implication for radiative lifetimes," Phys. Rev. Lett. **92**, 177401 (2004).

[226] A. Hagen, G. Moos, V. Talalaev, and T. Hertel, "Electronic structure and dynamics of optically excited single-wall carbon nanotubes," Appl. Phys. A **78**, 1137 (2004).

[227] A. Hagen, M. Steiner, M. B. Raschke, C. Lienau, T. Hertel, H. H. Qian, A. J. Meixner, and A. Hartschuh, "Exponential decay lifetimes of excitons in individual single-walled carbon nanotubes," Phys. Rev. Lett. **95**, 197401 (2005).

[228] T. Hertel, A. Hagen, V. Talalaev, K. Arnold, F. Hennrich, M. Kappes, S. Rosenthal, J. Mcbride, H. Ulbricht, and E. Flahaut, "Spectroscopy of single- and double-wall carbon nanotubes in different environments," Nano Lett. **5**, 511 (2005).

[229] S. Reich, M. Dworzak, A. Hoffmann, C. Thomsen, and M. S. Strano, "Excited-state carrier lifetime in single-walled carbon nanotubes," Phys. Rev. B **71**, 033402 (2005).

[230] M. Jones, C. Engtrakul, W. K. Metzger, R. J. Ellingson, A. J. Nozik, M. J. Heben, and G. Rumbles, "Analysis of photoluminescence from solubilized single-walled carbon nanotubes," Phys. Rev. B **71**, 115426 (2005).

[231] H. Hirori, K. Matsuda, Y. Miyauchi, S. Maruyama, and Y. Kanemitsu, "Exciton localization of single-walled carbon nanotubes revealed by femtosecond excitation correlation spectroscopy," Phys. Rev. Lett. **97**, 257401 (2006).

[232] Y. Z. Ma, L. Valkunas, S. L. Dexheimer, S. M. Bachilo, and G. R. Fleming, "Femtosecond spectroscopy of optical excitations in single-walled carbon nanotubes: Evidence for exciton-exciton annihilation," Phys. Rev. Lett. **94**, 157402 (2005).

[233] Y. Z. Ma, L. Valkunas, S. L. Dexheimer, and G. R. Fleming, "Ultrafast exciton dynamics in semiconducting single-walled carbon nanotubes," Mole. Phys. **104**, 1179 (2006).

[234] M. W. Graham, J. Chmeliov, Y. Z. Ma, H. Shinohara, A. A. Green, M. C. Hersam, L. Valkunas, and G. R. Fleming, "Exciton dynamics in semiconducting carbon nanotubes," J. Chem. Phys. B **115**, 5201 (2011).

[235] M. W. Graham, Y.-Z. Ma, and G. R. Fleming, "Femtosecond photon echo spectroscopy of semiconducting single-walled carbon nanotubes," Nano Lett. **8**, 3936 (2008).

[236] A. Gambetta, C. Manzoni, E. Menna, M. Meneghetti, G. Cerullo, G. Lanzani, S. Tretiak, A. Piryatinski, A. Saxena, R. L. Martin, and A. R. Bishop, "Real-time observation of non-linear coherent phonon dynamics in single-walled carbon nanotubes," Nat. Phys. **2**, 515 (2006).

[237] K. Kato, K. Ishioka, M. Kitajima, J. Tang, R. Saito, and H. Petek, "Coherent phonon anisotropy in aligned single-walled carbon nanotubes," Nano Lett. **8**, 3102 (2008).

[238] L. Luer, C. Gadermaier, J. Crochet, T. Hertel, D. Brida, and G. Lanzani, "Coherent phonon dynamics in semiconducting carbon nanotubes: A quantitative study of electron-phonon coupling," Phys. Rev. Lett. **102**, 127401 (2009).

[239] K. Makino, A. Hirano, K. Shiraki, Y. Maeda, and M. Hase, "Ultrafast vibrational motion of carbon nanotubes in different ph environments," Phys. Rev. B **80**, 245428 (2009).

[240] A. Ueda, K. Matsuda, T. Tayagaki, and Y. Kanemitsua, "Carrier multiplication in carbon nanotubes studied by femtosecond pump-probe spectroscopy," Appl. Phys. Lett. **92**, 233105 (2008).

[241] S. Wang, M. Khafizov, X. Tu, M. Zheng, and T. D. Krauss, "Multiple exciton generation in single-walled carbon nanotubes," Nano Lett. **10**, 2381 (2010).

[242] J. Wang, M. W. Graham, Y. Ma, G. R. Fleming, and R. A. Kaindl, "Ultrafast spectroscopy of midinfrared internal exciton transitions in separated single-walled carbon nanotubes," Phys. Rev. Lett. **104**, 177401 (2010).

[243] J. S. Lauret, C. Voisin, G. Cassabois, J. Tignon, C. Delalande, P. Roussignol, O. Jost, and L. Capes, "Third-order optical nonlinearities of carbon nanotubes in the femtosecond regime," Appl. Phys. Lett. **85**, 3572 (2004).

[244] H. Hippler, A. N. Unterreiner, J. P. Yang, S. Lebedkin, and M. M. Kappes, "Evidence of ultrafast optical switching behaviour in individual single-walled carbon nanotubes," Phys. Chem. Chem. Phys. **6**, 2387 (2004).

[245] A. Maeda, S. Matsumoto, H. Kishida, T. Takenobu, Y. Iwasa, M. Shiraishi, M. Ata, and H. Okamoto, "Large optical nonlinearity of semiconducting single-walled carbon nanotubes under resonant excitations," Phys. Rev. Lett. **94**, 047404 (2005).

[246] S. Tao, Y. Miyata, K. Yanagi, H. Kataura, and H. Okamoto, "Subpicosecond coherent nonlinear optical response of isolated single-walled carbon nanotubes," Phys. Rev. B **80**, 201405 (2009).

[247] H. Nong, M. Gicquel, L. Bramerie, M. Perrin, F. Grillot, C. Levallois, A. Maalouf, and S. Loualiche, "A direct comparison of single-walled carbon nanotubes and quantum-wells based subpicosecond saturable absorbers for all optical signal regeneration at 1.55 μm," Appl. Phys. Lett. **96**, 061109 (2010).

[248] L. Valkunas, Y. Z. Ma, and G. R. Fleming, "Exciton-exciton annihilation in single-walled carbon nanotubes," Phys. Rev. B **73**, 115432 (2006).

[249] L. Luer, S. Hoseinkhani, D. Polli, J. Crochet, T. Hertel, and G. Lanzani, "Size and mobility of excitons in (6,5) carbon nanotubes," Nat. Phys. **5**, 54 (2009).

[250] D. M. Harrah, J. R. Schneck, A. A. Green, M. C. Hersam, L. D. Ziegler, and A. K. Swan, "Intensity-dependent exciton dynamics of (6,5) single-walled carbon nanotubes: Momentum selection rules, diffusion, and nonlinear interactions," ACS Nano **5**, 9898 (2011).

[251] F. Wang, G. Dukovic, E. Knoesel, L. E. Brus, and T. F. Heinz, "Observation of rapid auger recombination in optically excited semiconducting carbon nanotubes," Phys. Rev. B **70**, 241403 (2004).

[252] T. Hertel, S. Himmelein, T. Ackermann, D. Stich, and J. Crochet, "Diffusion limited photoluminescence quantum yields in 1-d semiconductors: Single-wall carbon nanotubes," ACS Nano **4**, 7161 (2010).

[253] Z. P. Zhu, J. Crochet, M. S. Arnold, M. C. Hersam, H. Ulbricht, D. Resasco, and T. Hertel, "Pump-probe spectroscopy of exciton dynamics in (6,5) carbon nanotubes," J. Phys. Chem. C **111**, 3831 (2007).

[254] R. M. Russo, E. J. Mele, C. L. Kane, I. V. Rubtsov, M. J. Therien, and D. E. Luzzi, "One-dimensional diffusion-limited relaxation of photoexcitations in suspensions of single-walled carbon nanotubes," Phys. Rev. B **74**, 041405 (2006).

[255] L. Cognet, D. A. Tsyboulski, J. D. R. Rocha, C. D. Doyle, J. M. Tour, and R. B. Weisman, "Stepwise quenching of exciton fluorescence in carbon nanotubes by single-molecule reactions," Science **316**, 1465 (2007).

[256] A. J. Siitonen, D. A. Tsyboulski, S. M. Bachilo, and R. B. Weisman, "Dependence of exciton mobility on structure in single-walled carbon nanotubes," J. Phys. Chem. Lett. **1**, 2189 (2010).

[257] C. Georgi, M. Bohmler, H. H. Qian, L. Novotny, and A. Hartschuh, "Probing exciton propagation and quenching in carbon nanotubes with near-field optical microscopy," Phys. Status Solidi B-Basic Solid State Phys. **246**, 2683 (2009).

[258] K. Yoshikawa, K. Matsuda, and Y. Kanemitsu, "Exciton transport in suspended single carbon nanotubes studied by photoluminescence imaging spectroscopy," J. Phys. Chem. C **114**, 4353 (2010).

[259] S. Moritsubo, T. Murai, T. Shimada, Y. Murakami, S. Chiashi, S. Maruyama, and Y. K. Kato, "Exciton diffusion in air-suspended single-walled carbon nanotubes," Phys. Rev. Lett. **104**, 247402 (2010).